Grid Frequency Regulation Provided by High Power Motor Drives

A Thesis Presented for the

Master of Science

Degree

The University of Tennessee, Knoxville

Taylor Lee Short

May 2020

© by Taylor Lee Short, 2020
All Rights Reserved.

Abstract

Induction motors make up a significant portion of the load on the power grid. The implementation of variable speeds drives (VSDs) with induction motors brings not only efficiency savings for the customers, but also possible benefits to the utility companies through demand response and other ancillary services. This project uses the HTB platform and PSCAD/EMTDC to develop, test, and utilize VSD connected industrial induction motors for industrial motor loads, such as fans, pump, and compressors.

With the development of new power devices with wide bandgaps, such as SiC and GaN devices, active front end VSDs are growing in popularity. For this reason, an active front end topology is used for the simulation and emulation of the system. Controls are implemented in the VSD, including DC link voltage, inner and outer current loop, and grid frequency regulation. Two different control techniques were used for the grid frequency regulation– one on the WECC system and one on a microgrid system. The different techniques were developed based on the frequency characteristics on both systems.

Table of Contents

1 Introduction and Background **1**

1.1 Induction Motor Motor Drives . . . 1

1.1.1 Induction Motor Drive Overview . . . 1

1.1.2 Motor Drives Benefits and Advantages . . . 1

1.1.3 Motor Drives Challenges and Mitigation Techniques . . . 3

1.2 Ancillary Services . . . 4

1.3 Demand Response . . . 5

1.3.1 Classification of DR Models . . . 7

1.4 Hardware Testbed . . . 12

1.4.1 Motivations and Advantages . . . 12

1.4.2 Construction and Operation . . . 13

1.4.3 Existing Emulators . . . 15

1.5 Project Description . . . 18

1.6 Thesis Structure . . . 19

2 Literature Review **20**

2.1 Induction Motor Emulator . . . 20

2.2 Active Front End vs Diode Front End Motor Drive . . . 23

2.3 Wide Bandgap Power Devices and VSDs . . . 25

2.4 Motor Drive Modeling . . . 28

2.4.1 Passive Component Modeling . . . 28

2.4.2 Power Electronics Modeling . . . 28

2.5 Motor Drive Front End Controls . . . 31

2.5.1 Current Control . . . 32
2.5.2 DC Link Control . . . 32
2.6 Motor Drive Back End Controls . . . 34
2.6.1 Motor Constant V/f Control . . . 34
2.7 Grid Frequency Support using VSD . . . 37
2.7.1 Grid frequency support using variable motor speed . . . 37
2.8 Chapter Summary . . . 40

3 Emulator Design **41**
3.1 Induction Motor Model . . . 41
3.2 VSD Model . . . 44
3.2.1 VSI Average Model . . . 44
3.2.2 HTB connected Rectifier Average Model . . . 46
3.3 DC Link Control . . . 48
3.4 Motor Constant V/f Control . . . 49
3.5 Grid Frequency Regulation . . . 49
3.5.1 Grid Frequency Regulation for a Microgrid System . . . 49
3.5.2 Grid Frequency Regulation for an Aggregate Western Electricity Coordinating Council System . . . 51
3.6 Simulation . . . 51
3.6.1 Emulation Model Verification . . . 51
3.7 Chapter Summary . . . 52

4 Experimental Results and Discussion **56**
4.1 HTB Experimental Set Up . . . 56
4.2 Microgrid System . . . 56
4.2.1 HTB Model Verification . . . 56
4.2.2 Microgrid System Results . . . 59
4.3 WECC System . . . 67
4.3.1 HTB Model Verification . . . 67
4.3.2 WECC System Results . . . 71

4.4 Chapter Summary 81

5 Summary and Conclusions **82**

Bibliography **85**

Vita **95**

List of Tables

2.1 Properties of Silicon and dominate WBG semiconductors 27

2.2 Derived coefficients for induction motors 39

3.1 Values for designed motor emulation. 43

3.2 Base values for VSD emulation. 45

4.1 Microgrid System and HTB Power and Voltage Bases 59

4.2 WECC System and HTB Power and Voltage Bases 71

4.3 Nadir frequency for generators during frequency event on WECC system with and without VSD frequency compensation. 80

List of Figures

1.1 Motor Drive Basic Schematic. 2

1.2 A sudden drop in system frequency triggers automated response to correct the frequency, followed by manual interventions from power system operators. Ancillary services provide these responses. 6

1.3 Classification of DR programs. 8

1.4 Power Circulation within the HTB [2]. 14

1.5 HTB and RTDS connection overview [3]. 16

1.6 Map of emulated HTB system and RTDS overlay on map of United States. 17

1.7 HTB visualization wall. 18

2.1 The emulator structure for three phase induction motor. 21

2.2 Diode Front End Motor Drive. 24

2.3 Active Front End Motor Drive 24

2.4 Properties of WBG materials 26

2.5 Expected evolution of WBG power electronics technologies 26

2.6 The average model for half-bridge switching circuit. 29

2.7 Average model of a rectifier in ABC coordinates. 30
2.8 Average model of a rectifier in DQ coordinates 30
2.9 Average model of a VSI in ABC coordinates. 31
2.10 Average model of a VSI in DQ coordinates. 32
2.11 Basic PI current control 33
2.12 DC voltage link control 33
2.13 Simplified steady state equivalent circuit of induction motor 35
2.14 Stator voltage vs. frequency profile under V/f control 35
2.15 Modified V/f profile 36
2.16 Torque and speed curves for an induction motor. 37
2.17 The block diagram of the primary controller (2.17a), inertia emulator (2.17b), and the speed controller 2.17c 38
2.18 VSC inertia emulation control 40

3.1 Active front end motor drive topology for emulation. 42

3.2 Overview of control method used for the implementation of the VSD and induction motor emulator. 42

3.3 Inner current loop of HTB VACON. 43

3.4 Induction motor load model structure. 44

3.5 Integration of VSD and Induction Motor Emulator and HTB converter. . . . 47

3.6 DC voltage link control 48
3.7 Average model of VSD in dq coordinates 50

3.8 Frequency regulation control for microgrid. 51

3.9 Frequency regulation control for WECC. 52

3.10 Simulink verification of VSD model when H=0.1. 53

3.11 Simulink verification of VSD model when H=0.6. 54

3.12 Simulink verification of VSD model when H=0.8. 55

4.1 Emulated system for VSD model verification. 57

4.2 Experimental setup for HTB platform testing. 58

4.3 VSD model response for a microgrid on HTB platform and in PSCAD. . . . 60

4.4 One-line diagram of the microgrid system. 61

4.5 Frequency during 0.1 p.u. load increase for varying penetration of VSD. . . . 62

4.6 VSD power and induction motor stator voltage and current during 0.1 p.u. ZIP load increase. 63

4.7 The top figure shows the frequency during 0.1 p.u. load increase with 1 VSD on system comparing frequency regulation and without frequency regulation. The bottom figure shows induction motor stator voltage and VSD power. . . 64

4.8 Grid frequency and induction motor stator voltage during 0.1 p.u. load increase with 1 VSD on system. 65

4.9 The top figure shows the frequency during 0.1 p.u. load increase with 2 VSD on system comparing frequency regulation and without frequency regulation. The bottom figure shows the induction motor stator voltage and VSD power. 65

4.10 Grid frequency and induction motor stator voltage during 0.1 p.u. load increase with 2 VSD on system. 66

4.11 The top figure shows the frequency during 0.1 p.u. load increase with 3 VSD on system comparing frequency regulation and without frequency regulation. The bottom figure shows the induction motor stator voltage and VSD power. 66

4.12 Grid frequency and induction motor stator voltage during 0.1 p.u. load increase with 3 VSD on system. 67

4.13 Frequency during first second after 0.1 p.u. load increase for varying penetration of VSD. 68

4.14 VSD model response on HTB platform and in PSCAD with 50% ZIP load increase. 69

4.15 VSD model response on HTB platform and in PSCAD with 60% ZIP load increase. 70

4.16 One-line diagram of the aggregate WECC system. 72

4.17 VSD power and induction motor stator voltage and current for grid frequency regulation on the WECC system. 73

4.18 Frequency of generators 1, 4, 6, and 7 during 470 MW ZIP load increase at Bus 1 comparing with frequency regulation and without frequency regulation. 74

4.19 Load at Buses 4 and 10 during 470 MW ZIP load increase at Bus 1. 75

4.20 Frequency of generators 4, 6, and 7 during 485 MW ZIP load increase at Bus 4 comparing with frequency regulation and without frequency regulation. . . 76

4.21 Load at Buses 4 and 10 during 485 MW ZIP load increase at Bus 4. 77

4.22 Frequency of generators 4, 6, and 7 during 530 MW ZIP load increase at Bus 7 comparing with frequency regulation and without frequency regulation. . . 78

4.23 Load at Buses 7 and 8 during 530 MW ZIP load increase at Bus 7. 79

4.24 Frequency of all generators on WECC system during 530 MW ZIP load increase at Bus 6. 79

Chapter 1

Introduction and Background

1.1 Induction Motor Motor Drives

1.1.1 Induction Motor Drive Overview

Induction motors are considered the workhorse for industry because of their low cost and robust construction. Induction motors are used in a wide range of industries, such as oil, mining, power, marine, paper, and wastewater. Applications include fans, pumps, compressors, grinding mills, metal rolling, mine hoists, refiners, and propulsion. An induction motor can be connected directly to the 60 Hz power grid and will operate at a relatively constant speed. However, the availability of power electronics allows the speed of the motor to vary. The power electronics used to connect motors to the grid are referred to as motor drives. Motor drives consist of two conversion phases– AC to DC and DC to AC or rectifier and inverter respectively. The rectifier and inverter are connected by a DC link capacitor. See Fig. 1.1 for an example of a basic motor drive topology. Most motor drive systems are referred to as adjustable speed drives (ASDs) or variable speed drives (VSDs).

1.1.2 Motor Drives Benefits and Advantages

Industrial motor systems consume more than 679 billion kWh per year and 25% of all electric energy sales. According to an assessment done by DOE in 2002, only 8% of all industrial motor systems have variable speed drives (VSDs). In this same study, it was determined

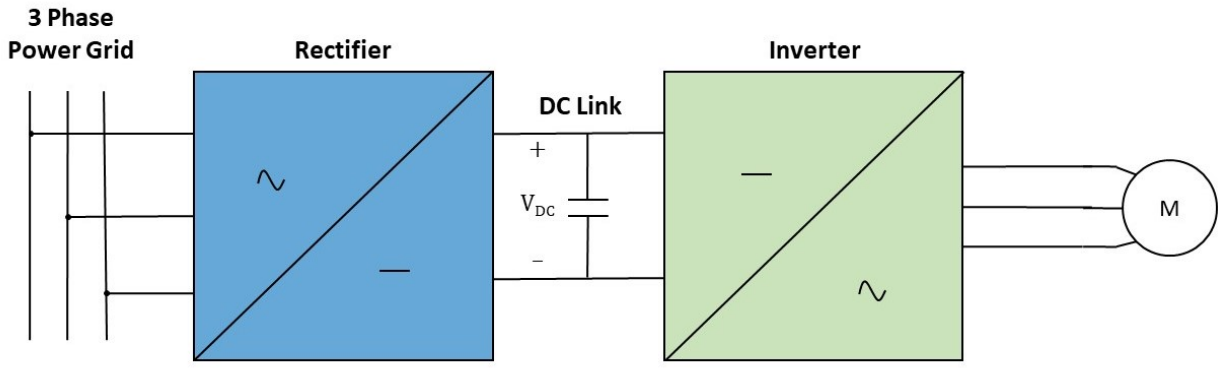


Figure 1.1: Motor Drive Basic Schematic.

that nearly two-thirds of all potential energy efficiency savings set forth by the Consortium for Energy Efficiency are accomplished by system improvements, such as VSDs or bypass loops in pumping systems[4]. Pumps, fans, and compressors show considerable improvements when VSDs are implemented. A VSD can regulate the flow of water or gas without the use of traditional mechanical equipment, which introduce significant loss into the system[5].

The survey suggests that a conservative estimate for energy savings from a VSD is 787 GWh/year for fan systems, 1366 GWh/year for air systems, and 6421 GWh/year for pump systems. The mid-range estimates for these savings are nearly twice that of the conservative estimates[4].

As of 2002, while 8% of industrial motor systems were equipped with a VSD, 90% of those were 20 hp or less. However, DOE estimated that 18-25% of total manufacturing motor system energy could add a VSD cost effectively[4]. The average payback time-frame on the investment of a VSD is only a year and a half. In addition to an increase in energy efficiency, VSDs can extend the lifetime of a motor by lowering starting currents and regulating the speed and power at or below ratings[6][7].

In addition to energy efficiency savings, a VSD-connected motor that can provide frequency support can provide potential benefits to the grid. The same reduction of the inrush current that improves the lifetime of the motor also improves stability of the power grid during motor startup[6]. Additionally, loads such as fans, air compressors, and pumps

can be controlled to provide support to the power grid, which are the same systems that find the majority of energy efficiency benefits from VSDs. These loads make up roughly 11% of all industrial motor loads[4]. This is a huge untapped resource for utilities. Many of these motor loads could be reduced without affecting primary production processes. Therefore, these loads could respond to grid fluctuations and assist in making the grid more reliable. Load-side participation in frequency regulation provides possible advantages in faster response, lower fuel consumption and emission, and better localization of disturbances[8]. VSDs are particularly equipped to implement frequency regulation, because load can be changed by changing motor speed. This is unique; most loads can only be controlled to be either on or off. While the availability of ancillary services is more unpredictable from loads than from traditional ancillary service sources, the development of VSDs, information systems, and the increase in energy prices provide a possible opening in this regulation market[9].

1.1.3 Motor Drives Challenges and Mitigation Techniques

While VSDs have become increasingly popular because of the energy efficiency gains and ease of control, the high rate of voltage rise (dv/dt) presents issues of motor insulation stress, electromagnetic interference (EMI), and bearing and leakage current caused by common-mode voltages[10]. Conventional inverters generate common-mode voltage within the motor windings, which may cause voltage to build up on the motor shaft. Charge accumulates on the rotor assembly until the voltage exceeds the dielectric capabilities of the bearing grease. This results in a repeated flash-over current, which can cause damage to the bearing surfaces[10]. Mitigation techniques for bearing currents include a shaft grounding system, insulated bearings, ceramic bearings, conducting grease, a Faraday shield, and design methods to eliminate common-mode voltages[10].

In many industrial applications, the VSD and motor are in different locations. This means the system requires long motor leads, which leads to more high frequency ringing at the motor terminals. This can result in over-voltages that stress the motor insulation, which can be mitigated by additional filters at the motor terminals. Additionally, EMI can be caused by the high switching speed of the power devices, especially with the rise of wide bandgap power device (discussed in Section 2.3). Traditionally, EMI is reduced through ac

line filters. However, additional mitigation techniques include common-mode inductors and transformers or grounding capacitors[10]. All of these challenges and resulting mitigation techniques increase the cost of installation or result in the need for more robust motor designs. Often customers will also install new motors with higher insulation capacity when adding a VSD to a system.

1.2 Ancillary Services

Ancillary services can support basic grid functions such as generating capacity, energy supply, and power delivery. This support is often provided by distributed energy resources (DER) or distributed generation (DG). However, with the integration of power electronic interfaced loads, many of the support functions provided by DG ancillary services can be provided by flexible loads. Currently, independent system operators' requirements do not allow much room for loads to operate in the regulatory market. For example, CAISO requires at least 0.5 MW power capacity to be able to participate in the frequency regulation market[11]. The focus of most interest in flexible loads is centered around air conditioning units and other residential loads. However, a medium voltage motor can have an operating capacity of near 5 MW, allowing a larger controllable capacity.

By 2009, both New York Independent System Operator (NYISO) and PJM Interconnect LLC (PJM) had a demand side ancillary service program[12]. For NYISO, demand side resources could participate in regulation and synchronous and non-synchronous reserve. PJM allows participation in regulation, synchronous reserve, and day ahead scheduling reserves[12].

The use of loads to regulate the grid is referred to as demand response. Most demand response programs adjust the load by an ON or OFF option. This happens one of two ways: (1) the customer gives the utility permission to interrupt their load during a designated time or (2) the customer is incentivised to reduce load during a time period. However, with the introduction of variable speed drives, loads' speed– and therefore load– can be varied over time. Motor loads, such as fans or pumps, can decrease or increase their load in response to the grid fluctuations. Large industrial fans and pumps are especially advantageous for this

application because these loads can often be reduced for a short time and will not interrupt any production processes.

There are two major regulatory services that can be provided by an industrial motor load: frequency regulation and voltage regulation. The VSD can inject reactive power providing voltage regulation, when the grid voltage at a bus is lower than that of the reference value. The opposite is true when the voltage at a bus is higher than that of the reference value– the VSD absorbs reactive power. For voltage support, the VSD must have an active front end rectifier. Frequency regulation is similar, but active power is provided or absorbed. If the frequency is above the reference value, active power from the load is reduced. If frequency is below the reference value, active power from the load is increased. Primary frequency regulation happens within 30 seconds of the event. After 30 seconds, generation secondary control takes over regulation. Fig. 1.2 shows the typical response for frequency regulation.

1.3 Demand Response

Demand Response (DR) is a subset of Demand Side Management (DSM), along with energy-efficiency and conservation. The U.S. Department of Energy defined DR as "a tariff or program established to motivate changes in electric use by end-use customers, in response to changes in the price of electricity over time, or to give incentive payments designed to induce lower electricity use at times of high market prices or when grid reliability is jeopardized" [13]. The main objectives of DR are to reduce power consumption, to reduce the total need of power generation, to change the demand, to follow available supply, and to reduce or eliminate overloads of the distribution system[14].

DR has applications in residential, commercial, and industrial sectors. Residential DR programs are more complicated due to the irregularity of consumption patterns. However, commercial buildings have near identical consumption patterns between various customers, making DR easier to design. Most commercial DR schemes include adoption of energy efficient building technologies or changing consumption behavior through price elasticity[14]. Finally, industrial customers have some of the largest loads; however, many of these loads are critical to the manufacturing process. Despite industrial customers heightened concerns

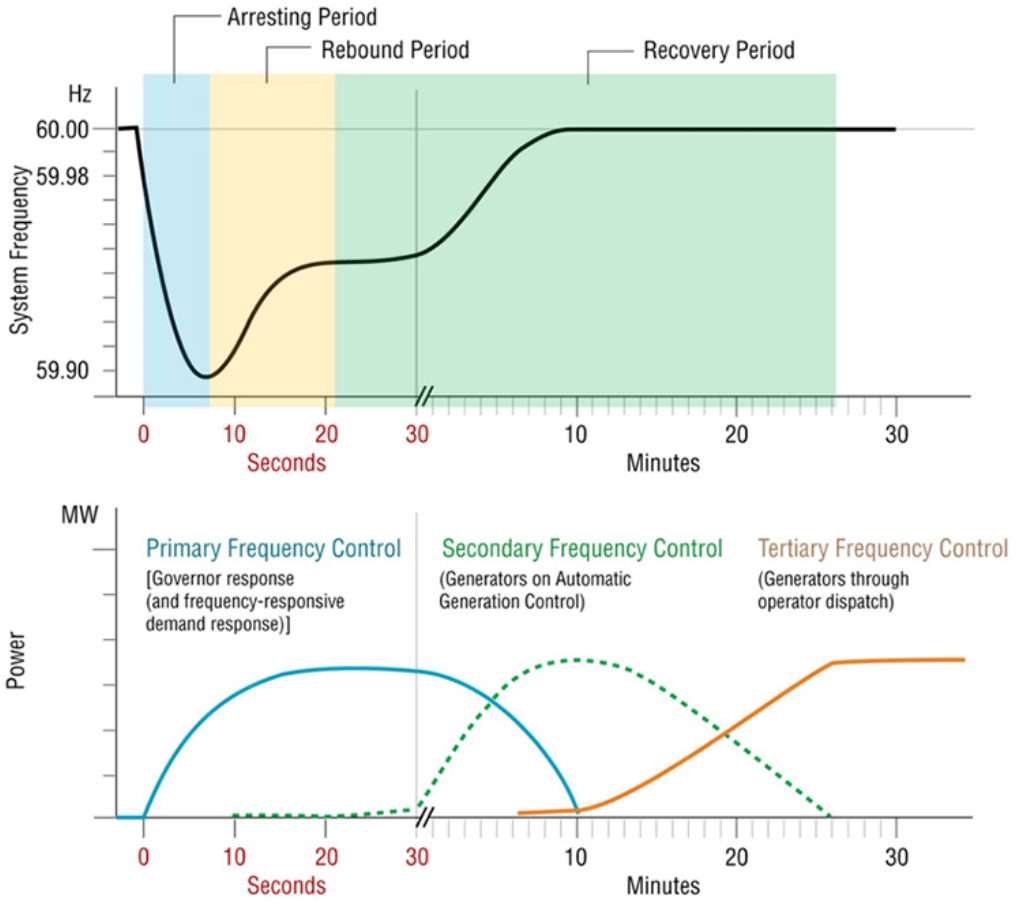


Figure 1.2: A sudden drop in system frequency triggers automated response to correct the frequency, followed by manual interventions from power system operators. Ancillary services provide these responses.[1].

about security, intelligent DR methods have the potential to increase reliability of the industrial system and the economic efficiency of the electricity infrastructure[15][16].

Reference [14] organizes DR into three categories: (1) control mechanism, (2) offered motivation, and (3) decision variables. Each of these categories can be further broken down. For DR based on control mechanisms, they can be classified into centralized or distributed programs. In this case, centralized mode refers to when consumers communicate directly to the power utility, without interaction between customers. Distributed mode refers to when the interaction between users provide information to the utility about total consumption[14].

Offered motivations can be broken down into time-based DR (also known as price-based DR) and incentive-based DR. In time-based DR, consumers are offered varying prices based on the electricity cost during different time periods. On the other hand, incentive-based are offered payments to motivate participation, but are also under constraints or are penalized for not participating[14]. Finally, DR that is based on decision variables can be broken down into task scheduling-based or energy management-based. In task scheduling, the control variable is the activation time of the requested load. For energy management, the main control is the power consumption of different loads[14]. In addition to the DR schemes, the optimization and control of the smart grid can be categorized into 5 groups: a) minimization of electricity cost, b) maximization of social welfare, c) minimization of aggregated power consumption, d) minimization of both electricity cost and aggregated power consumption, and e) both the maximization of social welfare and minimization of aggregated power consumption[14].

1.3.1 Classification of DR Models

Fig. 1.3 shows the classification used in [14]. This classification is divided into three groups based on control mechanism, offered motivation, and decision variables. Other references have, such as [17], simply classified DR into incentive-based programs and price-based programs. The following subsections further discuss each one of the classifications found in [14].

1.3.1.1 DR Based on Control Mechanism

DR based on control mechanism can be further broken down into centralized and distributed programs. In this case centralized mode refers to when consumers communicate directly to the power utility, without interaction between customers. Distributed mode refers to when the interaction between users provide information to the utility about total consumption. Currently, the power network is designed as a centralized system. However, the decentralized nature of distributed schemes allow for scalability and consumer privacy protection, which is an integral concern of industrial customers[14][18].

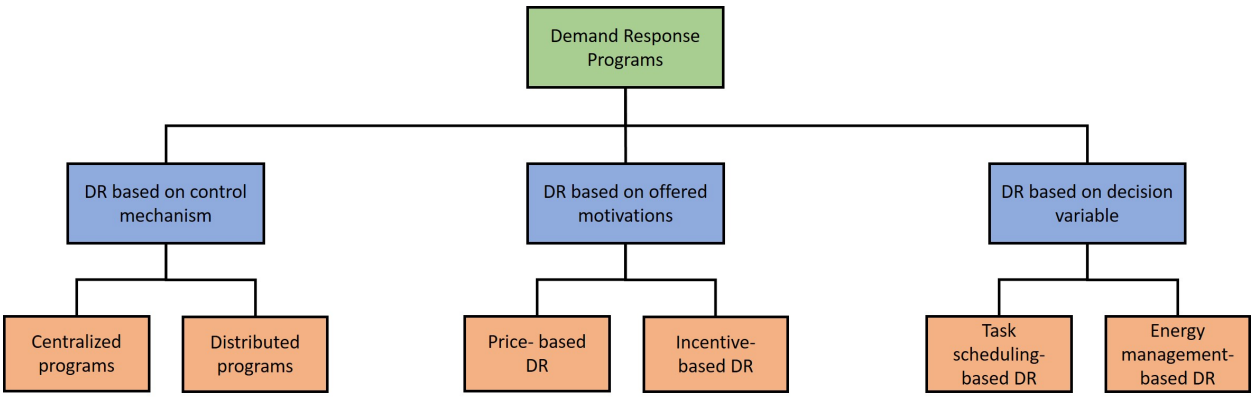


Figure 1.3: Classification of DR programs[14].

Centralized Schemes

Centralized schemes include a centralized controller that monitors and coordinates the DR procedure. The demand information is collected, and DR decisions are made for the demand scheduling. This method is effective in scheduling thermostatically controlled appliances, buildings, and charging stations for plug-in hybrid electric vehicles(PHEVs) and electric vehicles(EVs). Additionally, central controllers are often used in island microgrids.

Distributed Schemes

In a distributed system, the information is not centrally located and customers have indicators on the grid's state. Customers are able to respond based on the conditions and whether the event is critical. Many of distributed schemes have been inspired by the nature of internet traffic control [14]. Distributed control is often used in conjuction with other control mechanisms, including volt/var control or frequency response.

1.3.1.2 DR Based on Offered Motivations

Another method for categorizing DR schemes is by the motivation method offered to the customers. There are two main divisions in the category: time-based programs, also known as price-based program, and incentive-based programs.

Time-based DR

Time-based DR offers customers varying prices of electric consumption based on different time periods. Consumers are given this information, and they must determine whether they consume less power during time periods when electricity prices are high. There are many different pricing schemes used for time-based DR.

Flat pricing is the traditional pricing method in energy systems. Under this scheme, the only way to reduce customer bills is by reducing power usage throughout the day. Time-of-use (TOU) pricing is the use of varies pricing throughout the day. With this scheme, prices are held constant during different pricing periods, but vary between those time periods. These pricing periods can range from different hours within a day to different days within a week. For example, in California, they offer commercial customers three different pricing periods: off-peak, mid-peak, and peak[19]. It has been shown that TOU offered the lowest reduction in peak prices[20].This is because customers do not receive practical incentives to reduce their demand due to the high peak pricing.

Critical peak pricing (CPP) is similar to TOU pricing, except the price can change due to periods of system stress. The customers are notified of the price change a day-ahead. CPP experience similar adaption issues as TOU. Also, this scheme generally has higher peak pricing than TOU. However, electric energy providers gain higher benefits. There are a few variations to CPP, including fixed period CPP (CPP-F), variable peak pricing (VPP), variable period CPP (CPP-V), and extreme day CPP. In CPP-F, utilities select a critical peak price and choose a window with the highest wholesale market, thereby maximizing utility savings. VPP has varying peak price levels. For example, at Oklahoma Gas and Electric Company, three peak levels are offered: standard peak rate, high peak rate, and critical peak rate [14]. In CPP-V, an event can be triggered by the utility that can vary in start time and duration. Finally, extreme day CPP is critical peak pricing and is only applied to critical peak hours.

Peak load pricing (PLP) divides the day into different periods with different pricing. The price for each period is determined by the average consumption. Pricing is given to the customer at the beginning of each day. Adaptive pricing is similar to PLP, but utilities

calculate the prices real-time and give the customers the information at the beginning of each period.

Peak Day Rebates (PDR), also known as peak time rebates (PTR), give customers a rebate for responding to critical events. Reference [21] reveals that PDR is more effective than TOU, but CPP is more effective than PDR. Reference [22] shows that the balance of supply and demand does not seem to be clear because the rebate is so high.

In real-time pricing (RTP), utilities provide electric prices on a rolling basis, which is determined and announced before each pricing period. This schemes requires successful communication between the smart grid and the utility on a real-time basis, and has already been implemented with large industrial and commercial customers. However, RTP has not had much success in the residential sector. Day-ahead RTP (DA-RTP) provides an alternative to RTP that predicts the next-day real time prices. Customers are notified beforehand of the prices based on the predicted values.

Incentive-based DR

Incentive-based DR offers incentives or payment to the customer, which reduce their electricity during critical times. These incentives can take the form of bill credits, discount rates, or direct payment. Bill credit and discount rates are considered classical incentive-based programs, while direct payment is classified as market-based programs.

Direct load control (DLC) is a classic program which allows utilities to control customer load, turning the equipment on or off. These loads are generally air-conditioners and water-heaters and are directly controlled by the utility. This incentive-based program is generally implemented in residential and small commercial customers, and the incentive is given in advance. Industrial customers tend to not participate in DLC due to the delicate nature of most loads in the manufacturing process.

Uninterruptible/curtailable (I/C) load is similar to DLC in that it gives upfront incentives to participating customers. However, in an I/C program, customers are incentivized to reduce their load to a predefined level. If the customer does not participate when notified to curtail their load, they receive penalties. The customers have 30 to 60 minutes to respond once notified, and the utility is limited to the number of hours and times per year that they can

request a curtailment. Customers that participate in this program generally have power consumption of at least 3 MW.

Emergency DR programs (EDRPs) are a market-based program that combines DLC and I/C programs. Customers can choose whether to curtail their load or not, which determines whether they receive the payments. New York IDO has a similar program where if the customer curtails their load, the EDRP pays for energy during times of emergency, but does not pay for capacity. Implementations of EDRP have resulted in excessive shedding of the EDRP, which can result in power oscillations.

Capacity market program (CMP) is another market-based program which is offered to customers that are able to provide load reduction that can replace traditional generation. Customers generally receive day-ahead notification and are penalized if they choose not to participate. They receive payments whether curtailment is requested or not, but they can prove they have sufficient curtailment availability. Studies have shown CMP and I/C programs satisfied both customers and utilities.

Another market-based program is demand bidding (DB), which is offered to large customers who can offer curtailment bids to the wholesale market. In a program offered by ERCOT, it was discovered that capacity payment was not enough to incentivize formal bidding. However, a combination of DR and DB, where energy retailers request the curtailment, could be a solution to this issue. Finally, customers can be given the option to bid into the ancillary service market (ASM). This program looks similar to DB, but the bids are made to the ASM as opposed to the wholesale market.

1.3.1.3 DR Based on Decision Variables

This classification is based on DR programs that either decide when to activate a load or the amount of energy that can be allocated to each customer.

Task Scheduling-based DR

For task scheduling-based DR, the main control variable is the activation time of the requested loads. There are two type of loads : must-run loads and scheduled loads. Must-run loads cannot tolerate activation delay, such as refrigerators or light. Schedulable loads, such

as water heaters, PHEVs, or EVs, can be stopped, adjusted, or time-shifted. The main goal of these programs are to reduce power consumption during peak demand hours, by shifting the consumption to off-peak hours.

Energy Management-based DR

The main goal of energy management-based DR is to reduce the power consumption of certain loads, so that overall peak hour demand is reduced. This is achieved by controlling the appliance to consume less power during system stress. For example, an air conditioner could be changed by a couple degrees. Power consumption would reduce, but the customers would still feel comfortable. For these schemes, quality of experience (QoE) is often considered in the decision-making.

1.4 Hardware Testbed

The Center for Ultra-Wide-Area Resilient Electric Energy Transmission Networks (CURENT) has developed a converter-based grid emulator known as the Hardware Testbed (HTB) to study large scale power grids with a high penetration of renewable resources and other forward projected technologies. Using re-configurable voltage source inverters, the HTB emulates interconnected generation and loads. The converter-based emulators can be designed to have a bandwidth of several kHz, which allows the converters to accurately emulate voltage and current dynamics of the actual power system components. The HTB emulates the resiliency of the system by incorporating real time communication, protection, control, and cybersecurity. It has the capacity to examine many scenarios including line and bus faults [23],[24].

1.4.1 Motivations and Advantages

Traditional methods for analyzing power systems such as Power System Simulator for Engineering (PSSE) and Real Time Digital Power System Simulator (RTDS) tend to focus on either small-scale transients or large scale behaviors. In addition, these methods often do not include real world impacts like measurement errors, time delay, non-linearity, and

electronic interference. Even though experimental results tend to be more reliable for these reasons, some important characteristics of the power system are not included when scaled down. A converter-based large scale power system emulator, such as the HTB, emulates the reliability of the system by incorporating real time communication, protection, control and cybersecurity.

HTB's converter-based system can emulate both transients from power electronics and power grid system events. Power converters can act within tens of milliseconds. For example, an induction motor has a dynamic time scale of a couple seconds, so the converter is more than fast enough to represent the dynamic behavior of the motor. This can be said for most power system components, such as generators, motors, renewable generation, and loads. Using these capabilities, the converters can be programmed to emulate a broad and diverse group of power system components– allowing the HTB to demonstrate many different grid scenarios effectively and reliably. The HTB is a platform that can test converter control and system area control, as well as different microgrid architectures. The HTB is also designed so the only losses from the system are from the converters.

1.4.2 Construction and Operation

The HTB is designed with the converters connected to a DC bus on one side and the AC grid emulation on the other, as shown in Fig. 1.4. The DC link is supplied by the real power grid through a transformer and an active rectifier. The power flows from the DC link to the AC grid emulation for the generator emulators and from the AC grid emulation to the DC link for the load emulators. Synchronization process uses active power and frequency droop.

The HTB includes two types of cabinets, Type I and Type II. Type I cabinets include four power generation or load emulators, local transmission lines, and/or transformer emulators(inductors). Type II cabinets include two back-to-back converters used to emulate HVDC or long distance ac transmission lines. The converter used for the generation and load emulators and back-to-back converters use 75 kVA commercially available VACON converters. The emulated power system components are implemented using TMS320F28335 digital signal processors (DSPs), which control each converter on the HTB. Power system components that generate voltage and frequency are generally modeled as voltage sources,

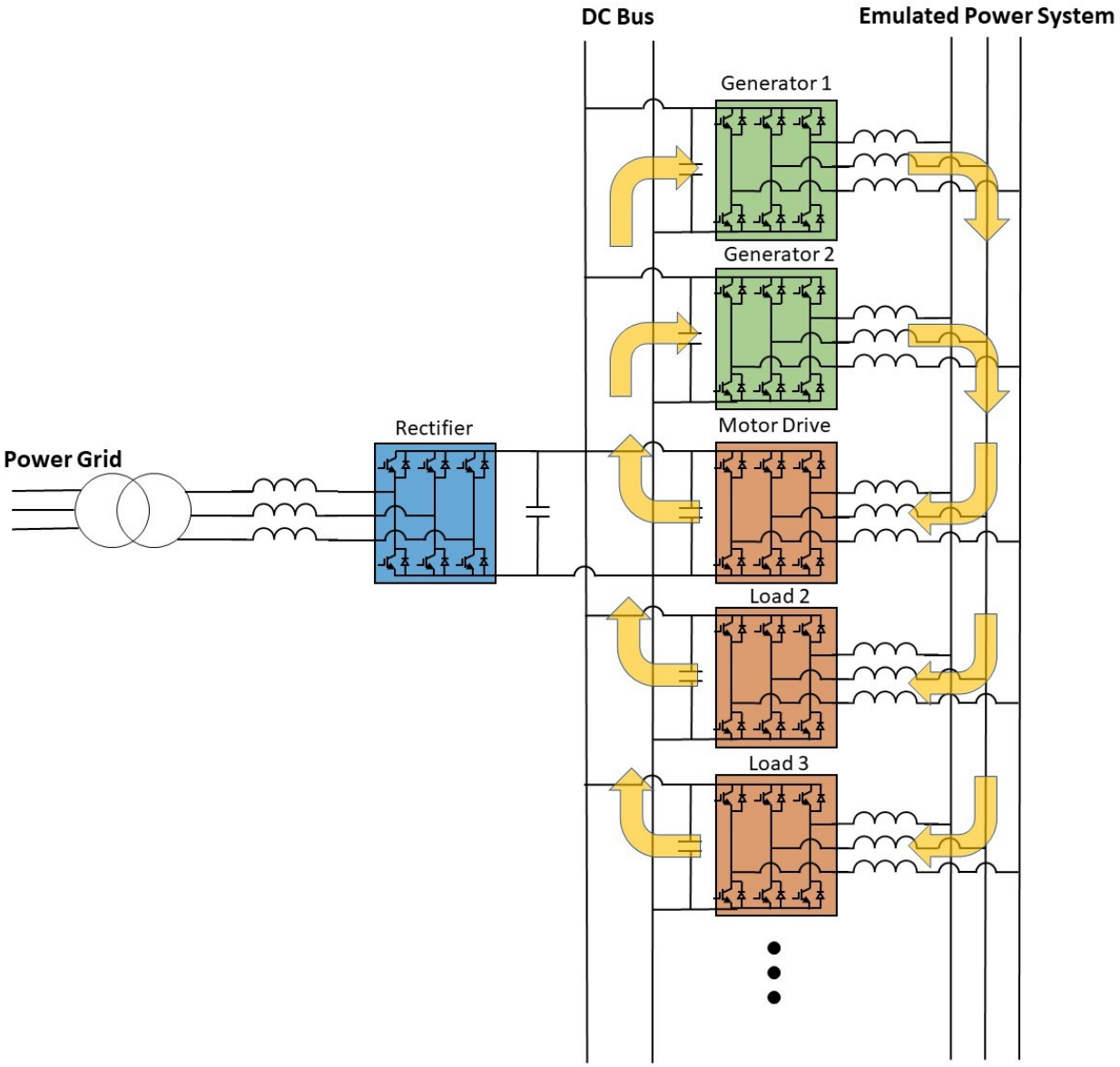


Figure 1.4: Power Circulation within the HTB [2].

and loads are modeled as current sources. Each current source contains an inner current loop and an outer voltage loop, which supplies the dynamic current reference to the inner current loop.

The size of the system that the HTB can emulate is constrained by the availability of hardware. Therefore, the HTB implements a hybrid emulation which integrates the RTDS and the HTB. This is executed using a similar technique as the Power Hardware-in-the-Loop(PHIL) emulation, which uses an interface– both power interface and digital interface– to make two separate emulation subsystems that operate as one large system, shown in Fig. 1.5.

The HTB emulates both Western Electricity Coordinating Council(WECC) as a four area system aggregation, and Electric Reliability Council of Texas (ERCOT) as a single area system aggregation. Additionally the HTB is connected to the Eastern Interconnect, which is modeled in the Real Time Digital Simulator (RTDS)[3]. Fig. 1.6 shows the system overlayed on a map of the United States. A visualization screen, shown in Fig. 1.7, is implemented through LabVIEW, which gathers data from phasor measurement units (PMUs) and frequency-domain reflectometers (FDRs) and is sent through local ethernet to the control screen. The visualization includes real-time values for active power, reactive power, frequency, voltage, and area control.

1.4.3 Existing Emulators

The HTB can be configured to emulate either a microgrid or a 6-area transmission level emulation. The microgrid includes emulations for solar, energy storage, and loads[25]. The microgrid used a dynamic boundary, which leads to better distributed energy resources and improved reliability[26][27]. Other emulations available for the 6-area system grid include a synchronous generator, wind turbine with virtual synchronous generator control, photovoltaics generation, and vanadium and lithium ion battery energy storage systems[28][29][30][31][32]. The load emulators include a 3-phase induction motor, constant ZIP, and VSD connected induction motor. The HTB also emulates three-phase transmission lines, three-phase faults, and multi-terminal high voltage DC (HVDC) [33][34][35][36].

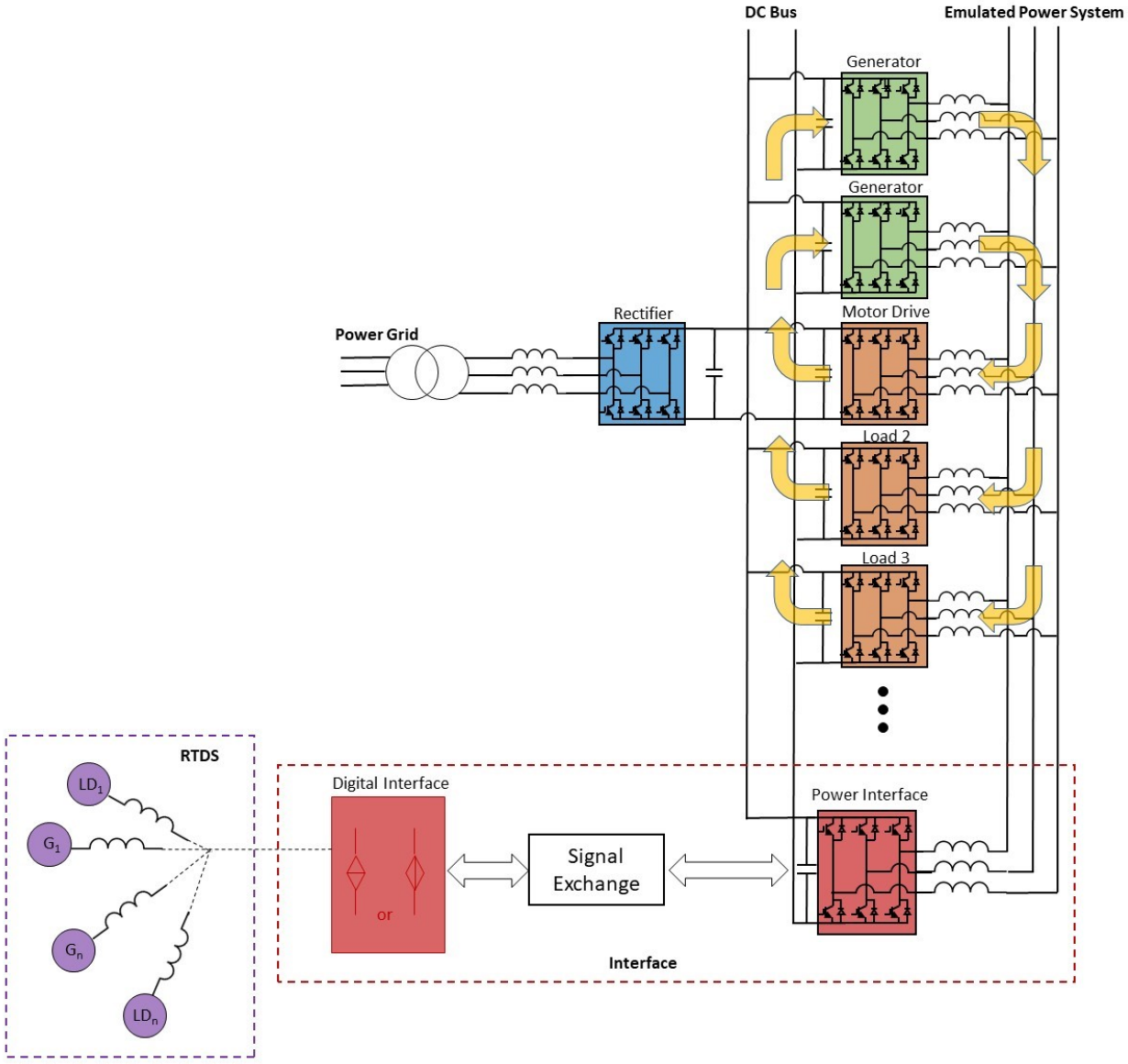


Figure 1.5: HTB and RTDS connection overview [3].

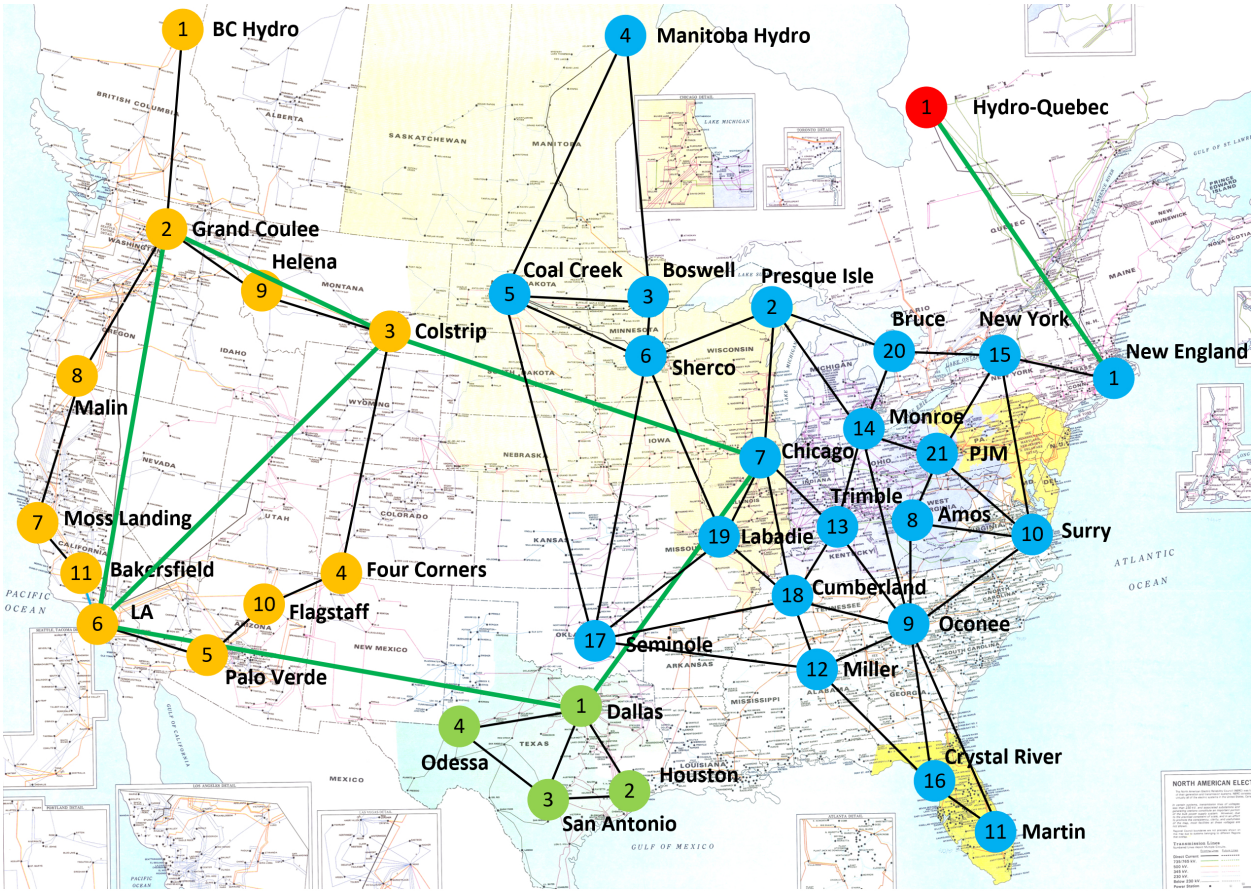


Figure 1.6: Map of emulated HTB system and RTDS overlay on map of United States.

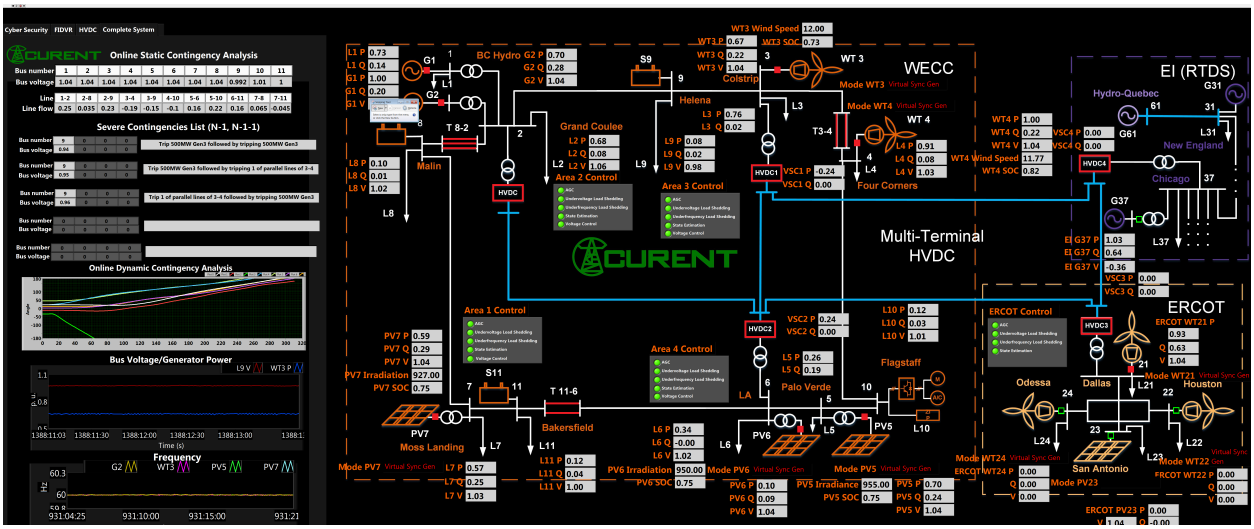


Figure 1.7: HTB visualization wall.

1.5 Project Description

Induction motors make up a significant portion of the load on the power grid. Not only does the implementation of variable speed drives on induction motors provide efficiency savings for the customers, but it also can bring possible benefits to the utility companies through demand response and ancillary services. This project uses the HTB platform and PSCAD/EMTDC to develop, test, and utilize VSD connected industrial induction motors.

With the development of new power devices with wide band gaps, such as SiC and GaN devices, active front end VSDs are growing in popularity. For this reason, an active front end topology is used for the simulation and emulation of the system. Controls are implemented in the VSD, including DC link voltage, inner and outer current loop, and grid frequency regulation. Two different control techniques were used for the grid frequency regulation– one on the WECC system and one on a microgrid system. The different techniques were developed based on the frequency characteristics on both systems.

The model and controls were verified in Matlab/Simulink, on the HTB platform, and in PSCAD/EMTDC.

1.6 Thesis Structure

In Chapter 1, induction motors drives are introduced through their benefits, advantages, and challenges. Additionally, Chapter 1 outlines the use of loads on the grid through ancillary services and demand response. The HTB project has also been described. Chapter 2 contains a literature review about an induction motor emulator, motor drive topologies, wide bandgap device, power electronics modeling and control. Chapter 3 includes a detailed description of the VSD emulator design process including modeling, control design, discrete implementation, and verification via simulation. Chapter 4 describes the experiment process on the HTB for each platforms– WECC and microgrid– and discusses in detail the responses observed. Both platforms are simulated in PSCAD/EMTDC to find system level responses. Finally, Chapter 5 summarizes the conclusions of this work and provides recommendations for future work using the BESS emulator.

Chapter 2

Literature Review

2.1 Induction Motor Emulator

A three phase induction motor is the dominant power system load, particularly for industrial systems. An accurate emulator should include dynamic behaviors in order to emulate overall power system behaviors. The inputs of a three-phase induction motor include three-phase AC stator voltage V_{abc} and electrical frequency ω, and the output is three-phase current I_{abc}. The electrical characteristics are also determined by the mechanical relationship between torque T and rotating speed ω_r. For this model, calculations are done using the dq coordinates, the frequency, and angle that are extracted using PLL from the V_{abc} measurements. Fig. 2.1 illustrates the induction motor load emulator structure. For this model, the calculations are done using the dq coordinates, the frequency, and angle that are extracted using PLL from the V_{abc} measurements[2].

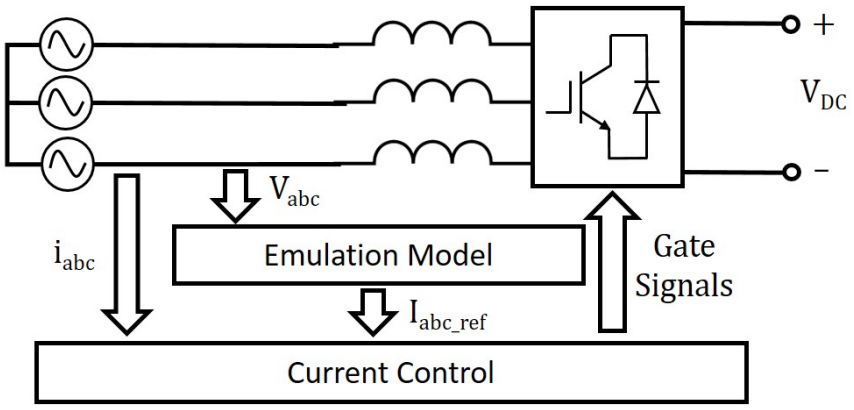


Figure 2.1: The emulator structure for three phase induction motor[2].

$$\begin{bmatrix} {v_{qs}}^{pu} \\ {v_{ds}}^{pu} \\ {v_{0s}}^{pu} \\ {v_{qr}}^{pu} \\ {v_{dr}}^{pu} \\ {v_{0r}}^{pu} \end{bmatrix} = \begin{bmatrix} {r_s}^{pu} & \omega^{pu} \cdot {X_{ss}}^{pu} & 0 & \cdots \\ -\omega^{pu} \cdot {X_{ss}}^{pu} & {r_s}^{pu} 0 & & \\ 0 & 0 {r_s}^{pu} & & \\ 0 & (\omega^{pu} - {\omega_r}^{pu}) \cdot {X_M}^{pu} & 0 & \\ -(\omega^{pu} - {\omega_r}^{pu}) \cdot {X_M}^{pu} & 0 & 0 & \\ 0 & 0 & 0 & \end{bmatrix}$$

$$\begin{bmatrix} 0 & -\omega^{pu} \cdot {X_M}^{pu} & 0 & \\ -\omega^{pu} \cdot {X_M}^{pu} & 0 & 0 & \\ 0 & 0 & 0 & \\ & {r_r}^{pu} & (\omega^{pu} - {\omega_r}^{pu}) \cdot {X_{rr}}^{pu} & 0 \\ -(\omega^{pu} - {\omega_r}^{pu}) \cdot {X_{rr}}^{pu} & {r_r}^{pu} & 0 & \\ 0 & 0 & {r_r}^{pu} & \end{bmatrix} \cdot \tag{2.1}$$

$$\begin{bmatrix} {i_{qs}}^{pu} \\ {i_{ds}}^{pu} \\ {i_{0s}}^{pu} \\ {i_{qr}}^{pu} \\ {i_{dr}}^{pu} \\ {i_{0r}}^{pu} \end{bmatrix} + \begin{bmatrix} X_{ss}^{pu} & 0 & 0 & X_M^{pu} & 0 & 0 \\ 0 & X_{ss}^{pu} & 0 & 0 & X_M^{pu} & 0 \\ 0 & 0 & X_{ls}^{pu} & 0 & 0 & 0 \\ X_M^{pu} & 0 & 0 & X_{rr}^{pu} & 0 & 0 \\ 0 & X_M^{pu} & 0 & 0 & X_{rr}^{pu} & 0 \\ 0 & 0 & 0 & 0 & 0 & X_{lr}^{pu} \end{bmatrix} \cdot \frac{1}{\omega_b} \cdot \frac{d}{dt} \begin{bmatrix} {i_{qs}}^{pu} \\ {i_{ds}}^{pu} \\ {i_{0s}}^{pu} \\ {i_{qr}}^{pu} \\ {i_{dr}}^{pu} \\ {i_{0r}}^{pu} \end{bmatrix}$$

$$T_e = (\frac{3}{2})(\frac{P}{2})(\lambda_{ds} i_{qs} - \lambda_{qs} i_{ds}) \tag{2.2}$$

$$\omega_r = \int_0^t \frac{T - T_L - T_{fri}}{2H} d\tau \tag{2.3}$$

Since the motor model equations are using the reference frame of synchronous rotating speed, the input voltages are constant in the dq domain. Equations (2.1)-(2.3) model the electromagnetic and electromechanical relationship between flux, current, voltage, and rotational speed. The variables are defined as follows: v_{qs}, v_{ds} and v_{0s} are stator voltage transformed in $dq0$ domain, v_{qr}, v_{dr} and v_{0r} are rotor voltage transformed in $dq0$ domain, ω is angular speed of reference frame, ω_r is rotating angular speed of the motor, r_s and r_r are stator and rotor resistances, X_{ls} and X_{lr} are stator and rotor leakage reactance, X_{ss} and X_{rr} are stator and rotor reactance, X_M is magnetizing reactance, p is pole pair number, λ_{qs} and λ_{ds} are q and d axis flux for stator, i_{qs} and i_{ds} are currents on q and d axis for the stator, and H is inertia constant of motor. Equation (2.1) contains derivative variables and must be solved during each iteration to maintain system stability and accuracy. Equation (2.1) can be simplified to the form shown in (2.4), where vector $\vec{y}$ can be solved: $\vec{y} = \begin{bmatrix} {i_{qs}}^{pu} & {i_{ds}}^{pu} & {i_{0s}}^{pu} & {i_{qr}}^{pu} & {i_{dr}}^{pu} & {i_{0r}}^{pu} \end{bmatrix}^T$.

$$\frac{d}{dt}\vec{y} = \mathbf{A} \cdot \vec{y} + \mathbf{b} \tag{2.4}$$

Matrices $\boldsymbol{A}$ and $\boldsymbol{b}$ can be derived from (2.1), and the numerical method, Runge-Kutta 4th order, is applied to (2.4), the simplified equation of (2.1).

$$\frac{d}{dt}\vec{y} = f(t, \vec{y}), \qquad \vec{y}(t_0) = 0 \tag{2.5}$$

$$\vec{y}_{n+1} = \vec{y}_n + \frac{1}{6}(k_1 + 2k_2 + 2k_3 + k_4) \tag{2.6}$$

where,

$$k_1 = \Delta t \cdot f(t_n, \vec{y}_n)$$

$$k_2 = \Delta t \cdot (t_n + \frac{1}{2}\Delta t, \vec{y}_n + \frac{1}{2}k_1)$$

$$k_3 = \Delta t \cdot (t_n + \frac{1}{2}\Delta t, \vec{y}_n + \frac{1}{2}k_2)$$

$$k_4 = \Delta t \cdot (t_n + \frac{1}{2}\Delta t, \vec{y}_n + \frac{1}{2}k_3)$$

Each iteration corresponds with the switching cycle of the HTB converters. With ideal voltage and frequency inputs, the induction motor model starts up with smooth fluctuation transients. The starting current for an induction motor in dq domain could be as high as 2-3 times that of normal rated current. The starting time takes around 5.5 s under this case.

2.2 Active Front End vs Diode Front End Motor Drive

Active front end (AFE) and diode front end (DFE) differ in the semiconductors used in the rectifier stage of the conversion process. As the name indicates, diode front end motor drives have a diode bridge as the rectifier and IGBTs on the back end as the inverter. Fig. 2.2 shows the schematic of a diode front end converter. Diode rectifiers cause major distortion on the grid because of the distortion in the current[37]. However, active front end motor drives replace the traditionally used diodes with IGBTs, shown in Fig. 2.3[37]. The implementation of AFE has become increasingly popular because of the decreasing cost of power switches[38]. Active front end motor drives reduce harmonic distortion, which are then added back to the power system by controlling to feed a sinusoidal current back to the grid. In addition to reducing the harmonic distortion, active front end drives allow for more control and for grid regulation. The inverter can control the motor, and rectifier controls can provide grid support. AFE-VSDs are becoming the standard solution for large-power medium-voltage VSDs[37]. While AFE has some benefits to DFE, there are some disadvantages, including complicated control, potential resonance, and bulky and expensive LCL filter[39].

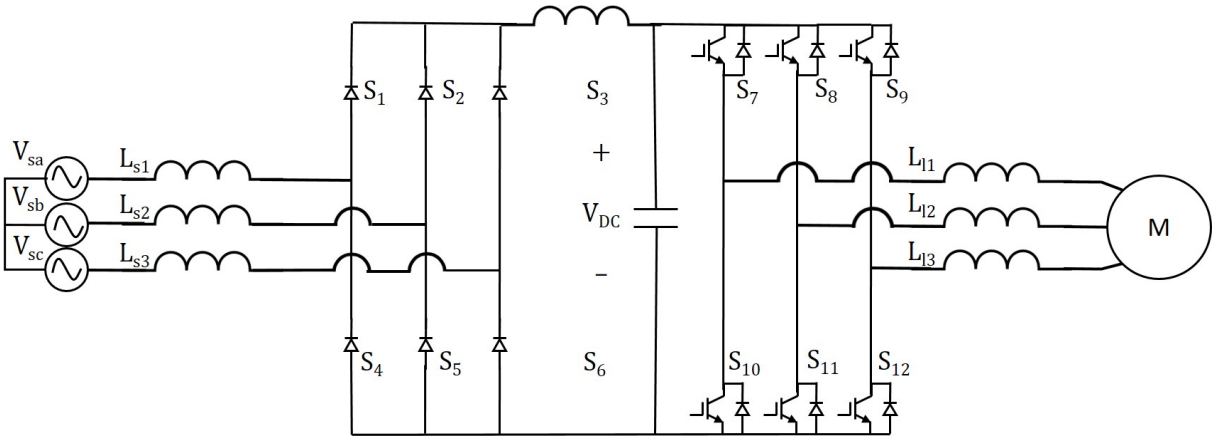


Figure 2.2: Diode Front End Motor Drive.

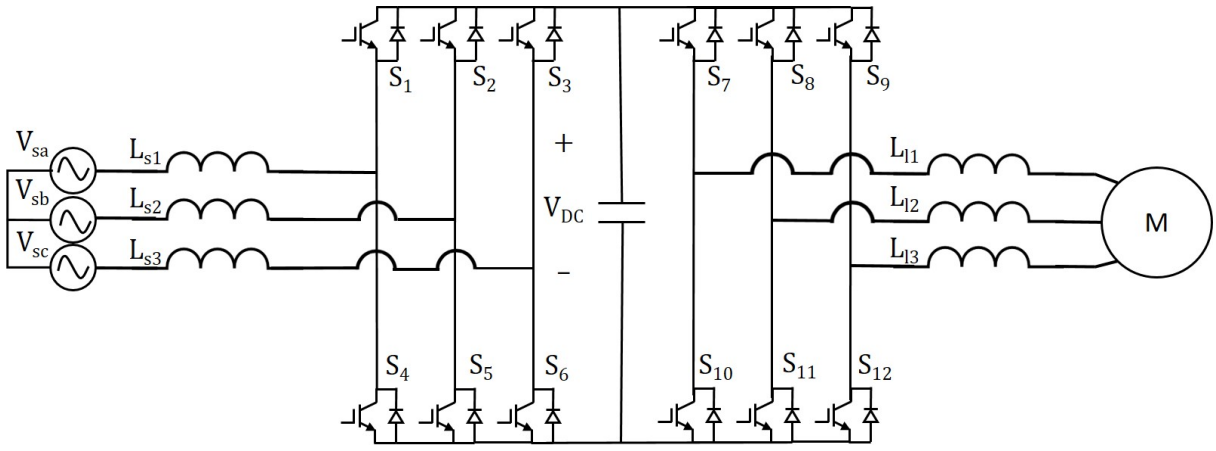


Figure 2.3: Active Front End Motor Drive[37].

2.3 Wide Bandgap Power Devices and VSDs

Most current commercial power electronics converters use silicon-based power devices. However, many utility applications need devices, which have properties that exceed the limits of silicon fundamental material properties. Silicon unipolar devices, such as the MOSFET, can not be economically scaled to voltages higher than 600 V[40]. In higher voltage applications, current state- of- the- art bipolar IGBT is used. However, wide bandgap (WBG) power device, with a high bandgap (E_g), present opportunities for improved power electronics performance, such as high blocking voltages, efficiency and reliability. Despite the apparent benefits in efficiency and reliability, there are still some barriers to integration, including cost of WBG power devices and electromagnetic interference.

Wide bandgap semiconductors' electrical characteristics have the potential to improve efficiency and reliability in power electronic converters. Table 2.1 shows the electrical properties of silicon and prominent WBG semiconductors[40]. Fig. 2.4 compares silicon, silicon carbide, and gallium nitride. Table 2.1 and Fig. 2.4 show that GaN and SiC both have higher bandgap and electric breakdown field, E_c, which allows for higher breakdown voltages. SiC has a clearly superior thermal conductivity, λ, which makes it preferable for high temperature applications. Finally, GaN and and SiC have higher electron velocity, v_s, which allows for high frequency switching.

The current market projects that GaN will dominate the high frequency market, and SiC will dominate the market at high voltages. Fig. 2.5 shows the evolution of WBG power electronics technologies. According to this projection, GaN is expected to dominate the low- voltage point-of-load (POL) power converters used in battery powered wireless original equipment manufacturing (OEM) devices, and power supplies requiring blocking voltages below 900 V[43]. SiC is expected to dominate the medium voltage and high voltage applications. The integration of SiC power devices for utility applications are projected to improve performance in higher blocking voltages, increased efficiency, and reliability[42]. Specifically in the case of active front end VSDs, SiC has been shown to improve efficiency by 1.2% over traditional Si devices[44].

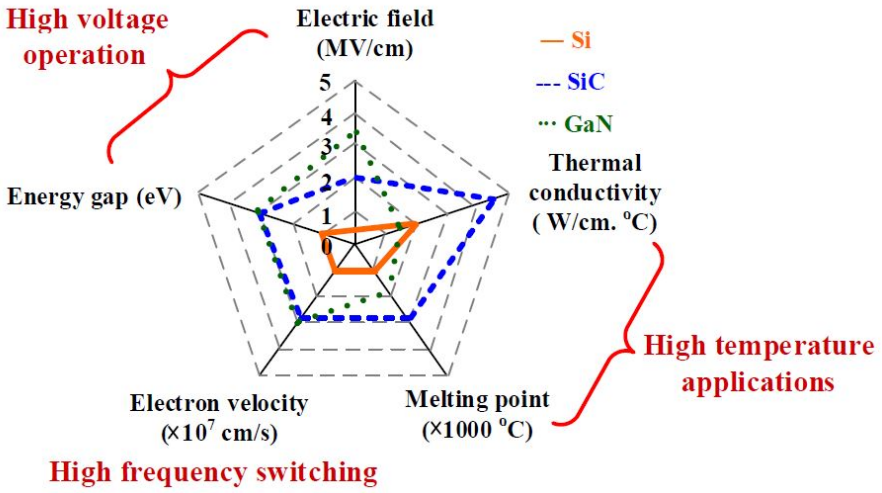


Figure 2.4: Properties of WBG materials[41].

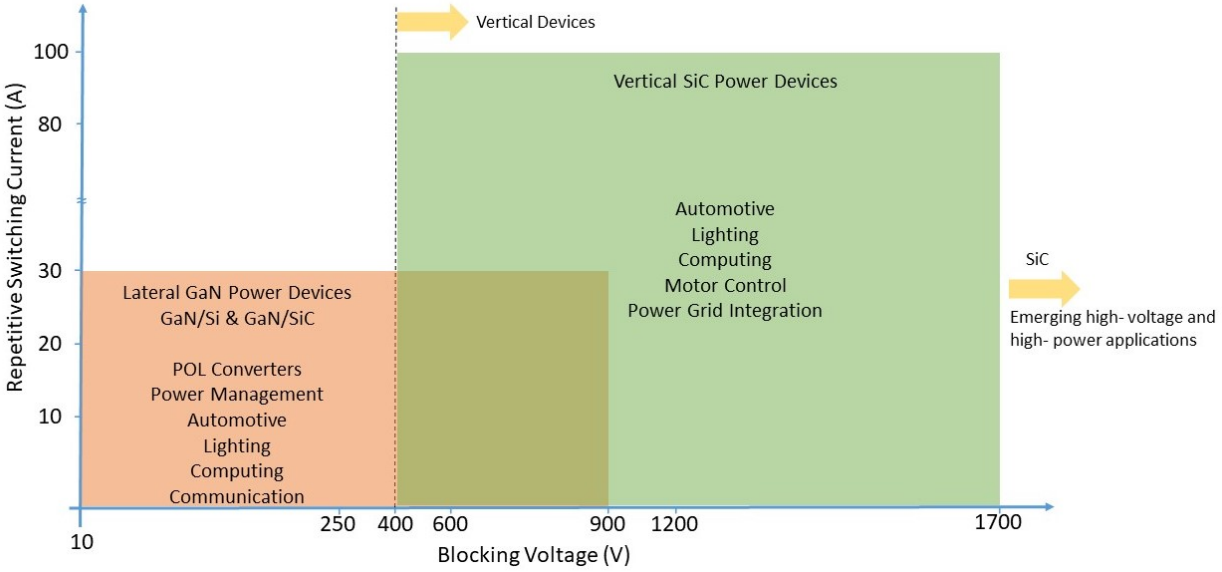


Figure 2.5: Expected evolution of WBG power electronics technologies[43].

Table 2.1: Properties of Silicon and dominate WBG semiconductors [42].

Property	Si	6H-SiC	4H-SiC	GaN
Bandgap, E_g (eV)	1.12	3.03	3.26	3.45
Dielectric constant, ϵ_r	11.9	9.66	10.1	9
Electric breakdown field, E_c (kV/cm)	300	2500	2200	2000
Electron mobility, μ_n (cm^2/Vs)	1500	500	1000	1250
Hole mobility, μ_n (cm^2/Vs)	600	101	115	850
Thermal conductivity, λ (W/cmK)	1.5	4.9	4.9	1.3
Saturated electron drift velocity, v_s ($x10^7$ cm/s)	1	2	2	2.2

2.4 Motor Drive Modeling

The motor drive can be modeled by an AC to DC converter connected to a DC to AC converter by a DC link capacitor. Then, the system can be represented by average models of both power converters and mathematical models of the passive components. The modeling techniques and control for the motor drive are described in this section.

2.4.1 Passive Component Modeling

Capacitors and inductors are modeled using mathematical equations. The equations used to describe the voltage and current for capacitors and inductors are shown in (2.7) and (2.8).

$$v_C(t) = \frac{1}{C}\int_{-\infty}^{t} i_C(t)dt \tag{2.7}$$

$$i_L(t) = \frac{1}{L}\int_{-\infty}^{t} v_L(t)dt \tag{2.8}$$

where $v_L(t)$ is the voltage across the inductor and $i_C(t)$ is the current through the capacitor.

The discrete forms of the same equations are given in (2.9) and (2.10).

$$v_C[x] = v_C[x-1] + \frac{i_C(t)}{C}T_s \tag{2.9}$$

$$i_L[x] = i_L[x-1] + \frac{L_L(t)}{L}T_s \tag{2.10}$$

where, T_s is the switching period.

2.4.2 Power Electronics Modeling

Power electronic converters can be modeled as average circuit models, which neglect switching ripple but provide average DC component waveforms. This simplifies circuit analysis, and allows fast calculation of converter states.

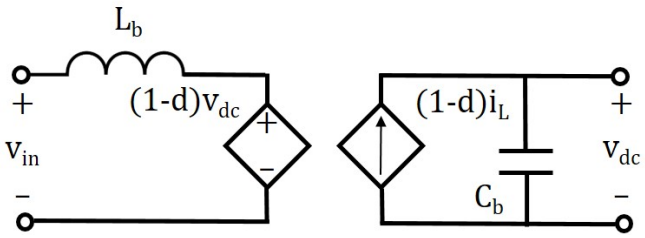


Figure 2.6: The average model for half-bridge switching circuit.

An average model gives the average response for each cycle that the switch is on, otherwise referred to as a switch's duty cycle. With this technique, a half bridge can be modeled by a duty-cycle dependent voltage source and a duty-cycle dependent current source, shown in Fig. 2.6. Using the average model, inductor volt-second balance and capacitor charge balance can be applied to obtain DC inductor current and capacitor voltage. Inductor volt-second balance and capacitor charge balance dictate that DC inductor voltage and capacitor current must equal zero within each switching cycle.

For AC to DC converters, the average model is further simplified using the synchronous direct-quadrature (dq) coordinate system. The dq coordinate system uses a rotating reference frame to simplify the sinusoidal voltage and current coordinates to dc-like dq coordinates. The dq coordinates are calculated using the Park and Clarke transformations, which are represented in the following transformation matrix:

$$Y = \sqrt{\frac{2}{3}} \begin{bmatrix} cos(\omega t) & cos(\omega t - \frac{2\pi}{3}) & cos(\omega t + \frac{2\pi}{3}) \\ -sin(\omega t) & -sin(\omega t - \frac{2\pi}{3}) & -sin(\omega t + \frac{2\pi}{3}) \\ \sqrt{\frac{1}{2}} & \sqrt{\frac{1}{2}} & \sqrt{\frac{1}{2}} \end{bmatrix} \tag{2.11}$$

Motor drives have two conversion states, as discussed in Section 1.1.1. The AC to DC conversion is done using a rectifier. Using the method discussed in Section 2.4.2, an average model for the rectifier can be developed. Fig. 2.7 shows a rectifier average model in ABC coordinates, and Fig. 2.8 shows a rectifier average model in dq coordinates, where $\overline{v}$ is the moving average of the voltage, and $\overline{i}$ is the moving average of the current.

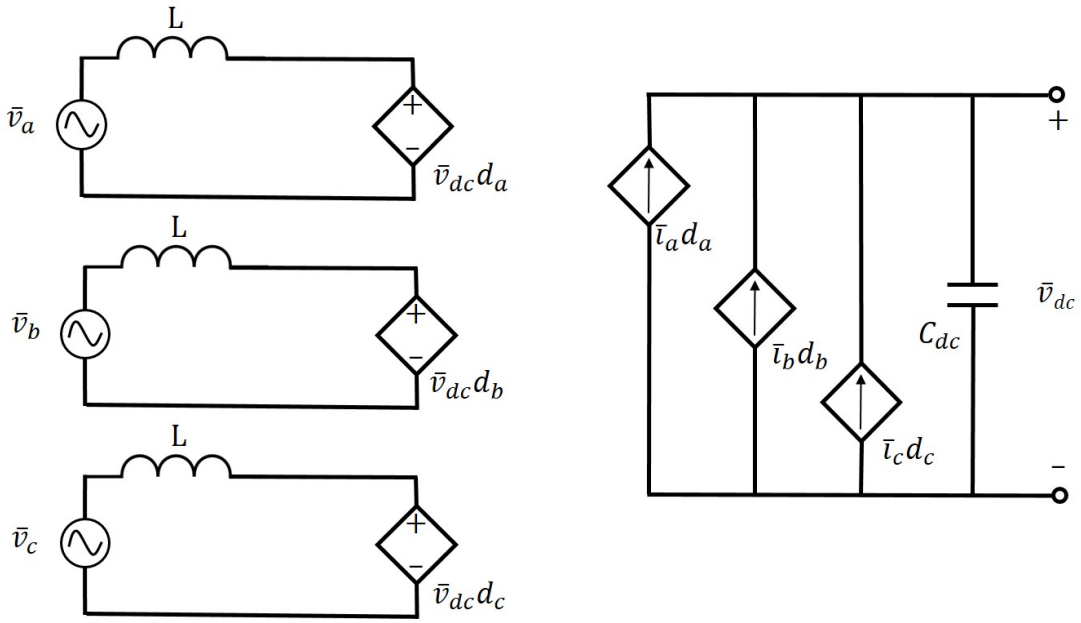


Figure 2.7: Average model of a rectifier in ABC coordinates [45].

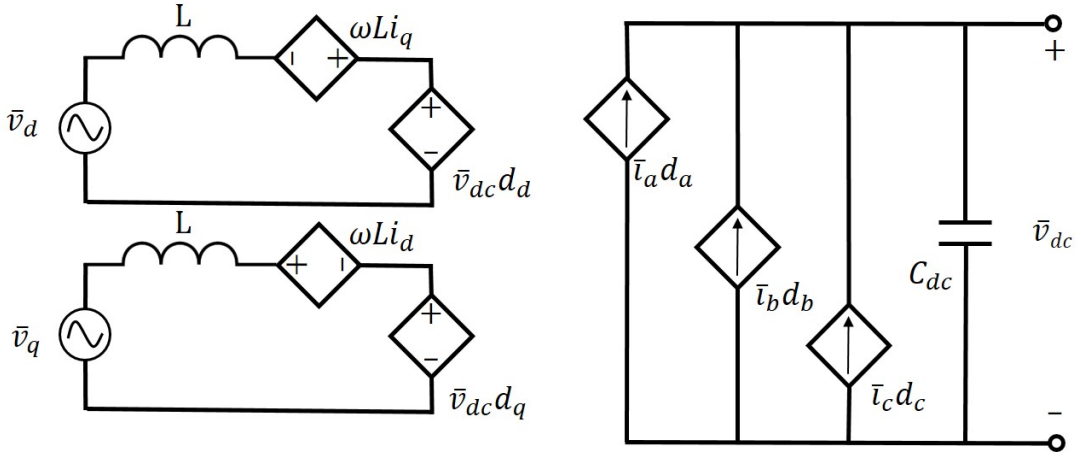


Figure 2.8: Average model of a rectifier in DQ coordinates[45].

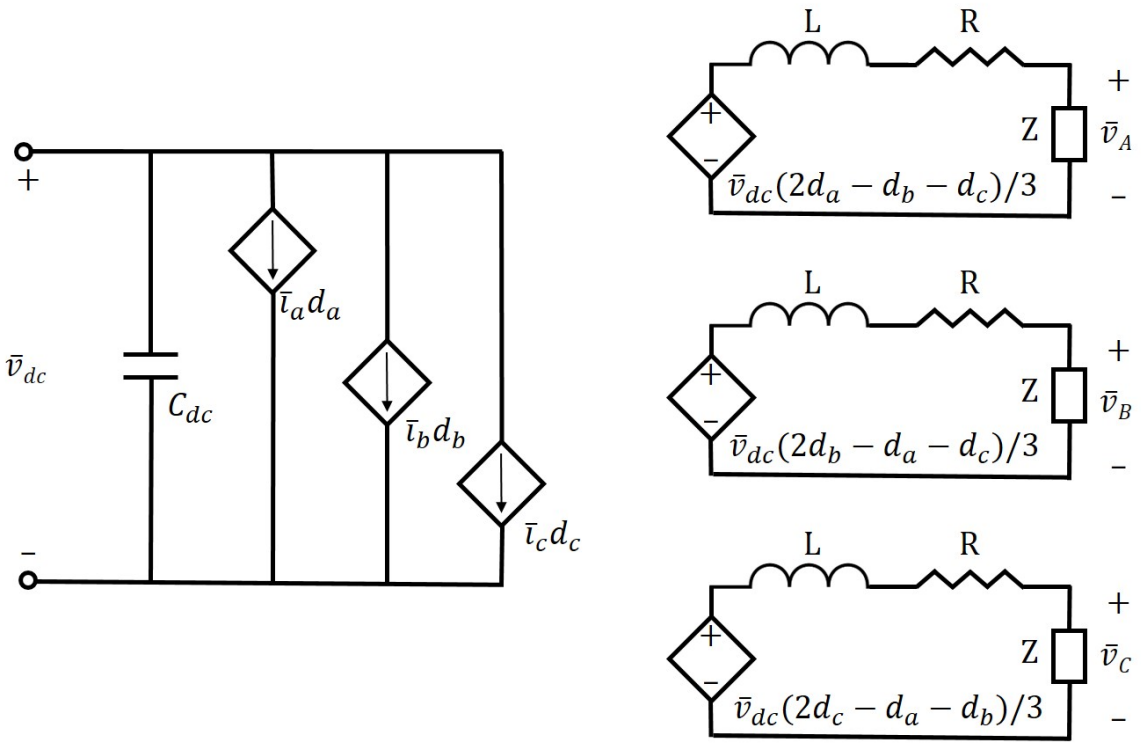


Figure 2.9: Average model of a VSI in ABC coordinates[45].

The second conversion state is DC to AC, which is done using a voltage source inverter(VSI). Using the method discussed in Section 2.4.2, an average model for the VSI can be developed. Fig. 2.9 shows a VSI average model in ABC coordinates, and Fig. 2.10 shows a VSI average model in *dq* coordinates.

2.5 Motor Drive Front End Controls

Both conversion states can be used for control because the use of an active front end motor drive. There are five major controls within this motor drive model: Inner and outer loop current control, DC link voltage control, grid voltage regulation, and grid frequency support.

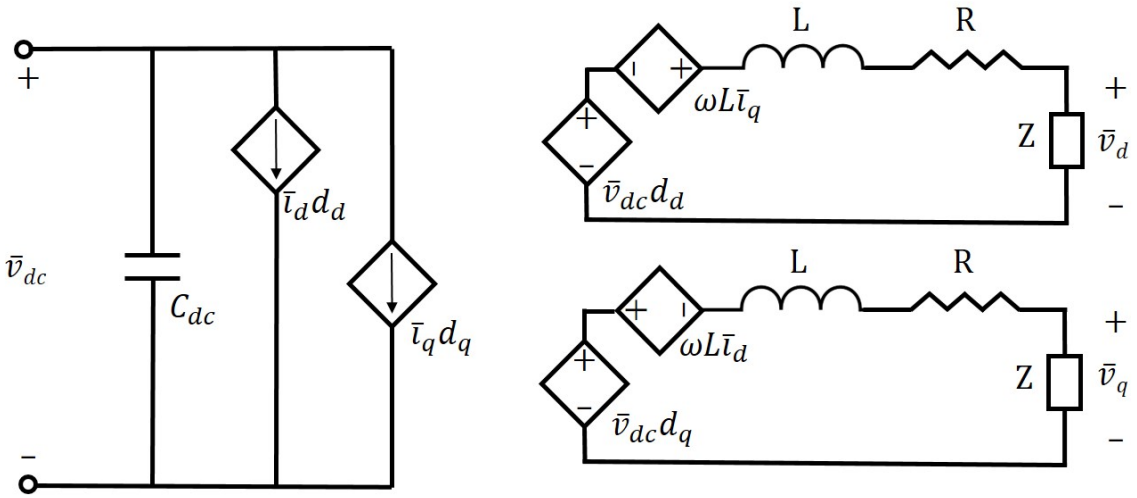


Figure 2.10: Average model of a VSI in DQ coordinates[45].

2.5.1 Current Control

For this emulator there are two current controls. However, a basic PI control technique is used for both controls, shown in Fig. 2.11[46]. This control is a PI control designed in a dq frame with decoupled d and q axes. The PI controller design is done with an L approximation of the LCL filter ($L_f = L_{fg} + L_{fc}$), where L_{fg} and L_{fc} are the grid side filter inductance and the converter side filer inductance, respectively. The low frequency behavior of the LCL filter is similar to the L filter, so at low frequencies, the filter can be approximated by the L components.

2.5.2 DC Link Control

The DC link control isolates the grid voltage from the motor output voltage by controlling the DC voltage link between the rectifier and inverter, refer to Fig. 2.3. The DC link control uses a basic PI control shown in Fig. 2.12[47].

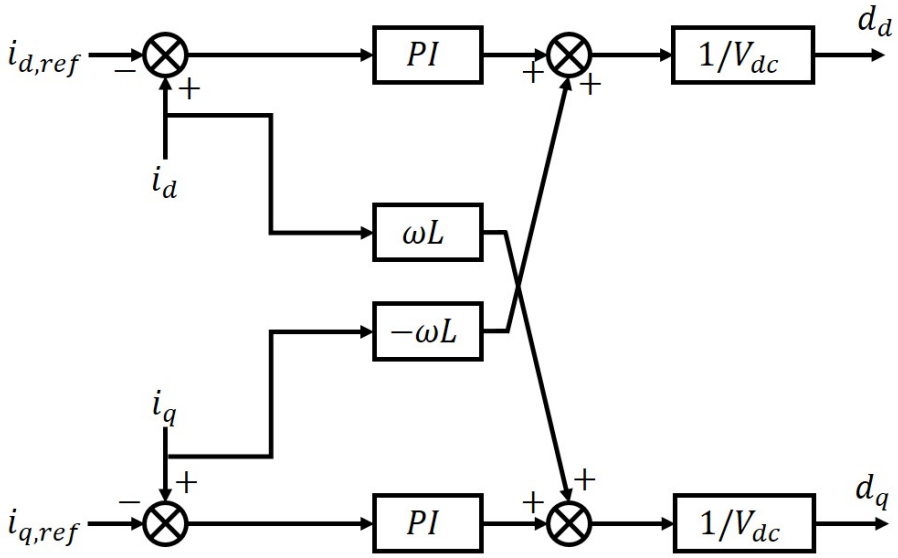


Figure 2.11: Basic PI current control[46].

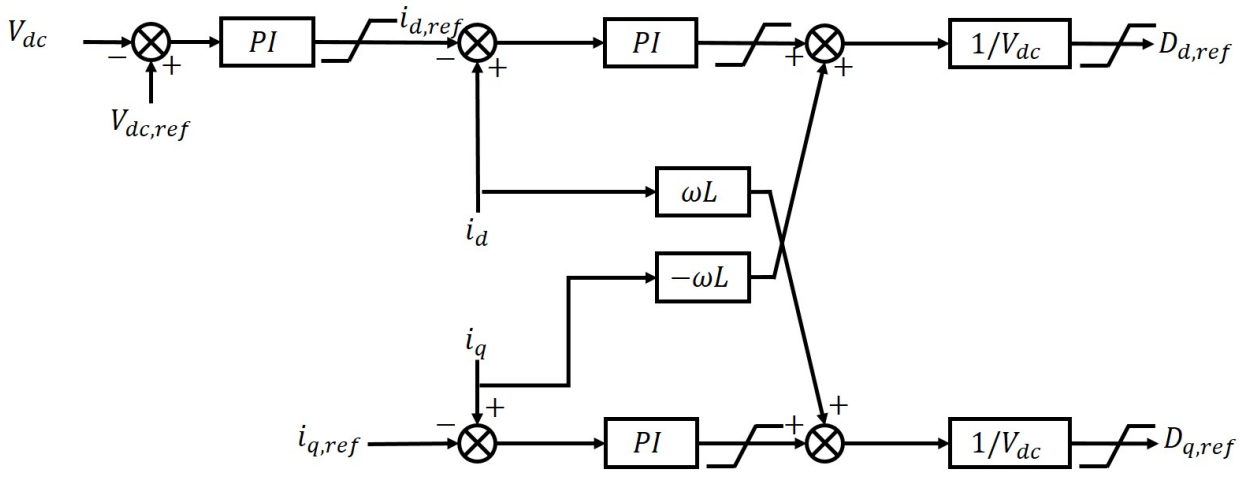


Figure 2.12: DC voltage link control[47].

2.6 Motor Drive Back End Controls

2.6.1 Motor Constant V/f Control

In V/f control, the speed of the induction motor is controlled by adjusting the magnitude of the stator voltages and frequencies. Traditionally, this is used to maintain the air gap flux value at steady state. Fig. 2.13 shows the simplified circuit of the steady state equivalent circuit of the induction motor. In this case, the stator resistance (R_s) is assumed to be zero and leakage inductance (L_l) refers to the total leakage inductance, which is the combination of stator and rotor inductance ($L_l = L_{ls} + L_{lr}$). The leakage inductance, L_l, represents the amount of air gap flux. The magnetizing current that generates the air gap flux can be approximated by the ratio of the stator voltage and frequency. This ratio is shown in (2.12) in phasor representation. If the motor is operating in the linear magnetic region, the L_m is constant. In which case, (2.12) can be rewritten in terms of magnitude, shown in (2.13). From this equation, it can be concluded that if the ratio V/f is constant for any change of f, then flux remains constant and the torque becomes independent of the supply frequency. Because the slip is a function of the motor load, at no-load torque, the slip is very small, and the speed is nearly the synchronous speed. Therefore, the simple open loop V/f system cannot precisely control the speed with a presence of load torque. If a slip compesation is added with a speed measurement, the closed loop V/f system can be shown in Fig. 2.14. However, in practice, a lower limit on the frequency and a maximum at the rated voltage can be set, shown in Fig. 2.15. This approach works for fans and blower drives where the speed response at the low end is not critical[48].

$$\tilde{I}_m \cong \frac{\tilde{V}_s}{j\omega L_m} \tag{2.12}$$

$$I_m \cong \frac{V_s}{(2\pi f)L_m} \tag{2.13}$$

V/f control is used to change voltage at the terminal of the induction motor proportionally to the change of motor reference speed [48], i.e.

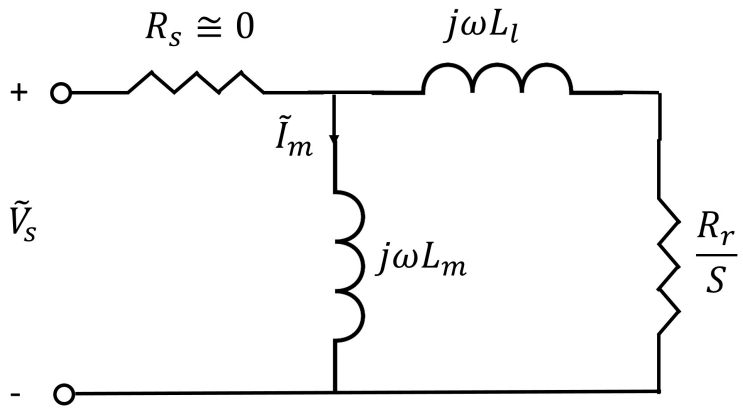


Figure 2.13: Simplified steady state equivalent circuit of induction motor[48].

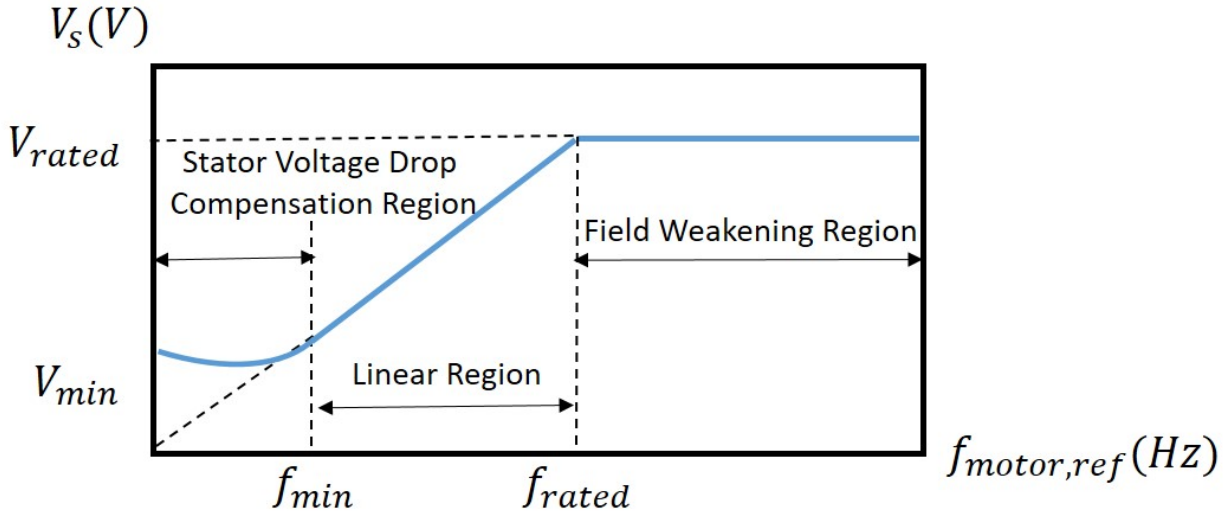


Figure 2.14: Stator voltage vs. frequency profile under V/f control[48].

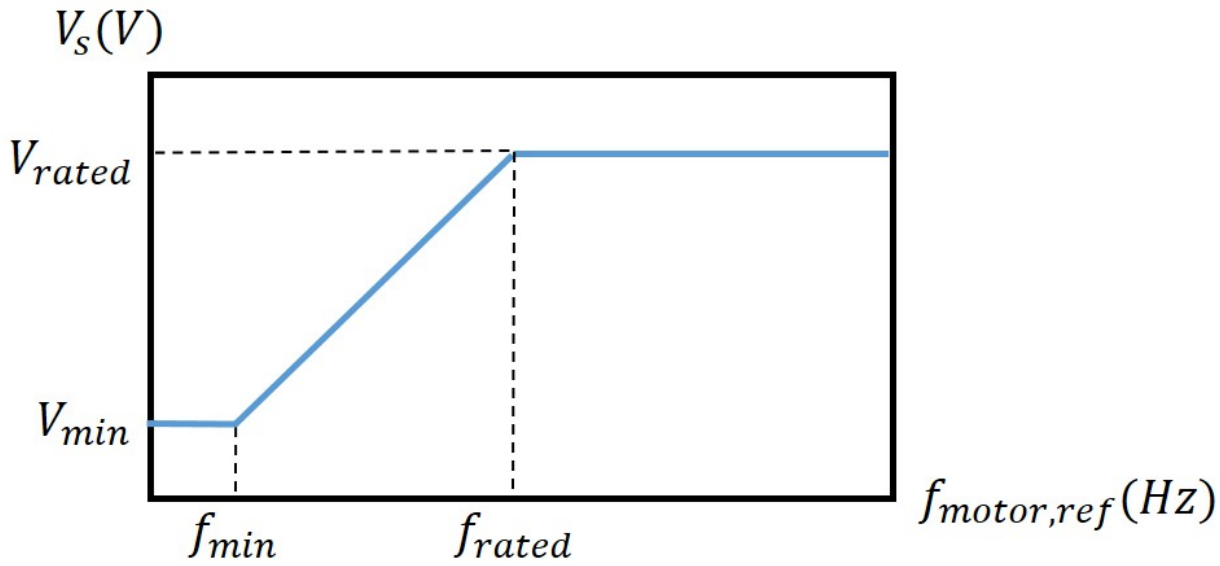


Figure 2.15: Modified V/f profile[48].

$$V_{dinv,ref} = \frac{V_{nom}}{f_{nom}} * f_{ref} \tag{2.14}$$

where $V_{dinv,ref}$ is the output reference voltage for the inverter.

Fig. 2.16 shows the torque-speed characteristics of an induction motor, which can be derived from the equivalent curcuit of an induction motor. As speed increases, the current slowly decreases until the torque reaches its maximum point. Then, the current drops quickly until both the torque and current are at the rated values. When the speed of the motor is changed, the torque and current of the motor will also be affected. When the speed of the motor is decreased to 50%, the motor will often transition past the breakdown torque. This means the relationship between speed and torque, and in turn current, will not be linear.

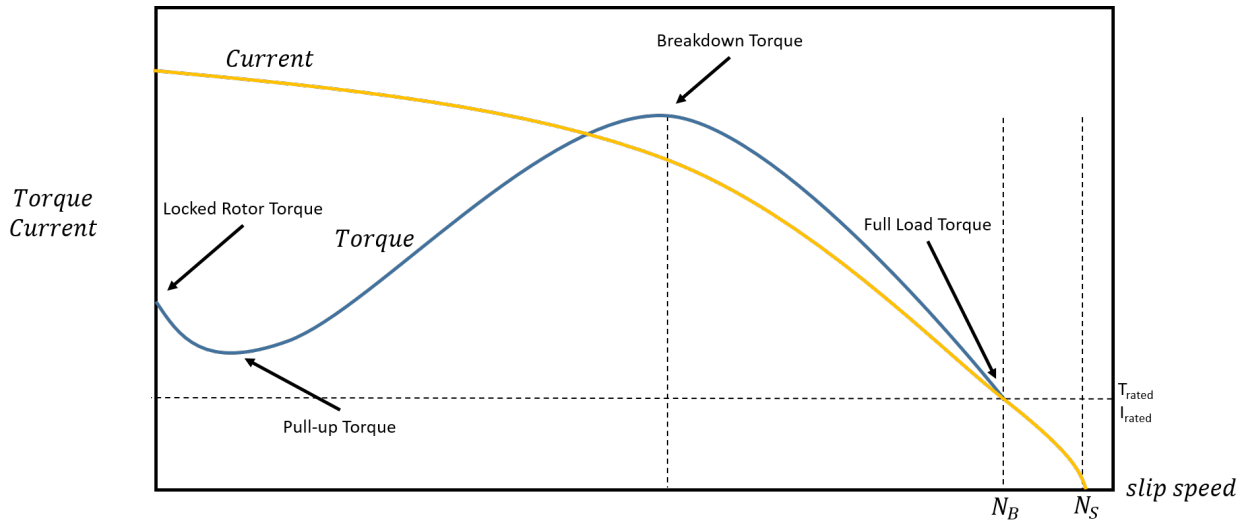
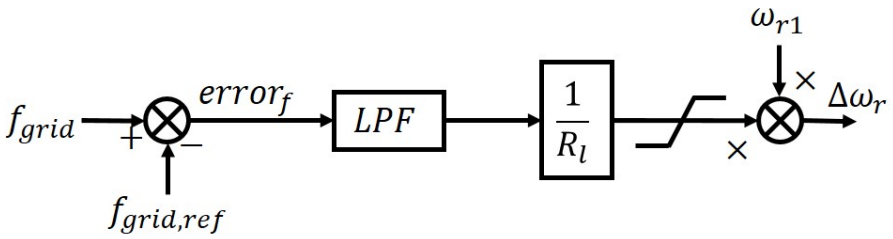


Figure 2.16: Torque and speed curves for an induction motor.

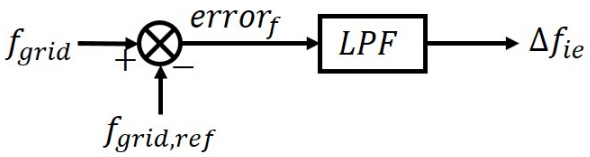
2.7 Grid Frequency Support using VSD

2.7.1 Grid frequency support using variable motor speed

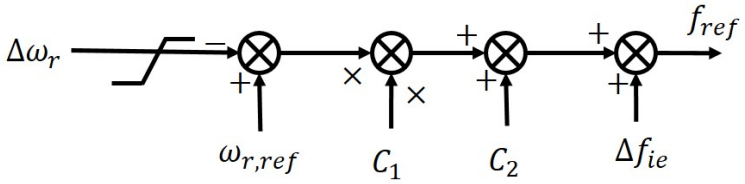
Adjustable speed drives are generally controlled using constant V/f control discussed in 2.6.1[49]. Using this method of control, the power from the motor can be reduced by reducing the motor speed. The inertia response of a line connected motor is emulated using the frequency response control. However, this control adds the primary frequency control. The frequency control reference in [49] uses a phase-lock loop (PLL) to measure the grid frequency. The grid frequency and the initial motor speed are the inputs for the system. The control scheme is shown in Fig. 2.17. The control includes primary frequency control (2.17a), inertia emulator (2.17b), and the speed controller 2.17c. f_{grid} is the PLL measured value for the grid frequency, R_l refer to the droop gain, $\omega_{r,ref}$ is the pre-event motor reference speed, and C_1 and C_2 are coefficients based on induction motor parameters[50]. Some common values for C_1 and C_2 are shown in Table 2.2.



(a) Primary controller.



(b) Inertia emulator.



(c) Speed controller.

Figure 2.17: The block diagram of the primary controller (2.17a), inertia emulator (2.17b), and the speed controller 2.17c[49].

Table 2.2: Derived coefficients for induction motors [50].

Motor Type	Ventilation	Small Industrial	Large Industrial
C_1	0.86268	0.96761	0.99653
C_2	0.10306	0.03777	0.01201

Another method for grid frequency support is inertia emulation using the DC voltage link in the VSD. This is a method commonly used for wind turbines or multi-terminal HVDC(MTDC) systems[51]. In this method when used for MTDC, both the electric energy stored in the DC link capacitors and the energy transferred from the remote grid side to the main AC transmission grid are used to regulate the grid frequency. This control method is shown in Fig. 2.18. The $V_{dc,ref}$ changes according to the deviation of the grid frequency, which can be expressed in 2.15:

$$K_c \cdot (f_{meas} - f_{nom}) + V_{dc,nom} = V_{dc,ref} \tag{2.15}$$

where K_c is the proportional control parameter of the VSC, f_{nom} is the initial frequency reference, f_{meas} is the real time grid frequency, and $V_{dc,nom}$ is the initial DC link voltage reference. The active power contribution of the DC link capacitor after a grid disturbance can be expressed in 2.16:

$$\Delta P_{VSC}(p.u.) = \frac{NCV_{dc,nom}}{S_{VSC}} \cdot \frac{dV_{dc,ref}}{dt} = \frac{NK_cCV_{dc,nom}}{S_{VSC}} \cdot \frac{df_{meas}}{dt} \tag{2.16}$$

where N is the number of the DC link capacitors, S_{VSC} is the rated power of the VSC.

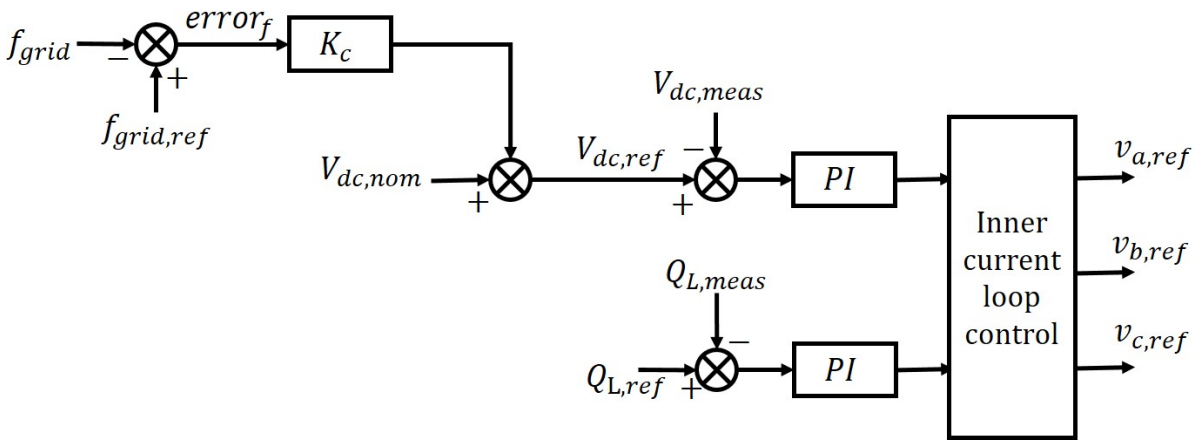


Figure 2.18: VSC inertia emulation control[51].

2.8 Chapter Summary

Induction motors can be modeled using the AC stator voltage, electrical frequency, and relationship between T and ω_r. The output of this model is three-phase current. VSDs have two general topologies, active front end and diode front end. This chapter compares the two topologies and discusses the effect wide bandgap devices have on VSDs. VSDs can be modeled by average models and passive components can be modeled by their governing voltage and current equations. There are numerous possible controls of the VSD depending on topologies used, including DC link voltage, inner and outer current loop, and grid frequency regulation.

Chapter 3

Emulator Design

The electrical topology shown in Fig. 3.1 was chosen for the VSD and induction motor emulator. An active front end VSD was chosen for this application given the flexibility of control and reduction of line voltage harmonics. Fig. 3.2 shows the control method used for the implementation of the VSD and induction motor emulator. Each emulator on the HTB have the same inner current loop for the VSI, which is shown in Fig. 3.3. In this case, $i_{d,ref}$ and $i_{q,ref}$ are the calculated reference values from the active front-end VSD. The final output of the emulator is the duty cycle reference for the HTB VSI. The DC voltage control is implemented in the rectifier, and a grid frequency control is implemented in the inverter of the VSD. The emulation model is simulated in Matlab/Simulink, and the behavior is verified.

3.1 Induction Motor Model

The induction motor model discussed in Section 2.1 is used for the emulation model. Fig. 3.4 shows the model structure. The calculations begin from the calculated values of the inverter voltages, $V_{dq,inv}$. Using Eq. (2.1)- (2.3) and the mathematical method described in Eq. (2.4)-(2.6), the reference currents for the motor model can be calculated. The reference currents are then used as the three phase current reference for the inverter calculations, $I_{dq,inv}$. Table 3.1 shows the parameters used for a medium voltage induction motor (per unit values).

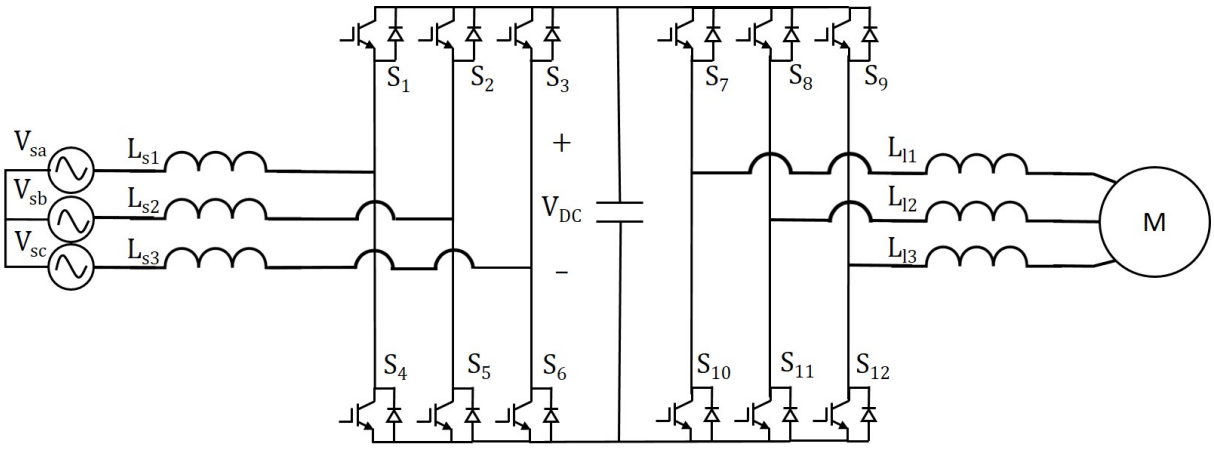


Figure 3.1: Active front end motor drive topology for emulation.

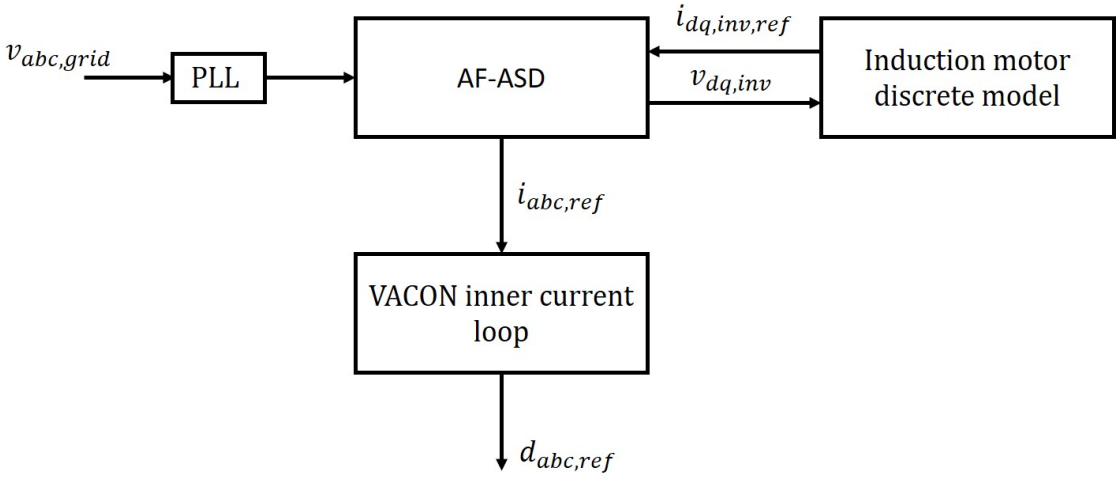


Figure 3.2: Overview of control method used for the implementation of the VSD and induction motor emulator.

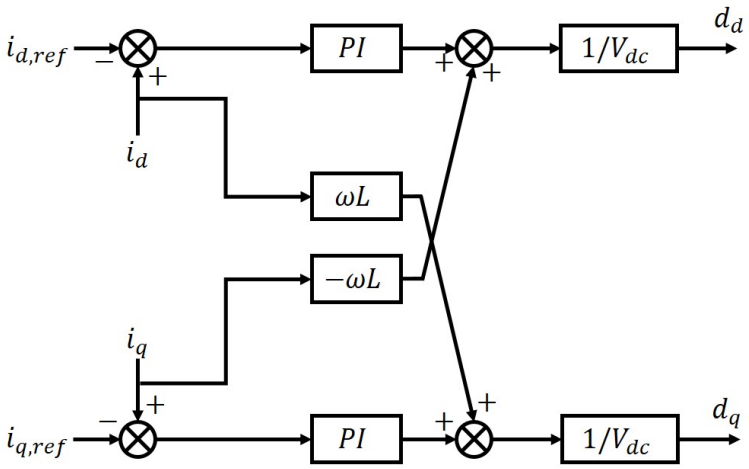


Figure 3.3: Inner current loop of HTB VACON.

Table 3.1: Values for designed motor emulation.

Variable	Emulation Value (p.u.)
X_{lr}	0.0916
X_{ls}	0.061
X_m	2.11
X_{rr}	2.2
X_{ss}	2.1696
r_r	0.0076
r_s	0.0104

3.2 VSD Model

The VSD design is based on an active front-end VSD, shown in Fig. 3.1. Table 3.2 shows the base values for the VSD emulator. These values were based on a commercial medium voltage motor and the corresponding values for a VSD rated for a motor of that size.

3.2.1 VSI Average Model

The back end of a VSD is connected to the induction motor load and can be modeled by a VSI. The average model for a VSI is shown in Fig. 2.9.

If s_n is defined as boolean and $s_n = 1$ indicates the high-side switch for phase n is ON, the phase currents and voltages can be related to v_{dc} and i_{dc}. Using s_n, $\overrightarrow{v_v}$ can be reduced to:

$$\overrightarrow{v_v} = v_{dc}\overrightarrow{s_{abc}} - \overrightarrow{v_n} \tag{3.1}$$

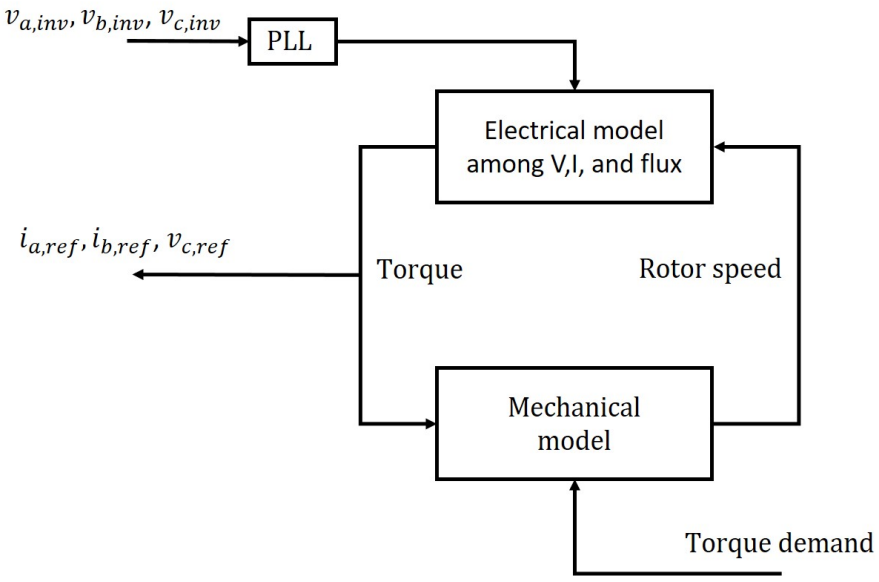


Figure 3.4: Induction motor load model structure.

Table 3.2: Base values for VSD emulation.

Variable	Emulation Value
$V_{dc,ref}$	9 kV
P_{base}	3 MW
$V_{LL,base}$	4.16 kV
C_{dc}	6.4 mF
f_{sw}	5 kHz

where

$$\overrightarrow{v_n} = \frac{v_{dc}}{3}\begin{bmatrix}1 & 1 & 1\\ 1 & 1 & 1\\ 1 & 1 & 1\end{bmatrix}\overrightarrow{s_{abc}} \tag{3.2}$$

which combines into:

$$\overrightarrow{v_{(abc)}} = \frac{v_{dc}}{3}\begin{bmatrix}2 & -1 & -1\\ -1 & 2 & -1\\ -1 & -1 & 2\end{bmatrix}\overrightarrow{s_{(abc)}} - L_f\frac{\overrightarrow{di_{(abc)}}}{dt} \tag{3.3}$$

Thus, the switching model can be defined as:

$$\begin{cases}\overrightarrow{v_{(abc)}} = \dfrac{v_{dc}}{3}\begin{bmatrix}2 & -1 & -1\\ -1 & 2 & -1\\ -1 & -1 & 2\end{bmatrix}\overrightarrow{s_{(abc)}} - L_f\dfrac{\overrightarrow{di_{(abc)}}}{dt} & (3.4)\\ i_{dc2} = \overrightarrow{s_{(abc)}}^T \cdot \overrightarrow{i_{(abc)}} & (3.5)\end{cases}$$

The average of $\overrightarrow{s_{(abc)}}$ is the switching duty cycle, meaning the average model equations can be expressed by:

$$\begin{cases} \overrightarrow{v_{(abc)}} = \dfrac{\overline{v_{dc}}}{3} \begin{bmatrix} 2 & -1 & -1 \\ -1 & 2 & -1 \\ -1 & -1 & 2 \end{bmatrix} \overrightarrow{d_{(abc)}} - L_f \dfrac{\overrightarrow{di_{(abc)}}}{dt} & (3.6) \\ \overline{i_{dc2}} = \overrightarrow{d_{(abc)}}^T \cdot \overrightarrow{i_{(abc)}} & (3.7) \end{cases}$$

The average model for the VSI is shown in Fig. 2.9 in *abc* coordinates and Fig. 2.10 in *dq* coordinates.

3.2.2 HTB connected Rectifier Average Model

The rectifier is used for the front-end of the VSD emulation. HTB load emulators are used as current sources in the system. The physical rectifier on the system is included in the emulators, so the references for the modeled rectifier can be fed directly to the physical rectifier. Then, the rectifier is controlled as if it were the motor drive itself, shown in Fig. 3.5.

To begin the derivation of the average model, you must first derive the inductor voltage equations.

$$L_f \frac{\overrightarrow{di_{(abc)}}}{dt} = \overrightarrow{v_{f(abc)}} - \overrightarrow{v_{t(abc)}} \tag{3.8}$$

Then, the equations in Section 3.2.1 can be used to derive the average model for the rectifier. The circuit diagram of the *abc* average model is shown in Fig. 2.7, and the average model in *dq* coordinates is shown in Fig. 2.8. Fig. 3.7 shows the average model of the entire VSD in *dq* coordinates, including the rectifier and VSI. With the average model shown in Fig. 2.8, v_{fd} and v_{fq} are calculated using the line voltage, the inductor voltage, and the cross-coupling term, shown below in (3.9) and (3.10)

$$v_{fd}[x] = v_{td}[x] + L_f \frac{(i_d[x-1] - i_d[x-2])}{T_s} - \omega L_f i_q[x-1] \tag{3.9}$$

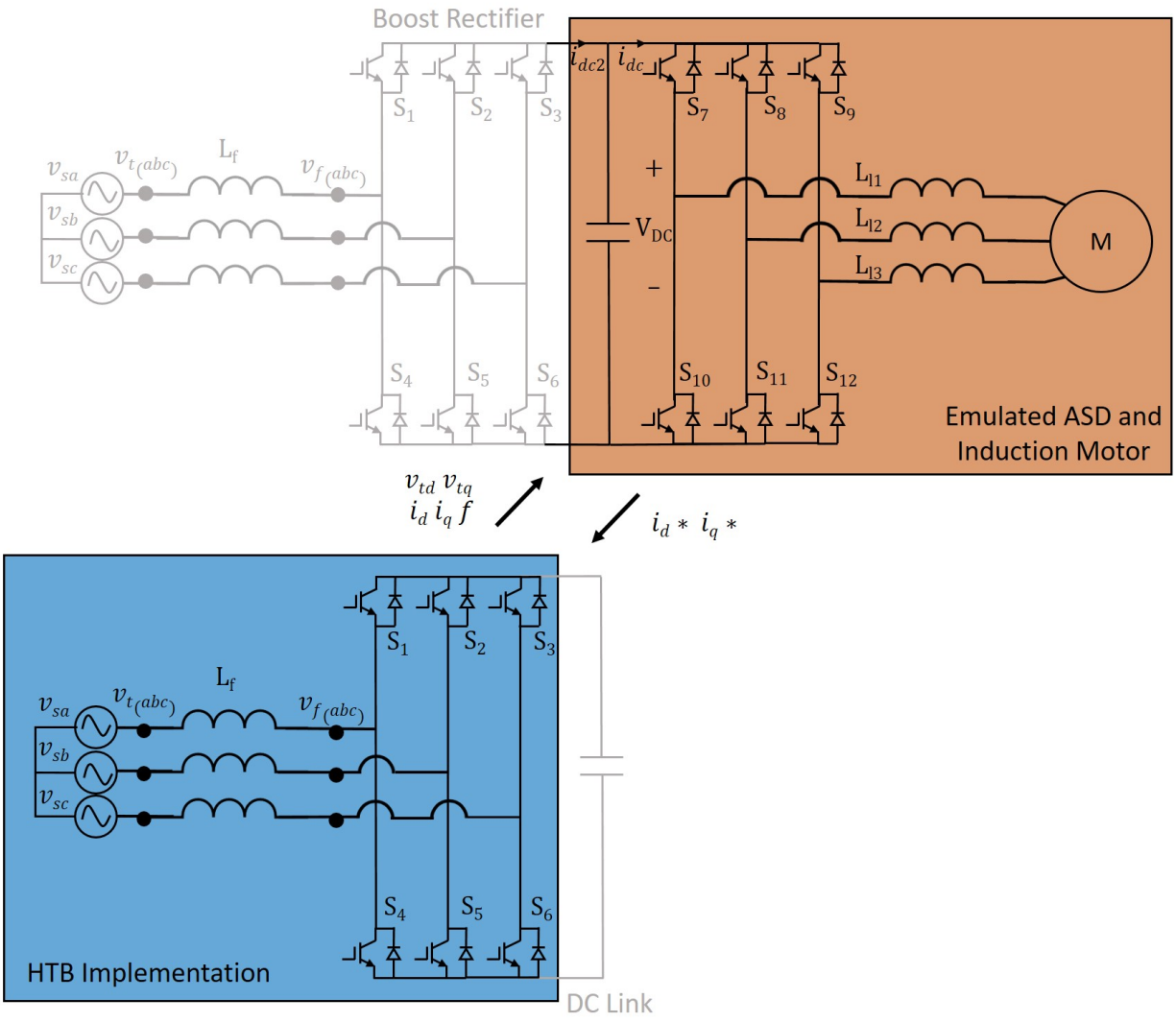


Figure 3.5: Integration of VSD and Induction Motor Emulator and HTB converter.

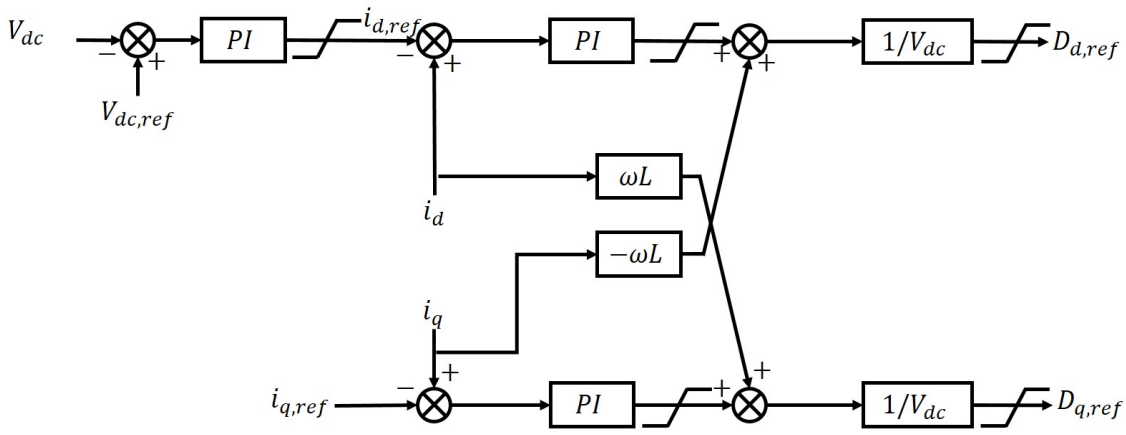


Figure 3.6: DC voltage link control[47].

$$v_{fq}[x] = v_{tq}[x] + L_f \frac{(i_q[x-1] - i_q[x-2])}{T_s} - \omega L_f i_d[x-1] \tag{3.10}$$

This voltage can then be used to calculate the DC current i_{dc2} with the assumption that the power entering the rectifier equals the power leaving it (before the L filter)[52]. Thus, i_{dc2} can be found using the following equations:

$$P_f[x] = 1.5 * (v_{fd}[x-1]i_d[x-1] - v_{fq}[x-1]i_q[x-1]) \tag{3.11}$$

$$i_{dc2}[x] = \frac{P_f[x]}{v_{dc}[x-1]} \tag{3.12}$$

3.3 DC Link Control

For an active front end VSD, the DC voltage control is done in the rectifier. The DC link voltage control isolates the grid voltage from the motor output voltage. This emulator uses a basic PI control, shown in Fig. 3.6. The PI parameters for the DC link voltage control were designed using Matlab/Simulink. The average model, shown in Fig. 3.7, was used to simulate VSD.

3.4 Motor Constant V/f Control

V/f control is used to change voltage at the terminal of the induction motor proportionally to the change of motor reference speed [48], i.e.

$$V_{dinv,ref} = \frac{V_{nom}}{f_{nom}} * f_{ref} \tag{3.13}$$

where $V_{dinv,ref}$ is the output reference voltage for the inverter and f_{ref} is the desired frequency of the motor.

The value of V_{nom} and f_{nom} are set to 1 pu, because all emulator controls are done in per unit values. Therefore, in the per unit system the control is simplified to:

$$V_{dinv,ref} = f_{ref} \tag{3.14}$$

3.5 Grid Frequency Regulation

The grid frequency is measured and compared to the nominal value, which in a per unit system is 1 pu. For this emulator, a detection of a frequency event triggers a different response if used in a microgrid versus the WECC system.

3.5.1 Grid Frequency Regulation for a Microgrid System

Frequency regulation for a microgrid system uses a PI control to determine the value of f_{ref}, shown in Fig. 3.8. The motor frequency reference is limited to 50 % to 1.03 % of the nominal operating speed, which was chosen to limit the effect of the load. The response is triggered when the measured error of the grid frequency goes outside the dead-band of ±60 mHz. This deadband prevents the frequency regulation from triggering for smaller frequency events. The grid frequency regulation can run for a maximum of 30 seconds, after which the speed ramps back to the nominal value at a rate of 5 %/second. Generally, primary frequency control begins to ramp down after 30s, and secondary control takes precedence.

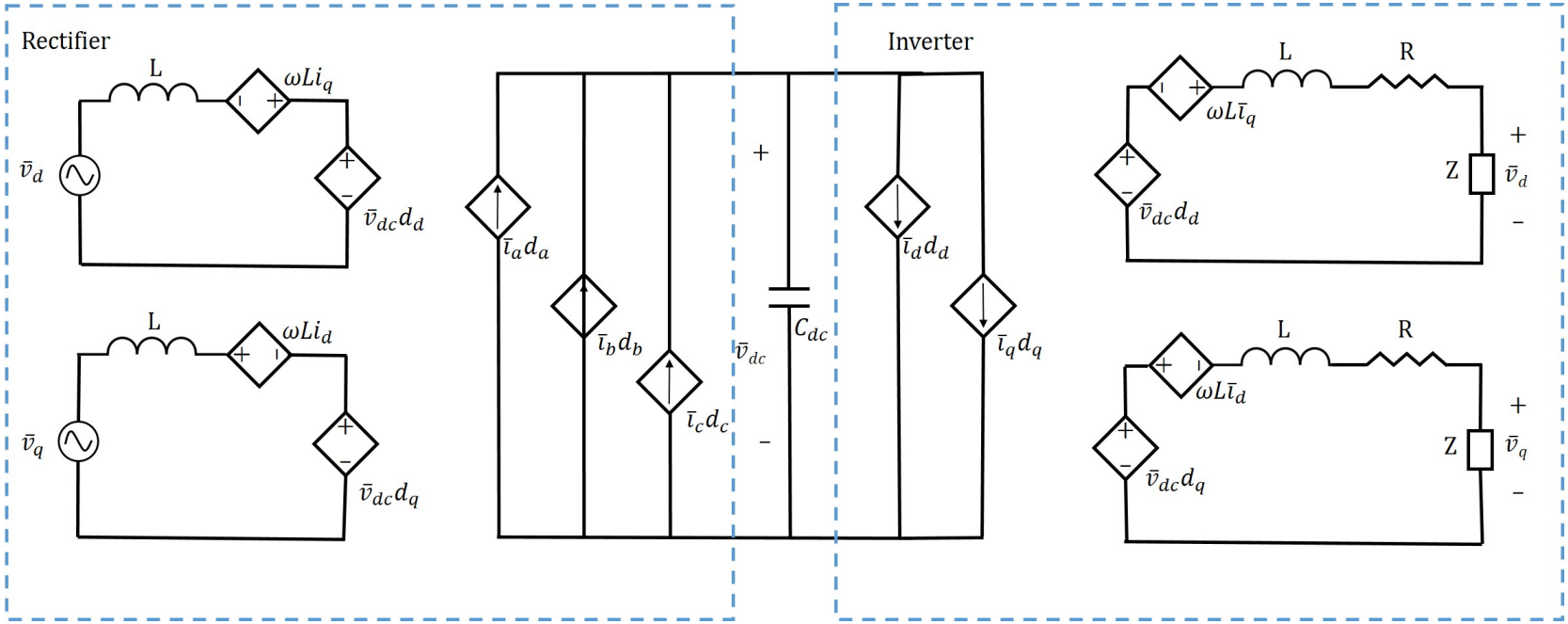


Figure 3.7: Average model of VSD in dq coordinates[45].

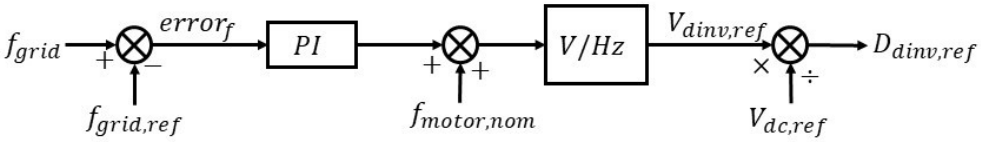


Figure 3.8: Frequency regulation control for microgrid.

3.5.2 Grid Frequency Regulation for an Aggregate Western Electricity Coordinating Council System

The frequency regulation for the WECC system simply reduces or increases the load based on the value of the grid frequency error. Similar to the microgrid case, the motor frequency referenced is limited to 50 % to 1.03 % of the nominal operating speed, and response is triggered when the measured error of the grid frequency goes outside the dead-band of ±60 mHz. The grid frequency regulation can run for a maximum of 30 seconds, after which the speed ramps back to the nominal value at a rate of 3 %/second. Fig. 3.9 shows the response for the case when grid frequency goes below the dead-band limits.

3.6 Simulation

3.6.1 Emulation Model Verification

Matlab/Simulink is used to verify the AF-VSD model and induction motor. The simulation is set up like Fig. 3.1 with a voltage source connected to the AF-VSD. The reference motor frequency for the V/f control is changed using the ramp function discussed in Section 3.5.2. Fig. 3.10-3.12 compares the motor reference frequency for V/f control, power absorbed by the VSD, and actual motor rotational speed with varying inertia constants of $H = 0.1$, $H = 0.6$, and $H = 0.8$, respectively. Since the induction motor model and VSD are based on

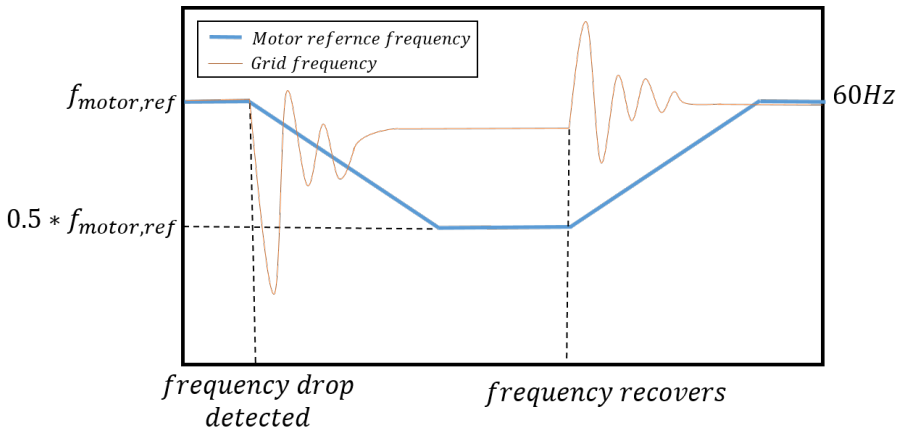


Figure 3.9: Frequency regulation control for WECC.

previously implemented emulators, the main purpose of verification is to observe the response of the load power when the frequency regulation control is implemented. Fig. 3.10 shows that with a low inertia constant, H, the power absorbed by the the VSD is proportional to the motor speed. However, when $H = 0.8$, which is shown in Fig. 3.12 shows a variance in the power from the interaction of the inertia.

3.7 Chapter Summary

The emulated VSD includes an induction motor model and active front end VSD. The power electronics are modeled using average models, and all passive components are modeled using their relevant voltage and current equations. The controls include DC link voltage, inner and outer current loop, and grid frequency regulation. The model was verified using Matlab/Simulink.

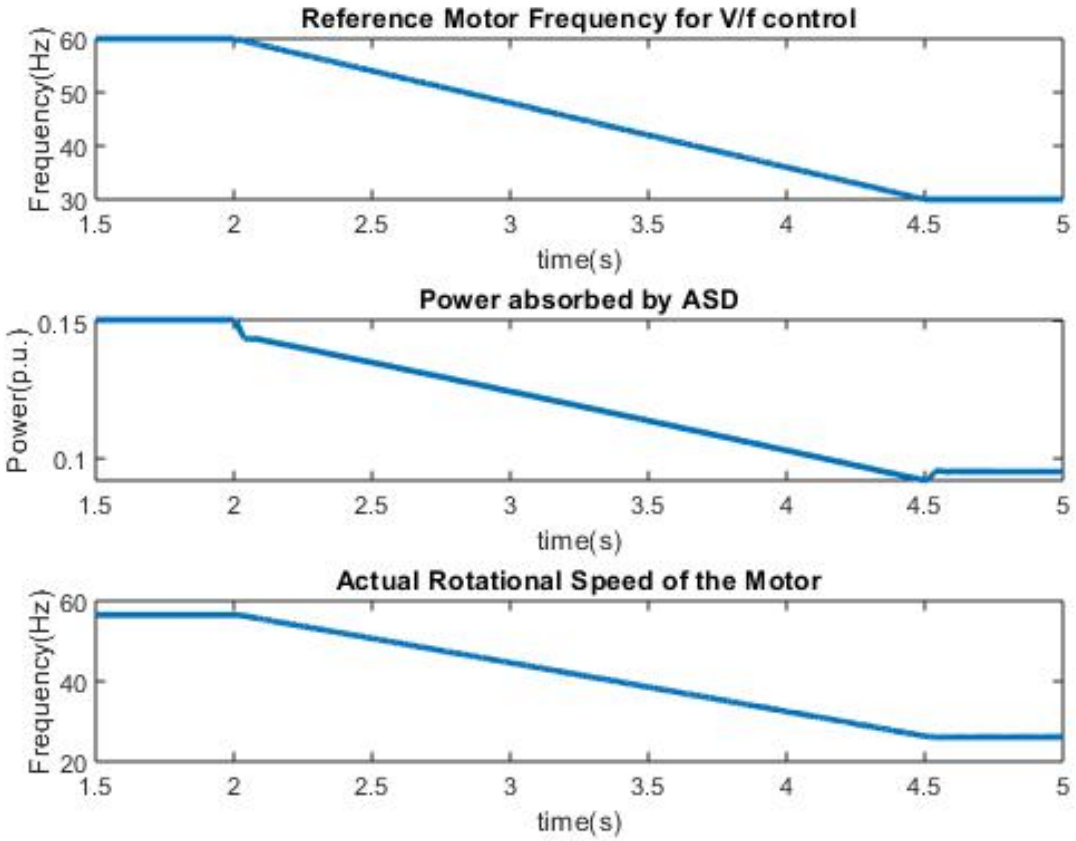


Figure 3.10: Simulink verification of VSD model when H=0.1.

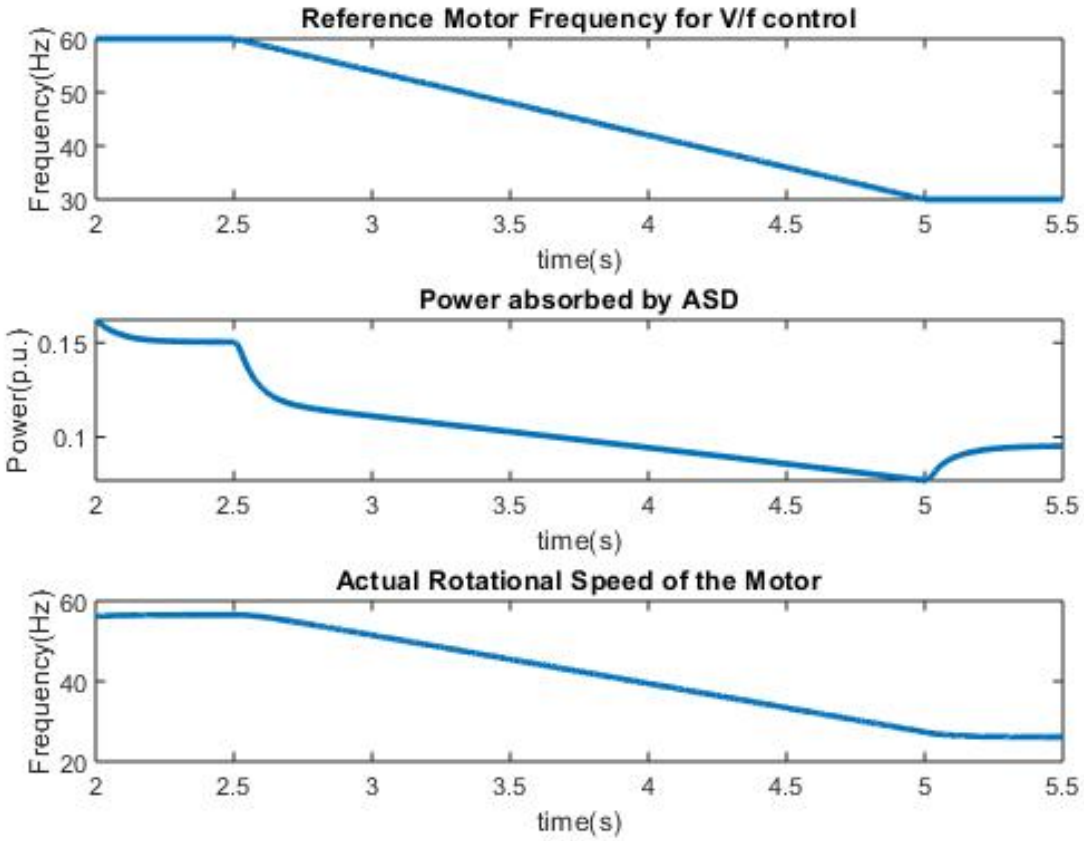


Figure 3.11: Simulink verification of VSD model when H=0.6.

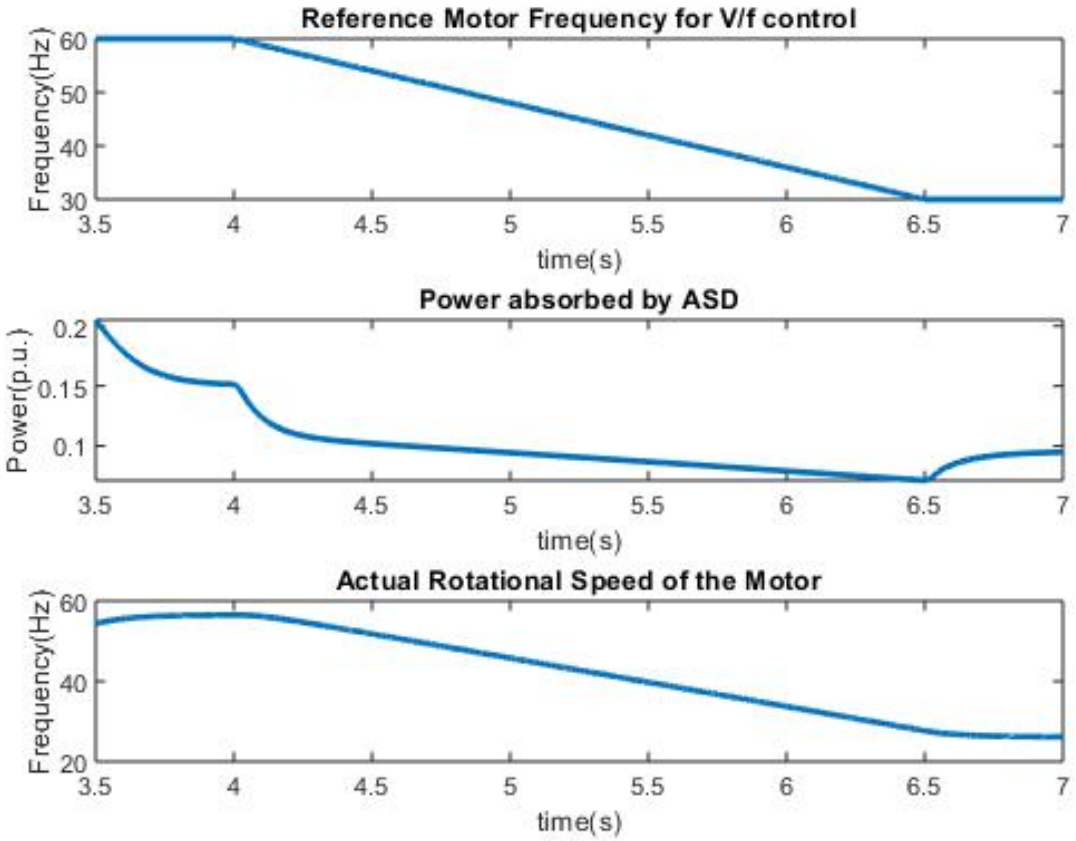


Figure 3.12: Simulink verification of VSD model when H=0.8.

Chapter 4

Experimental Results and Discussion

The system outlined in Chapter 3 is emulated with a two bus system on both the microgrid and WECC platforms on the HTB. The system responses are verified by simulation system in PSCAD/EMTDC.

4.1 HTB Experimental Set Up

To verify the behavior of the VSD and the frequency regulation, it was tested in a single area cabinet with the configuration shown in Fig. 4.1. A photo of the physical hardware is shown in Fig. 4.2. This set up is used to test both the WECC and microgrid system. The following sections explain additional system parameters.

4.2 Microgrid System

4.2.1 HTB Model Verification

In order to verify the HTB model and the PSCAD/EMTDC model, the model was implemented on both platforms with the same parameters. Table 3.1 shows the parameters for the induction motor, and Table 3.2 shows the parameters for the VSD. For this case, the model has a low inertia constant, $H = 0.1$, because it allows the dynamics of the V/f control to be easily observed at the output power, which helps troubleshooting on the HTB platform.

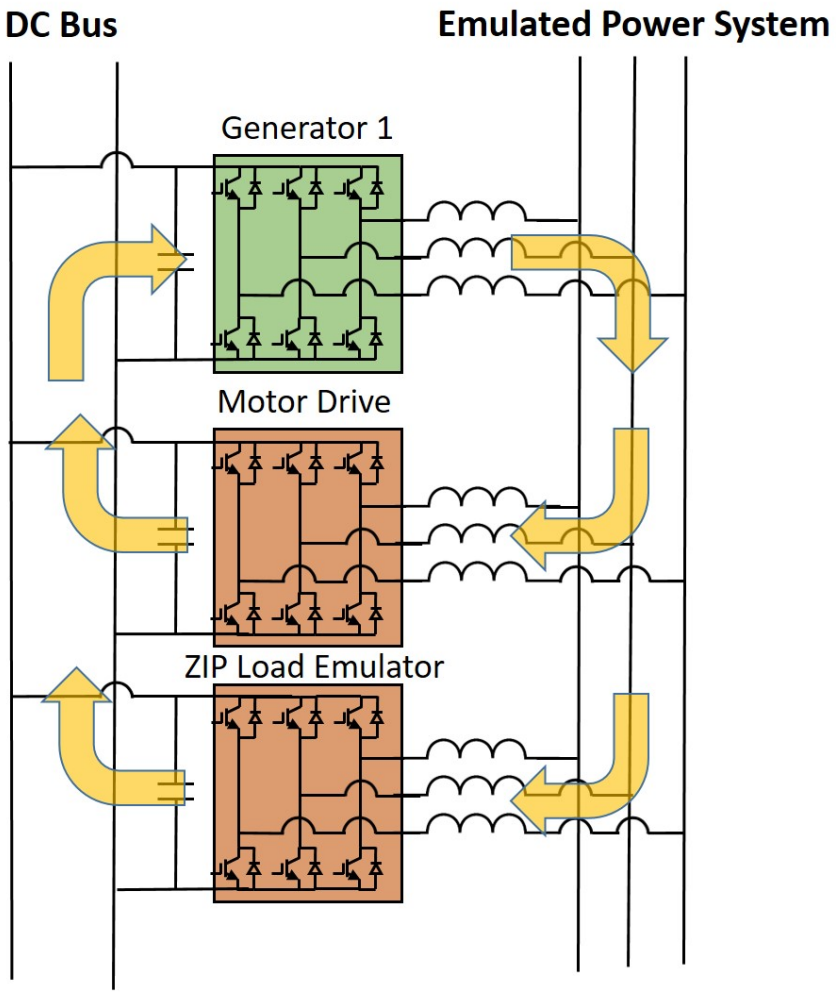


Figure 4.1: Emulated system for VSD model verification.

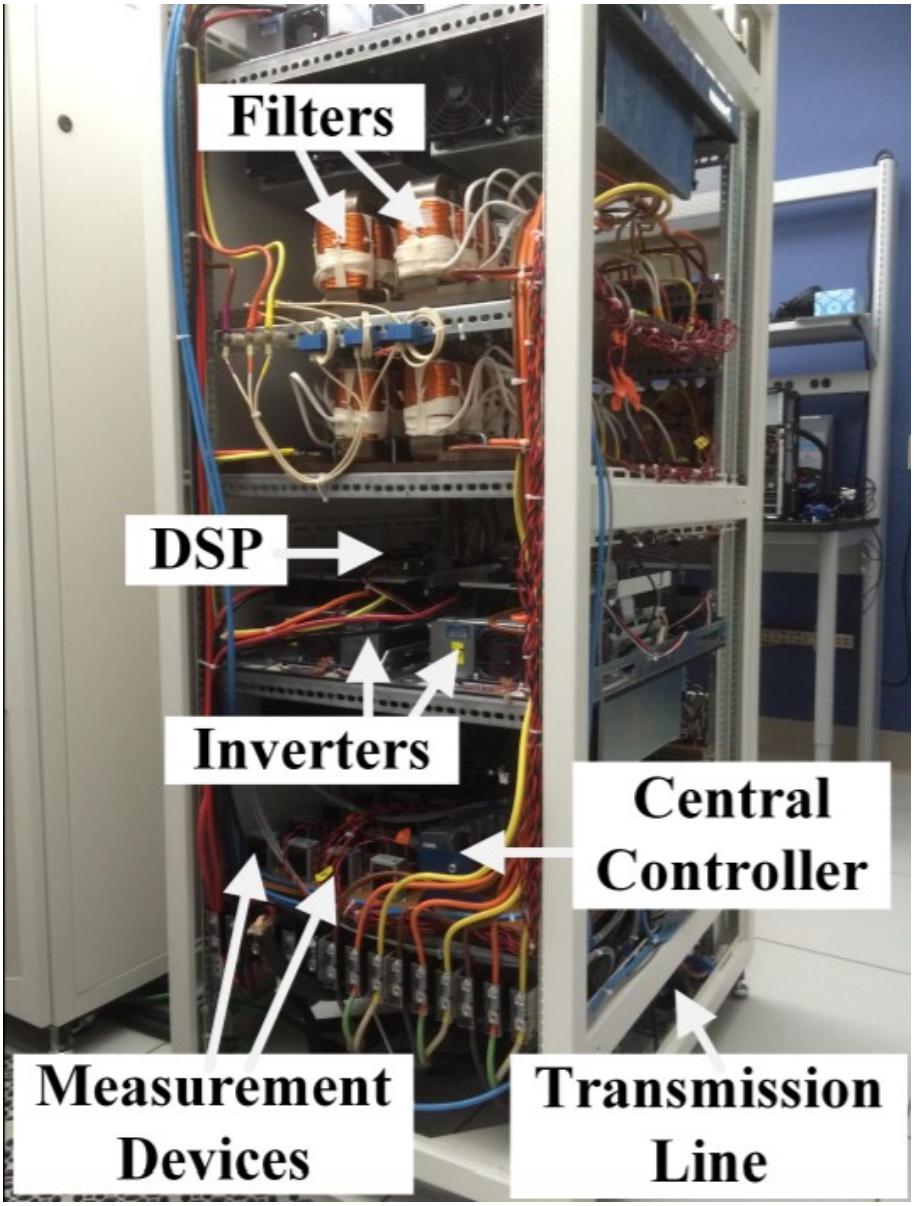


Figure 4.2: Experimental setup for HTB platform testing.

Table 4.1: Microgrid System and HTB Power and Voltage Bases

Base	Microgrid	HTB
Power	0.1 MVA	1 kVA
Voltage	0.574 kV	81.65 V

When the model is implemented on the HTB platform, all models must be converted to the HTB bases before being sent to the inner current loop control of the HTB's VSIs. Table 4.1 shows the default power system scale for the microgrid system and the HTB's power and voltage bases.

Fig. 4.3 shows the grid frequency response for the model on the HTB platform and in PSCAD/EMTDC. This is implemented in the two bus system shown in Fig. 4.1. Varying ZIP loads are applied to the load bus. The VSD is absorbing 0.1 p.u. A ZIP load is added that absorbs 0.1 p.u., 0.05 p.u., and 0.04 p.u. The frequency control on the HTB model uses the local frequency determined by the PLL measurement at the point of the load. However, in the model in PSCAD/EMTDC, the frequency control uses the nearest generator frequency. This explains the dynamic discrepancies between the two responses. Additionally, the response for the HTB shown in Fig. 4.3 is the moving average of the waveform. This helps visualize the response without the measurement noise. There is additional oscillation in the steady state response of the 50% and 40 % ZIP load increase because the HTB platform has greater stability at higher powers.

4.2.2 Microgrid System Results

The microgrid system is shown in Fig. 4.4. There is one synchronous generator at Bus 8, and one VSD located at Buses 2, 5, and 8. The remaining loads are represented as ZIP loads. The frequency control in the VSD uses the frequency from the generator. Given the

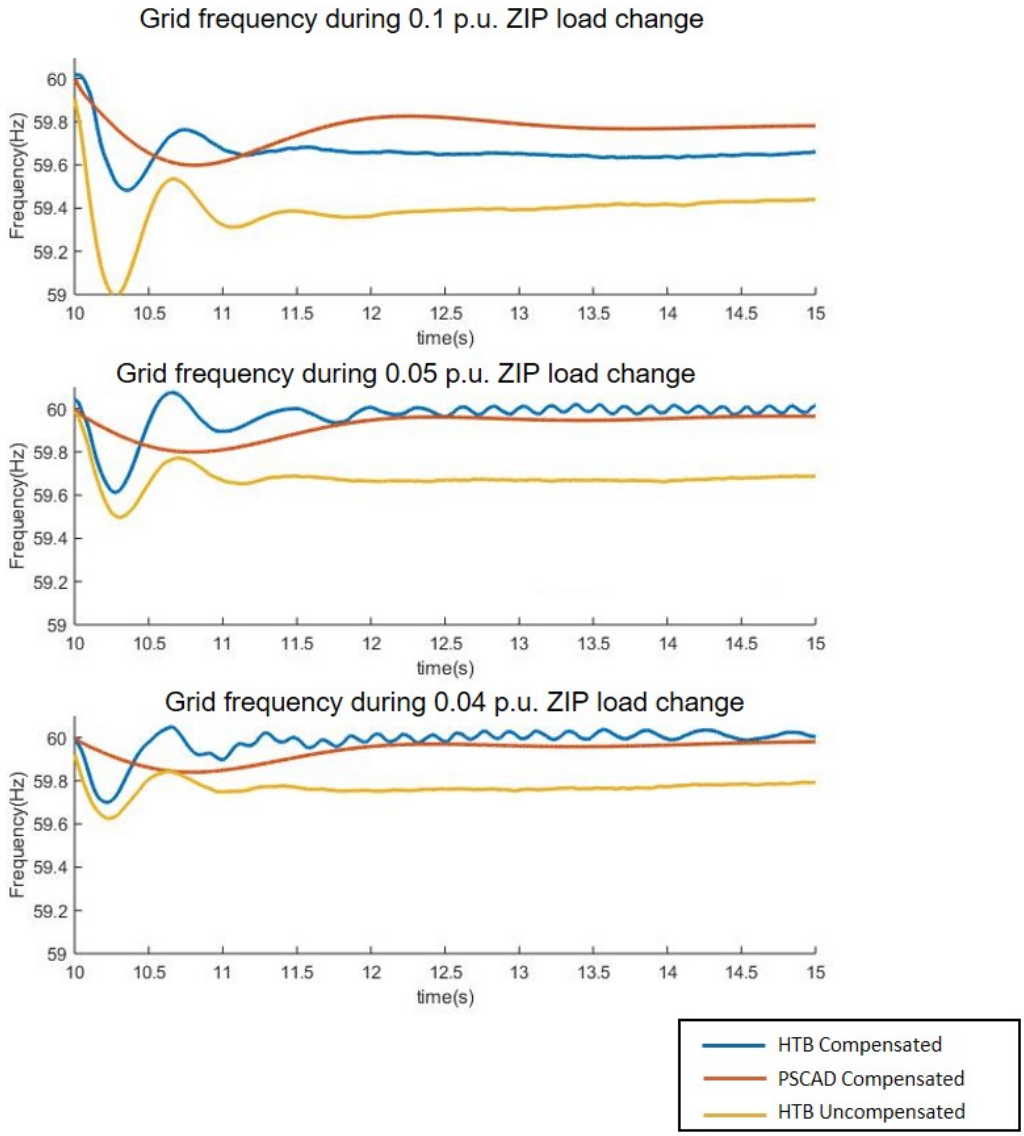


Figure 4.3: VSD model response for a microgrid on HTB platform and in PSCAD.

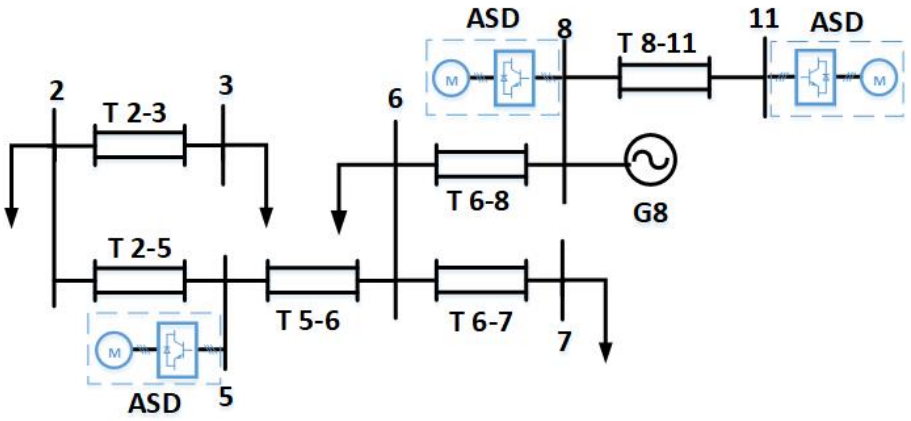


Figure 4.4: One-line diagram of the microgrid system.

size of the microgrid, the generator frequency can be an approximation of the frequency at each bus. The frequency control implemented is the control shown in Fig. 3.8. The inertia constant for the induction motor is $H = 1$, which is the commonly accepted value for motors with a rating greater than 200 hp.

Fig. 4.5 shows the frequency response for varying penetration of VSDs on the microgrid. For the no VSD case, the motor load at Buses 5, 8, and 11 are directly connected to the grid without an VSD interface. For the 1 VSD case, the motor load at Bus 8 has an VSD connected induction motor. For 2 VSDs, Buses 8 and 11 have an VSD-connected induction motor. Finally, the 3 VSD case has an VSD interface at each motor load at Buses 5, 8, and 11. In order to cause a frequency event, a 0.1 p.u. load increase in added at Bus 6 at 10 seconds. The load recovers to its original value at 30 seconds. Automatic generation control is active in the generator. This control responds 4 seconds after the event. This explains the asymmetry between the initial load event at 10 seconds and the recovery at 30 seconds. After the automatic generation control begins to respond, the loads and the generator are both providing frequency support. However, during the first 4 seconds of the event, before the automatic generation control responds, the load is solely providing the compensation for the frequency fluctuation.

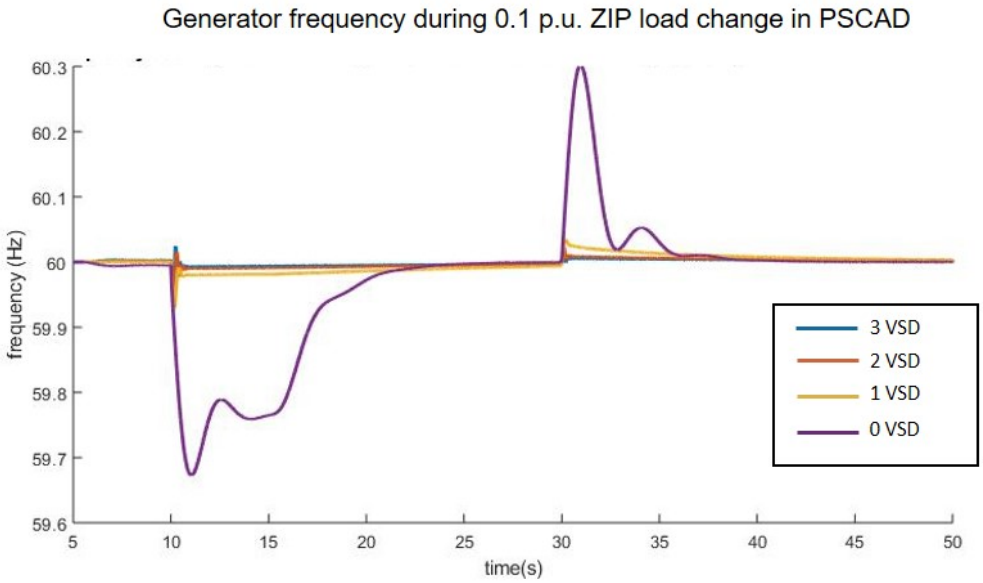


Figure 4.5: Frequency during 0.1 p.u. load increase for varying penetration of VSD.

Fig. 4.6 shows the induction motor stator voltage, current, and VSD power when all three VSDs are on the grid and are actively compensating frequency. When the ZIP load increases at Bus 6 at 10 seconds, the frequency drops. When the frequency reaches the lower deadband, 59.94 Hz, the VSD frequency regulation is activated. The frequency regulation decreases the induction motor stator voltage. This causes an immediate decrease in the current because of the motor inertia. As the voltage continues to decrease, the inertia causes the motor current to increase. When the load recovers to its original value at 30 seconds, the voltage gradually increases to its original value.

Figs. 4.7 and 4.8 show the response when there is a 0.1 p.u. load increase at Bus 6, and there is only one VSD on the grid, at Bus 8. The top figure in Fig. 4.7 shows the frequency response of the grid when the VSD is actively compensating the frequency versus when there is no frequency regulation active at the VSD, and the bottom figure shows the voltage at the induction motor stator voltage and the power of the VSD. Figs. 4.9 and 4.10 show the response when there is a 0.1 p.u. load increase at Bus 6, and there are only two VSDs on

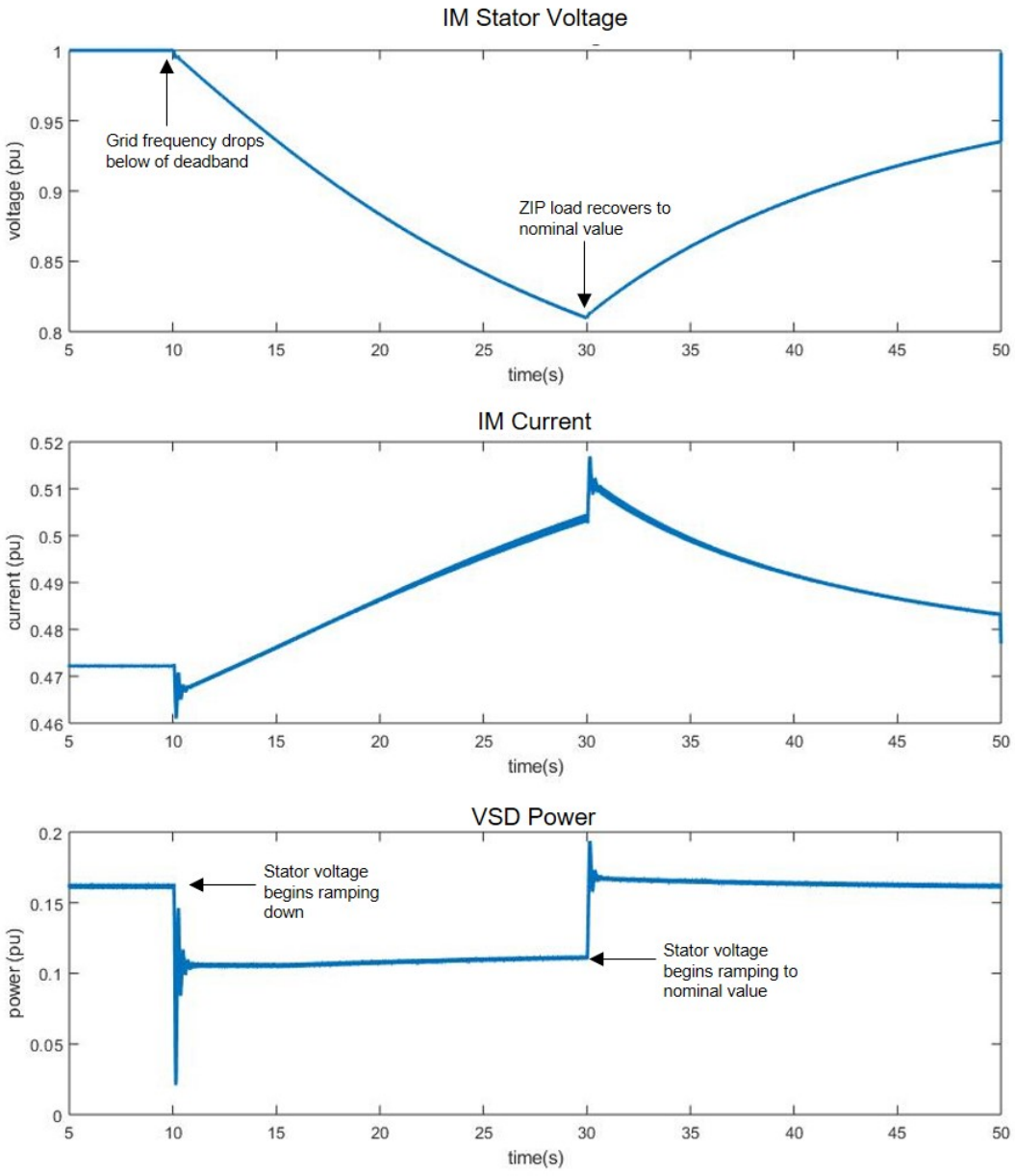


Figure 4.6: VSD power and induction motor stator voltage and current during 0.1 p.u. ZIP load increase.

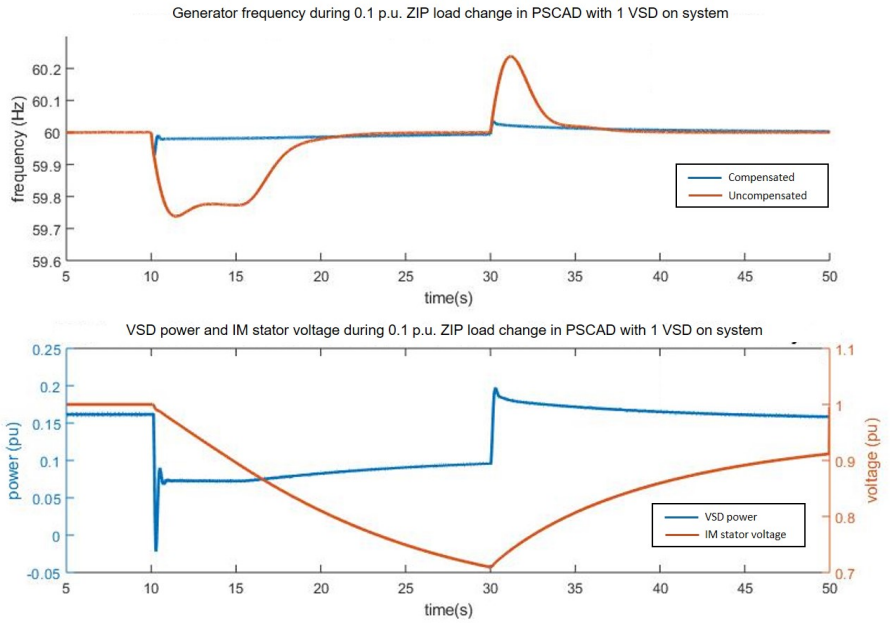


Figure 4.7: The top figure shows the frequency during 0.1 p.u. load increase with 1 VSD on system comparing frequency regulation and without frequency regulation. The bottom figure shows induction motor stator voltage and VSD power.

the grid, at Bus 8 and 11. Fig. 4.11 and 4.12 show the response when there is a 0.1 p.u. load increase at Bus 6, and all three VSDs are on the grid, at Buses 5, 8 and 11.

Figs. 4.8, 4.10, and 4.12 show the generator frequency and the induction motor stator voltage for a 0.1 p.u. ZIP increase for 1 VSD, 2 VSD, and 3 VSD respectively. These figures show the frequency regulation is activated at the bottom of the frequency deadband, at 59.94 Hz in each case. Comparing the three cases, shown in Figs. 4.7, 4.9, and 4.11, less compensation is required from each VSD, when all three VSDs are actively compensating the frequency. There is only a 10 % drop of the induction motor stator voltage, which cooresponds to a 10 % drop in motor speed. However, even with the case of one VSD on the grid, the induction motor stator voltage is only decreased to 70% of the nominal value.

Fig. 4.13 shows the dynamics of the frequency within the first second after the event, which varies for each different case. This can be explained by the oscillation in the frequency

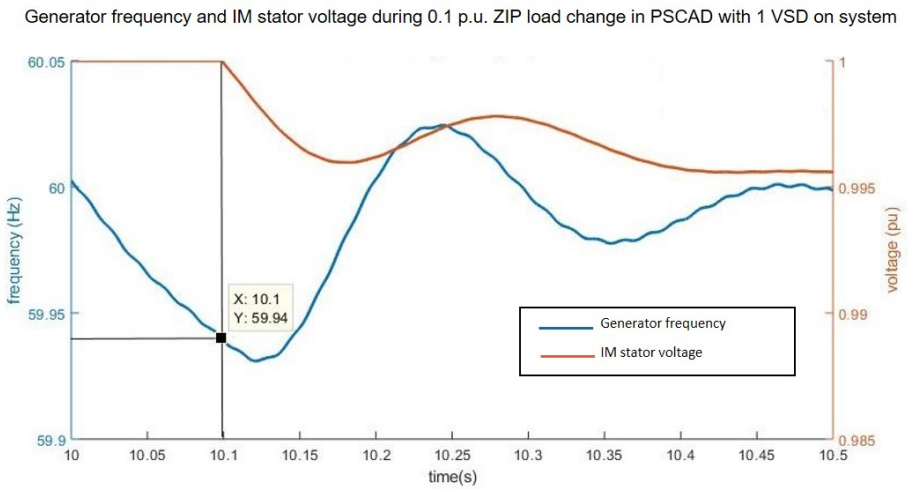


Figure 4.8: Grid frequency and induction motor stator voltage during 0.1 p.u. load increase with 1 VSD on system.

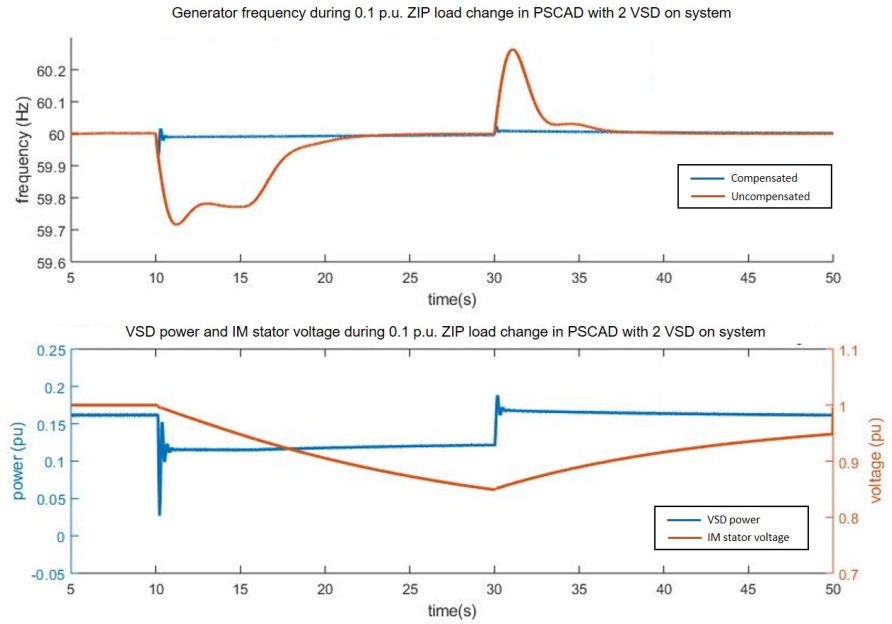


Figure 4.9: The top figure shows the frequency during 0.1 p.u. load increase with 2 VSD on system comparing frequency regulation and without frequency regulation. The bottom figure shows the induction motor stator voltage and VSD power.

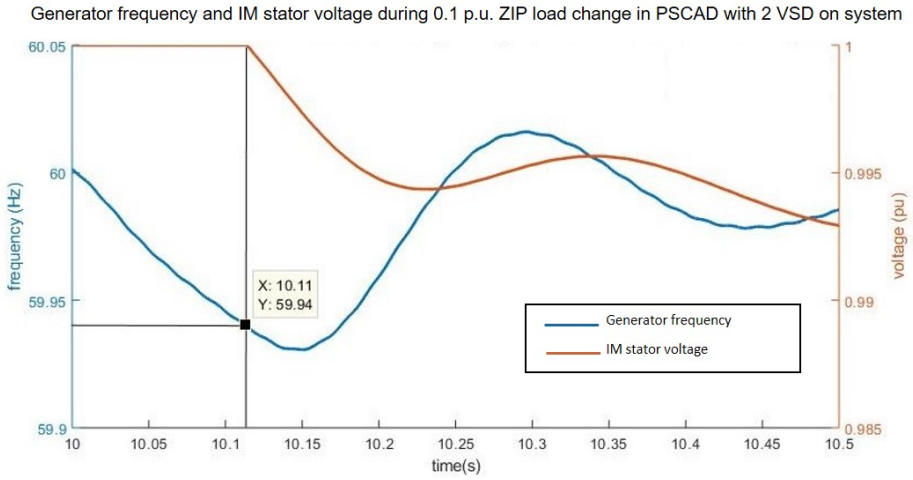


Figure 4.10: Grid frequency and induction motor stator voltage during 0.1 p.u. load increase with 2 VSD on system.

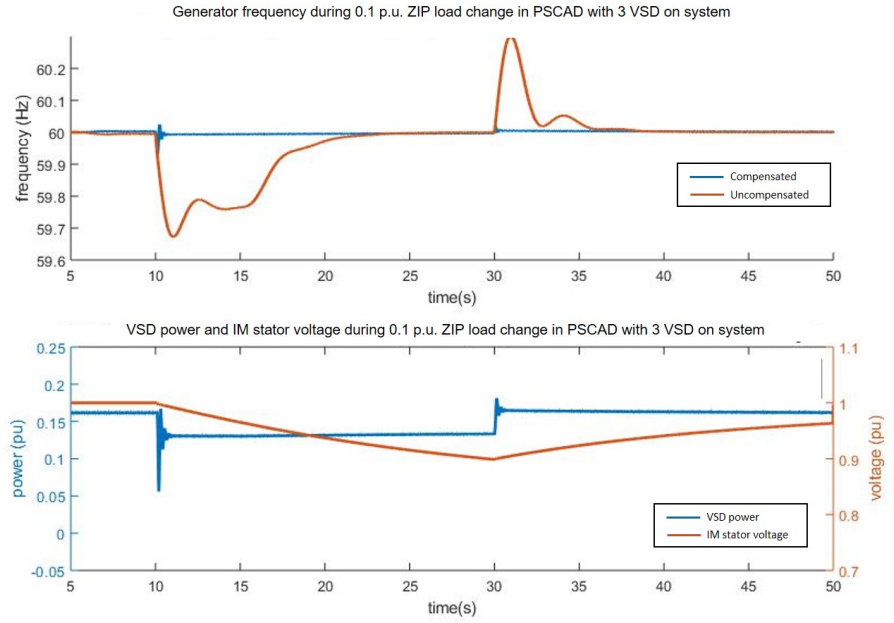


Figure 4.11: The top figure shows the frequency during 0.1 p.u. load increase with 3 VSD on system comparing frequency regulation and without frequency regulation. The bottom figure shows the induction motor stator voltage and VSD power.

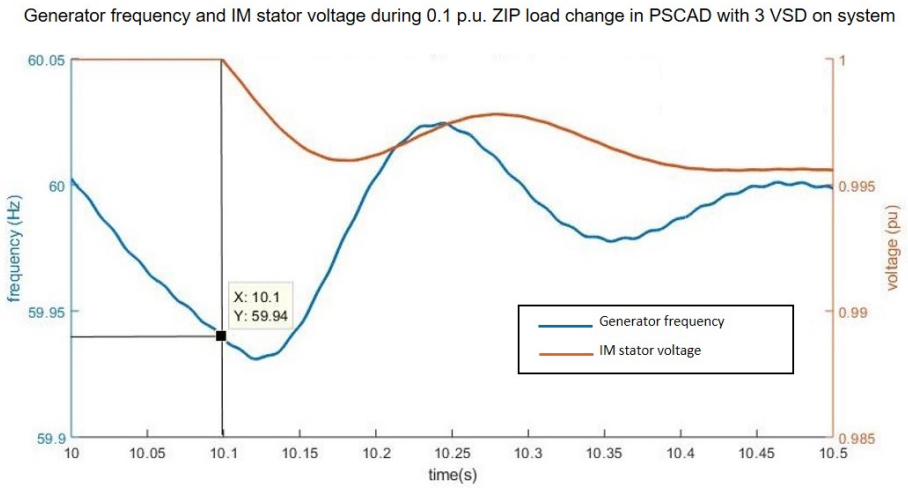


Figure 4.12: Grid frequency and induction motor stator voltage during 0.1 p.u. load increase with 3 VSD on system.

regulation control, which can be seen in Figs. 4.8, 4.10, and 4.12. The oscillation in the stator voltage causes an oscillation in the frequency response of the grid. This could be mitigated with a more finely tuned PI control in the frequency regulation.

4.3 WECC System

4.3.1 HTB Model Verification

In addition to the model verification done in Matlab/Simulink, the VSD model was verified by comparing the results on the HTB platform and PSCAD/EMTDC for a two bus system. Fig. 4.14 and Fig. 4.15 compare the results for a ZIP load increase that is equivalent to 50% and 60% of the VSD load at nominal speed. The inertia constant, H, for these tests are low, i.e. $H = 0.1$. Similar to the microgrid system, the low inertia allows the dynamics of the V/f control to be observed in the VSD power output.

The VSD absorbs 0.1 p.u. A ZIP load is added that absorbs 0.06 p.u. and 0.05 p.u., shown in Fig. 4.14 and 4.15. For the frequency on the HTB platform, the frequency is

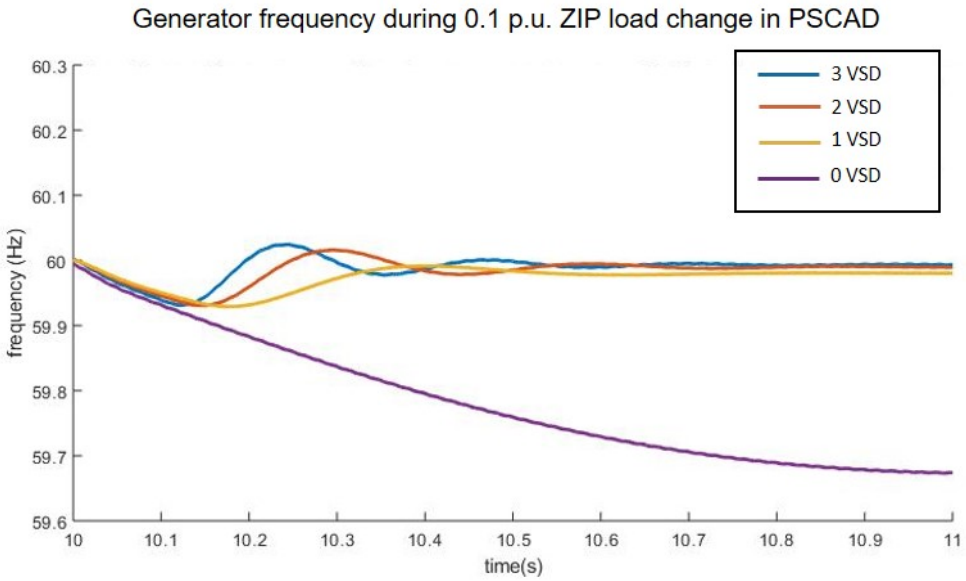


Figure 4.13: Frequency during first second after 0.1 p.u. load increase for varying penetration of VSD.

measured through a PLL at the point of the load. This frequency is used for the control of the VSD frequency response. However, in PSCAD/EMTDC, the frequency used for VSD control is measured at the generator frequency, which is a better representation of the system frequency. However, on the HTB, since each emulation is run on different converters, it is more practical to use the measurements at each converter. This explains the discrepancies between the results from the two platforms. The generator inertia causes overshoot of the minimum frequency in the PSCAD/EMTDC simulation. In both cases, the grid frequency changes at a similar rate and reaches steady state at similar values. When the 0.05 p.u. ZIP load is added, the frequency returns to 60 Hz. However, because the motor is limited to only decreases to 50 % of the nominal speed, when the 0.06 p.u. ZIP load is added, the frequency only returns to 59.95 Hz. The VSD is only capable of compensating for 0.05 p.u. out of the 0.06 p.u. loss on the system.

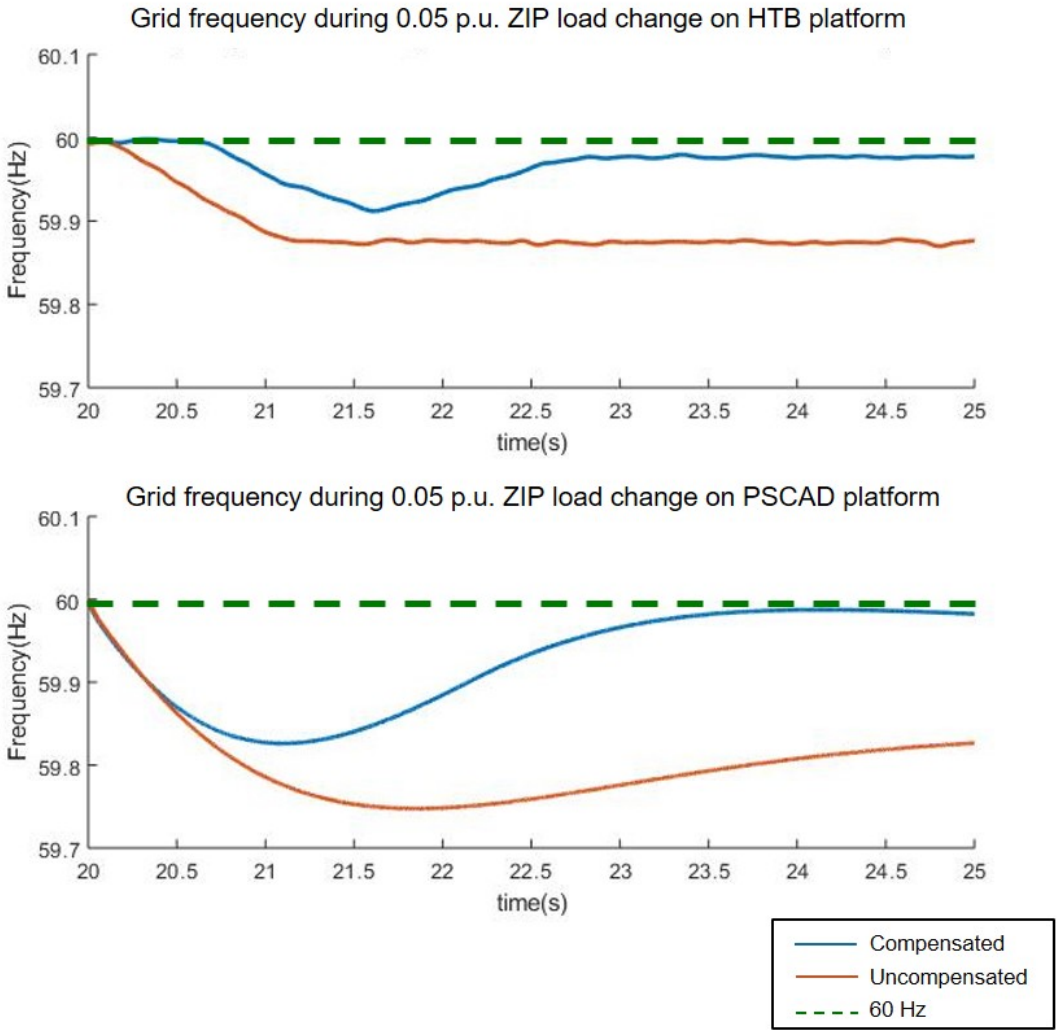


Figure 4.14: VSD model response on HTB platform and in PSCAD with 50% ZIP load increase.

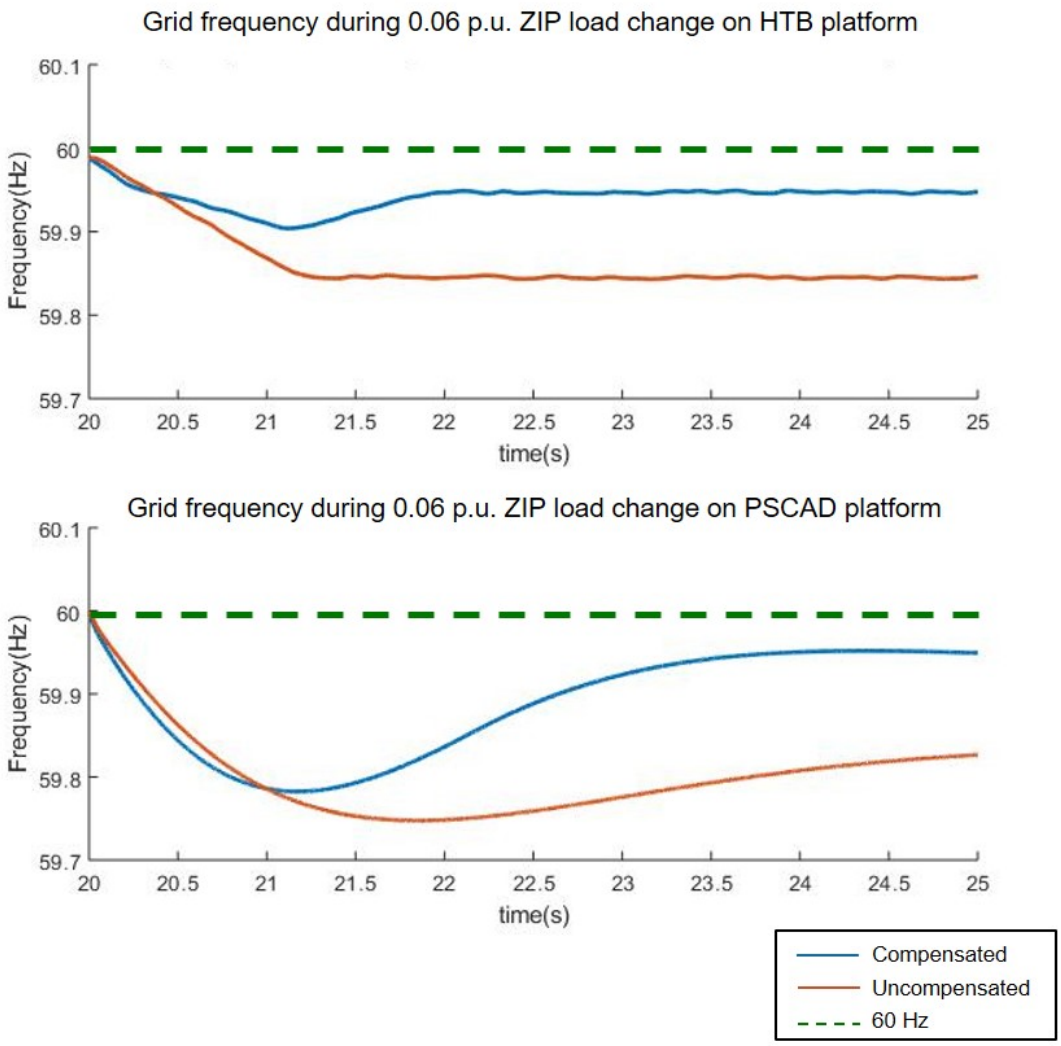


Figure 4.15: VSD model response on HTB platform and in PSCAD with 60% ZIP load increase.

Table 4.2: WECC System and HTB Power and Voltage Bases

Base	WECC	HTB
Power	10 GVA	2 kW
Voltage	500 kV	43.8 kV

4.3.2 WECC System Results

The aggregate WECC system is shown in Fig. 4.16. All the generators are represented by synchronous generators, and there is an VSD at Bus 8,10, and 11. The remaining loads are represented as ZIP loads. The default power system scale for the WECC system and the HTB's power and voltage bases are displayed in Table 4.2. The simulations in PSCAD/EMTDC are done in the WECC power and voltage bases. However, when implemented on the HTB platform, all models must be converted to the HTB bases before being sent to the inner current loop control of the HTB's VSIs.

In this case, high power motor systems represent roughly 10% of the total load. According to the United States Industrial Electric Motor Systems Market Opportunities Assessment preformed in 2002, industrial motor systems above 200 hp make up 44.6 % of the total industrial motor energy consumption. According to this same report, industrial motor systems make up 25 % of the total energy consumption in the United States [4]. Therefore, it can be estimated that industrial motors above 200 hp make up roughly 11 %, so a 10% penetration is a good representation of the large motors driving a fan, pump, or compressor on the system. There are three aggregate VSD models on the system. For simplification, it is assumed that one model with a larger power consumption can represent multiple smaller systems. Due to the fact that frequency is fairly global for a localized part of the grid, then the frequency control can be accurately represented by one system.

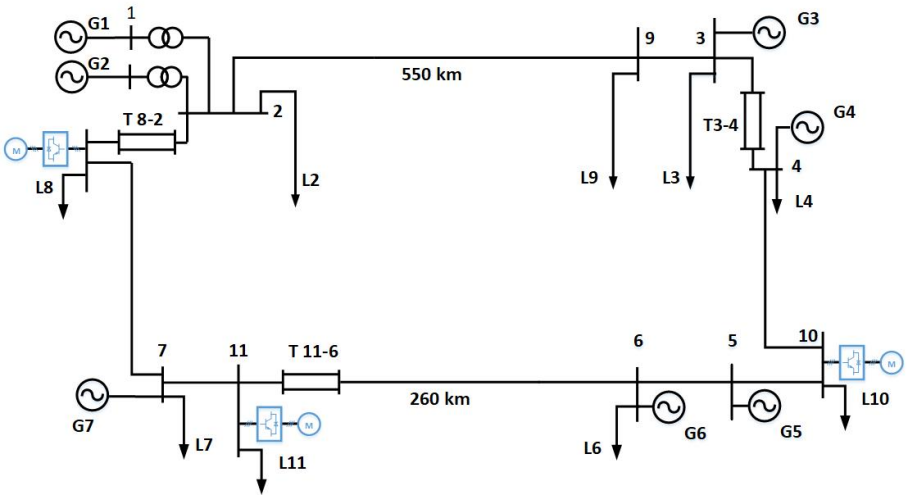


Figure 4.16: One-line diagram of the aggregate WECC system.

Various test cases were simulated in PSCAD/EMTDC. Based on the results shown above, the HTB system response can fairly accurately be estimated through PSCAD/EMTDC. In order to test the response of VSD connected medium voltage induction motors, the value of the inertia constant, H, was set to 1 for these test cases. This is the commonly accepted value for large induction motors above 200 hp. Automatic generation control (AGC) for frequency is also active in generator 4 and generator 6. AGC activates 4 seconds after the initial frequency event and remains active for the rest of the test case.

Fig. 4.17 shows the induction motor stator voltage, induction motor current, and the total power from the VSD. This figure shows that when the stator voltage begins to decrease, the motor current initially decreases, but then increases while the voltage continues to ramp down. However, when the stator voltage stops ramping, the motor current also stabilizes at a constant value. When the ZIP load recovers to its original value at 35 seconds, the stator voltage begins to ramp back to the orginal value. When the stator voltage begins to ramp up, the motor current initially increases, but then decreases until the stator voltage reaches its nominal value.

The frequency response is initiated by adding a ZIP step load that is equal to 10% of the amount of generation at the time of the event. Three cases were tested: a 470 MW ZIP load

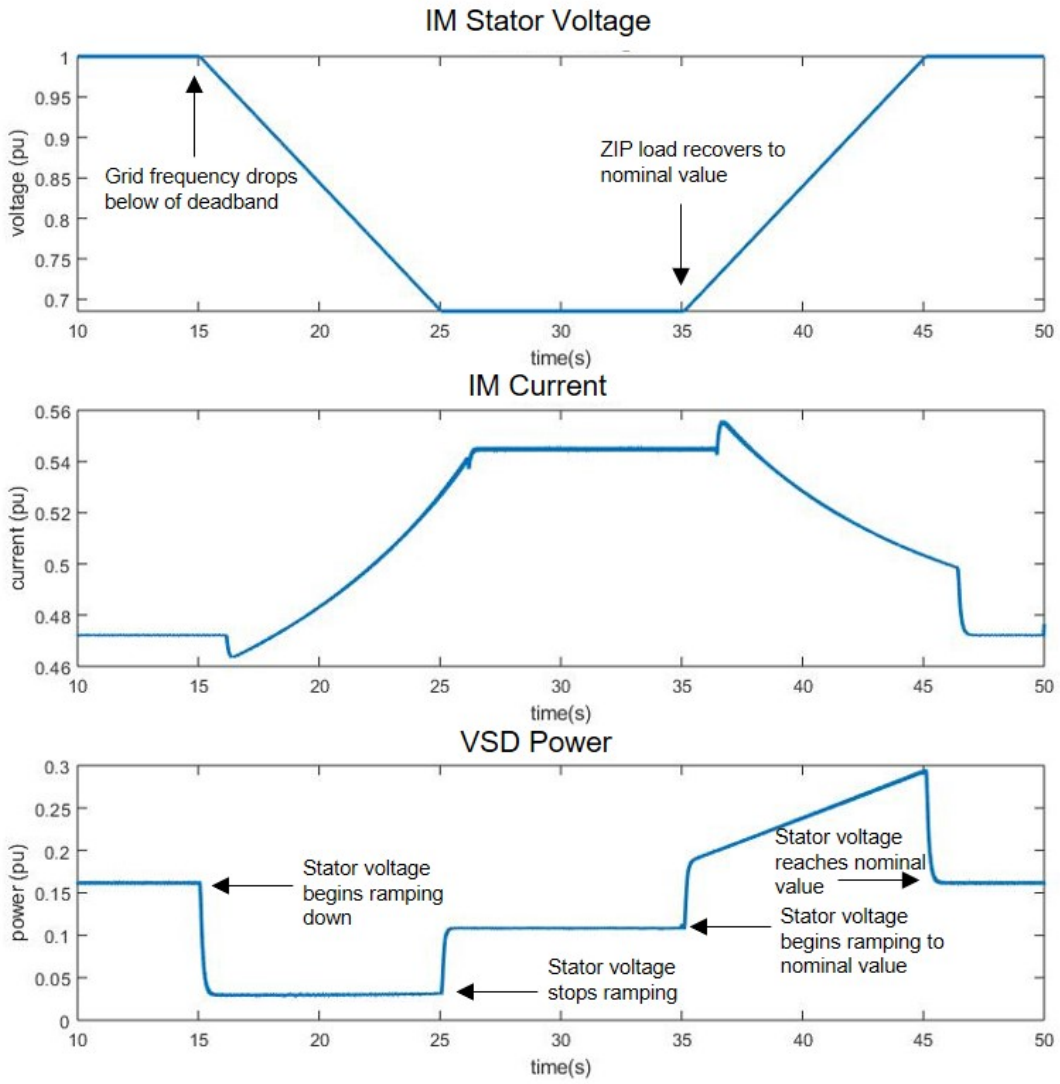


Figure 4.17: VSD power and induction motor stator voltage and current for grid frequency regulation on the WECC system.

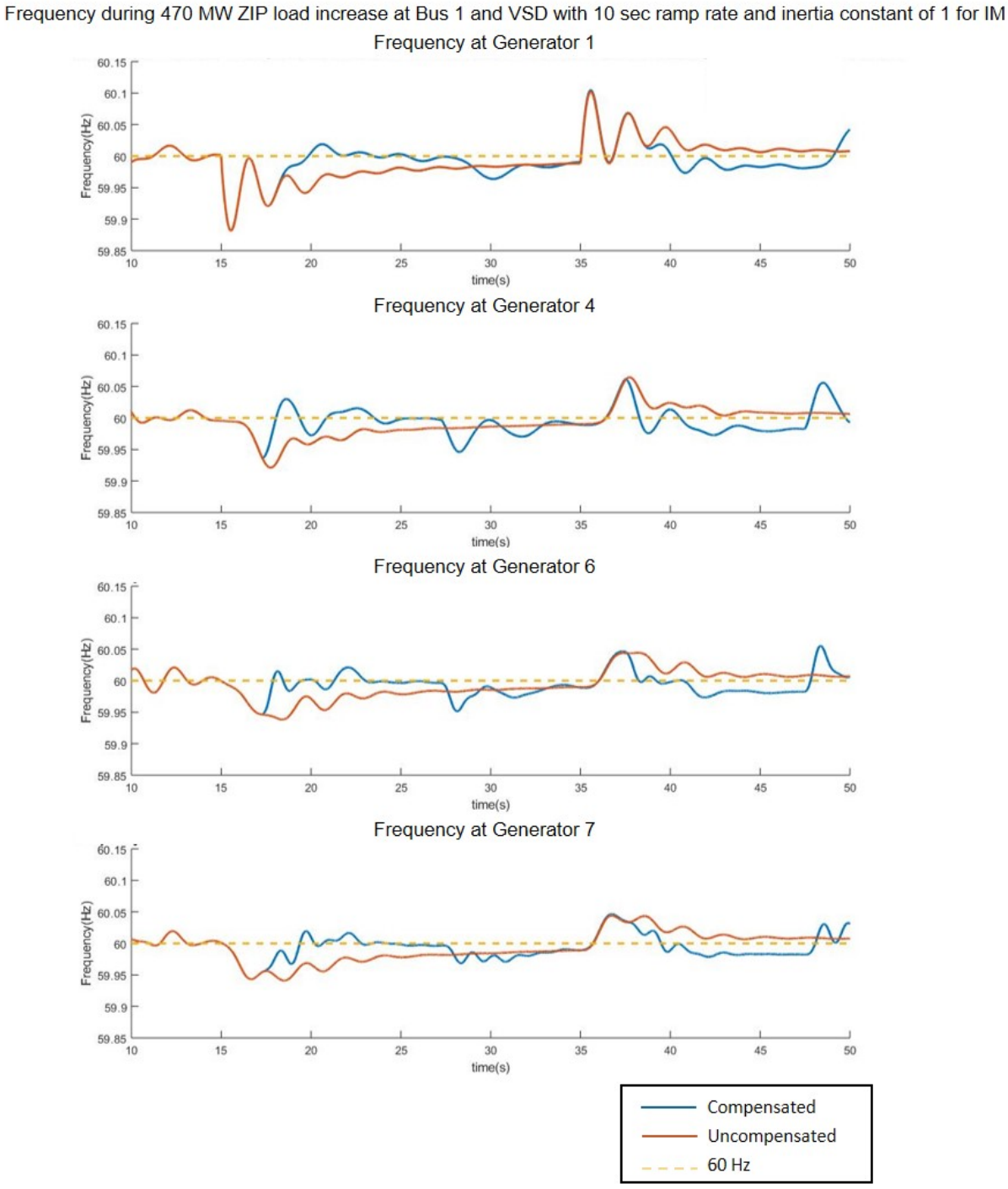


Figure 4.18: Frequency of generators 1, 4, 6, and 7 during 470 MW ZIP load increase at Bus 1 comparing with frequency regulation and without frequency regulation.

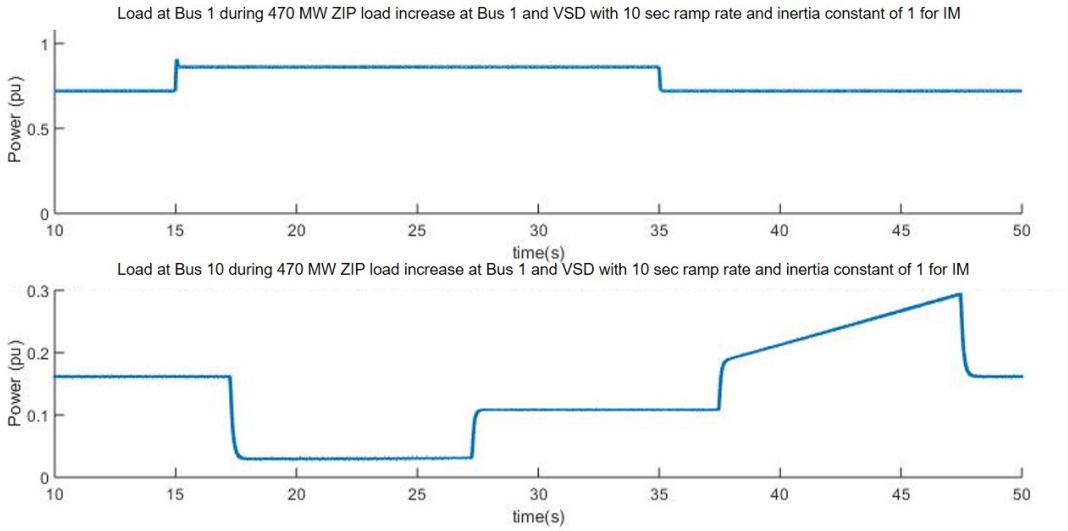


Figure 4.19: Load at Buses 4 and 10 during 470 MW ZIP load increase at Bus 1.

increase at Bus 1, a 485 MW ZIP load increase at Bus 4, and a 477 MW ZIP load increase at Bus 7. Fig. 4.18 shows the frequency at Buses 1, 4, 6, and 7 when the 470 MW ZIP load is added to Bus 1, because these are the buses with generators closest to the load event and the 3 VSDs on the grid. Fig. 4.19 shows the power absorbed by the VSDs at Buses 1 and 10. The frequency at Buses 8 and 11 never went out of the dead-band. Fig. 4.20 shows the frequency when the 485 MW ZIP load is added to Bus 4. Fig. 4.21 is the power absorbed by the VSDs and the ZIP load at Bus 4. Fig. 4.22 shows the frequency when the 477 MW ZIP load is added to Bus 7. Fig. 4.23 is the power absorbed by the VSDs and the ZIP load at Bus 7.

Fig. 4.24 shows all of the generator frequencies, when there is a ZIP increase at Bus 6 and there is no frequency compensation from the VSDs. The frequency begins to drop quicker at generators closer to the load increase. Generator 6 decreases first, followed by Generators 5 and 7. Therefore, when the VSD is close to the load increase, the VSD is able to respond to the event quicker. This reduces the effect throughout the rest of the system. However, when the load increase happens in a location that has no VSDs in a close vicinity, there is minimal effect on the minimum frequency. The frequency does still return to the

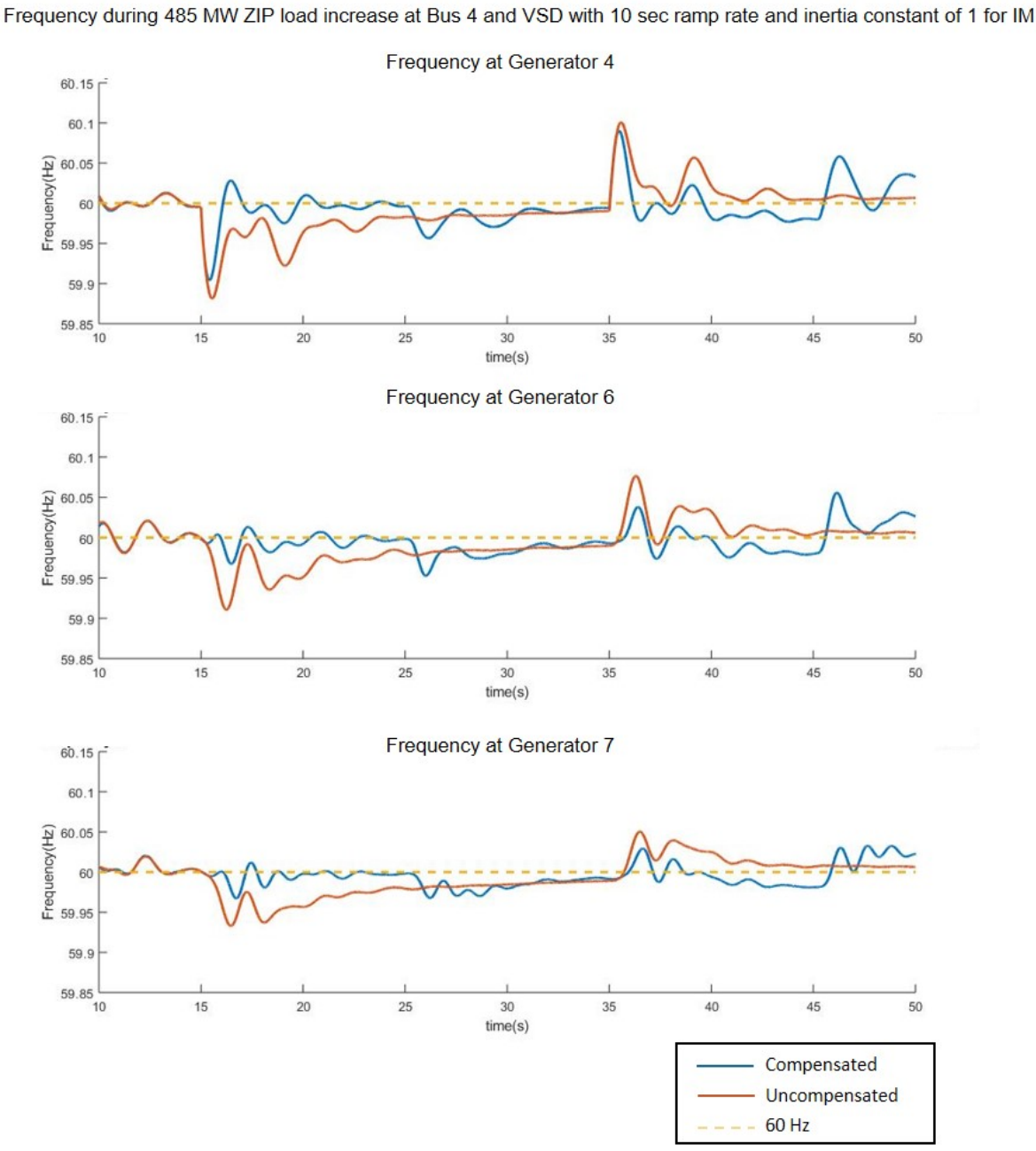


Figure 4.20: Frequency of generators 4, 6, and 7 during 485 MW ZIP load increase at Bus 4 comparing with frequency regulation and without frequency regulation.

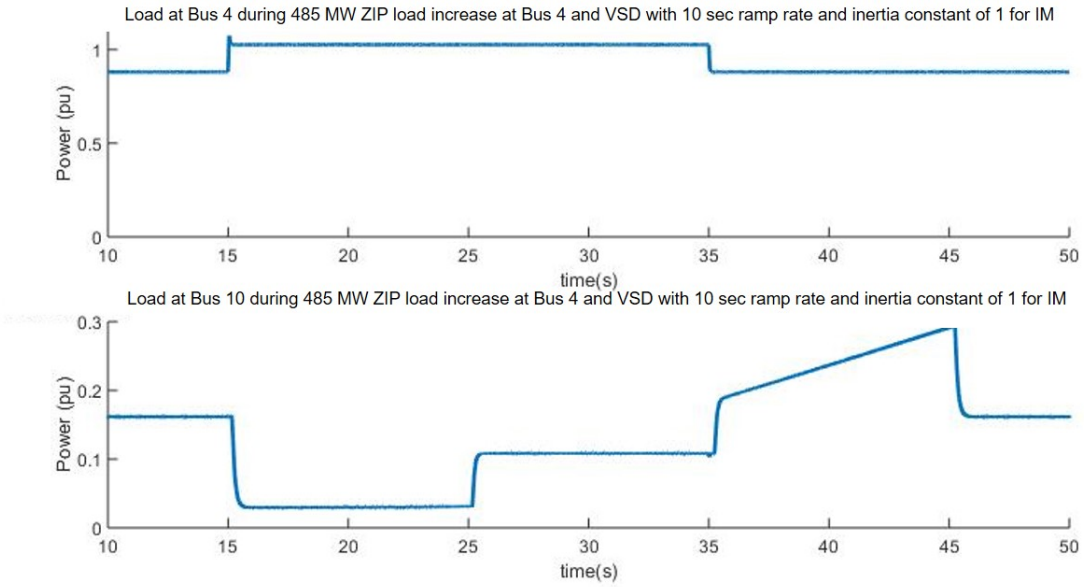


Figure 4.21: Load at Buses 4 and 10 during 485 MW ZIP load increase at Bus 4.

nominal value of 60 Hz quicker than without any frequency compensation from the VSDs, as seen in Fig. 4.18.

When there is a ZIP load increase near a bus with an VSD, the frequency response throughout the system is improved. Fig. 4.22 shows that the minimum frequency during the event is reduced at Bus 4 and Bus 6, and the frequency returns to the nominal value of 60 Hz quicker. Fig. 4.20 shows a similar response, where the ZIP load increase happens at Bus 4. The minimum frequency during the event is reduced for Buses 6 and 7. Table 4.3 shows the nadir frequencies after the load increase for all the generators on the system. There are two cases shown in the table– a load increase at Bus 4 and a load increase at Bus 7. You can see from this data that the improvement in the nadir frequency is the greatest the furthest from the event. The nadir frequency at the bus the event occured only improved by around 20 % for both cases. However, at the buses furthest from the event, the nadir frequency was improved by around 70 %.

For each of the cases, with the load increase at Buses 1, 4, and 7, there was only one VSD that was actively compensating the frequency. That compensation from the one VSD

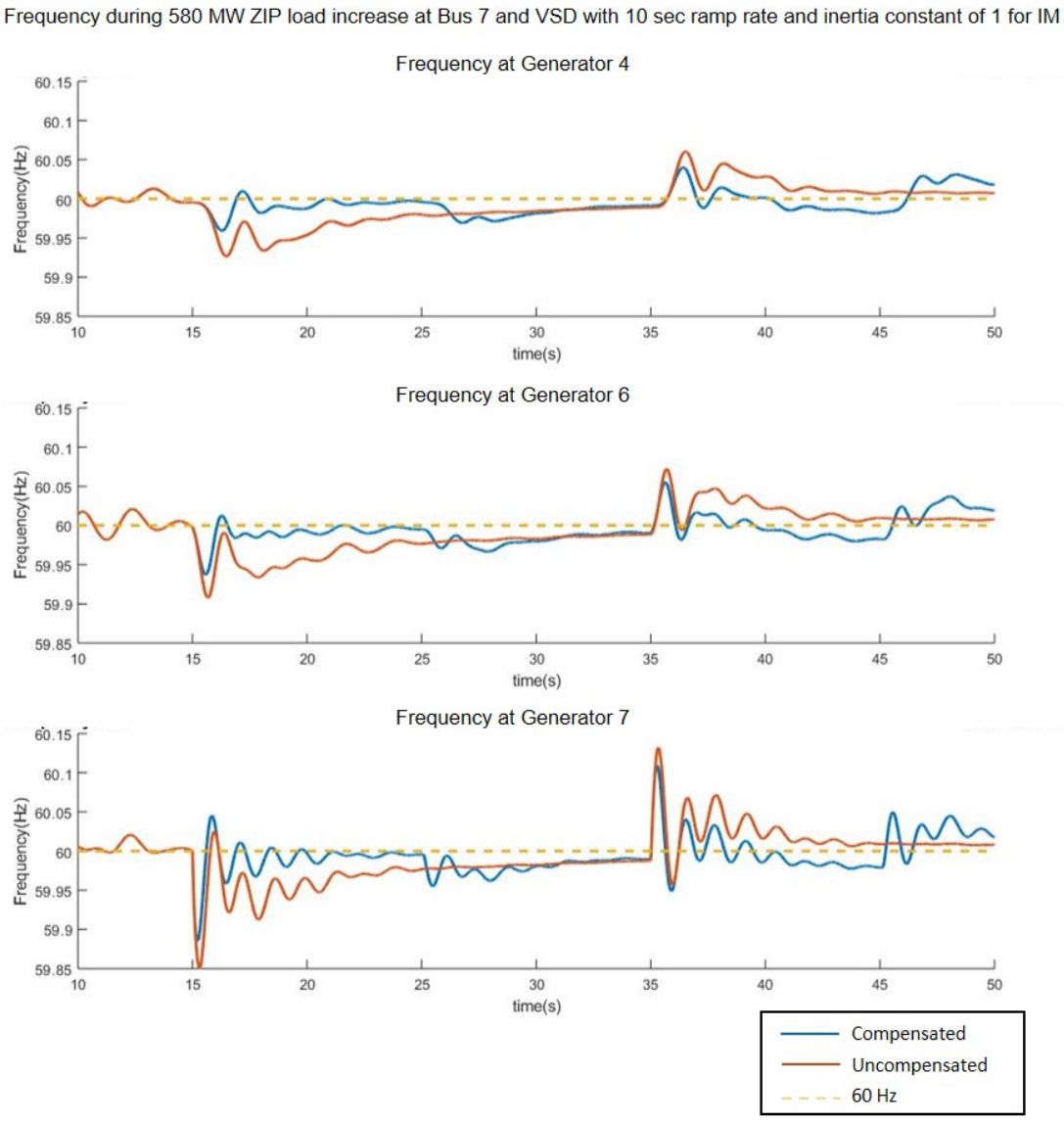


Figure 4.22: Frequency of generators 4, 6, and 7 during 530 MW ZIP load increase at Bus 7 comparing with frequency regulation and without frequency regulation.

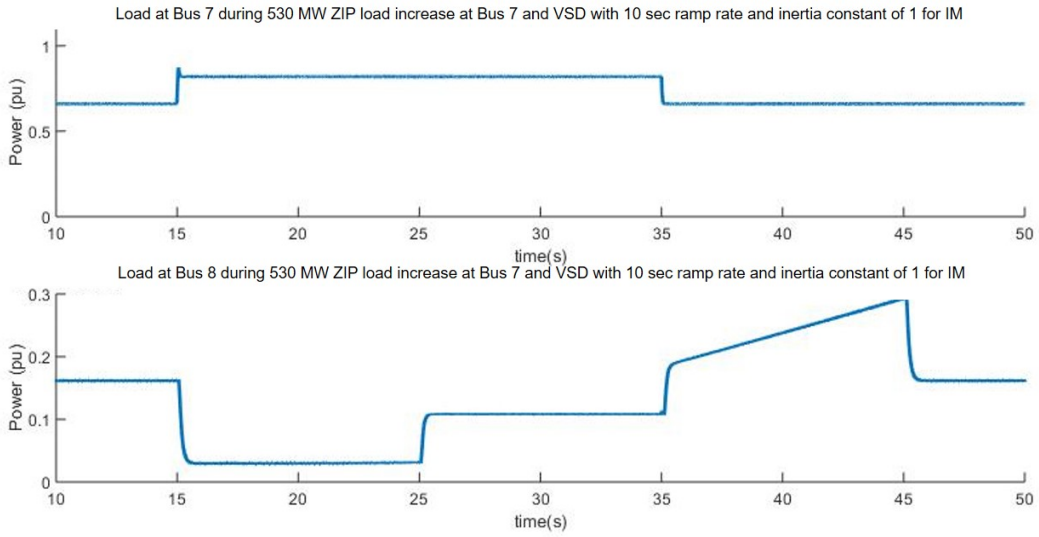


Figure 4.23: Load at Buses 7 and 8 during 530 MW ZIP load increase at Bus 7.

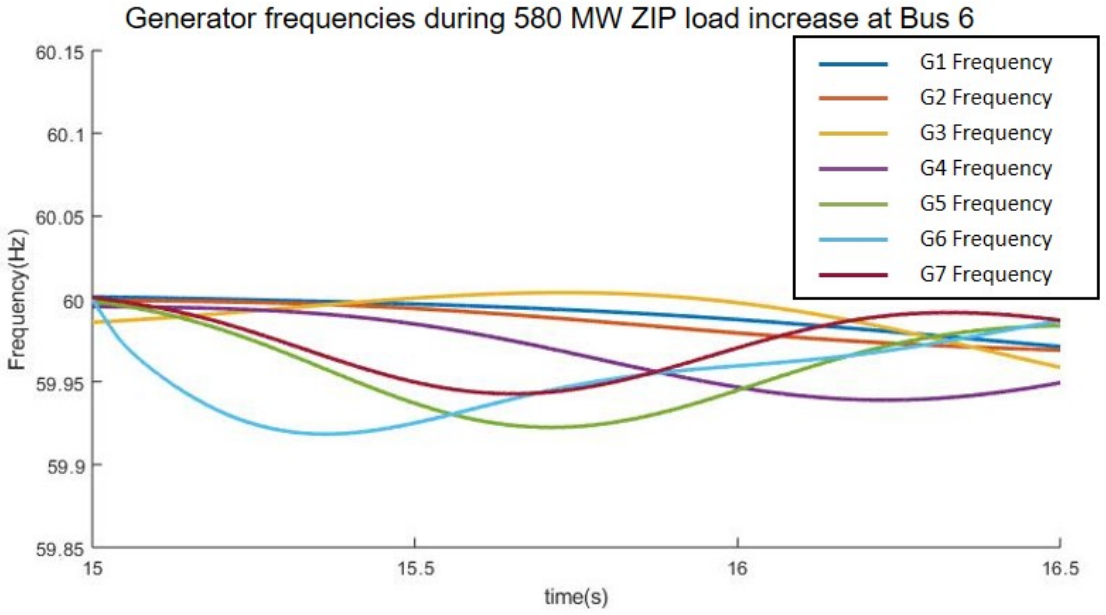


Figure 4.24: Frequency of all generators on WECC system during 530 MW ZIP load increase at Bus 6.

Table 4.3: Nadir frequency for generators during frequency event on WECC system with and without VSD frequency compensation.

Generator	Compensated	Uncompensated	Percent Improvement
Load increase at Bus 4			
Generator 1	59.98 Hz	59.92 Hz	71.00%
Generator 2	59.98 Hz	59.93 Hz	67.98%
Generator 3	59.97 Hz	59.93 Hz	47.14 %
Generator 4	59.90 Hz	59.88 Hz	19.11 %
Generator 5	59.97 Hz	59.91 Hz	65.23 %
Generator 6	59.97 Hz	59.91 Hz	63.53 %
Generator 7	59.97 Hz	59.93 Hz	50.89 %
Load increase at Bus 7			
Generator 1	59.98 Hz	59.93 Hz	72.05 %
Generator 2	59.98 Hz	59.94 Hz	73.92 %
Generator 3	59.97 Hz	59.91 Hz	61.91 %
Generator 4	59.96 Hz	59.93 Hz	44.61 %
Generator 5	59.94 Hz	59.92 Hz	33.50 %
Generator 6	59.94 Hz	59.91 Hz	31.73 %
Generator 7	59.89 Hz	59.85 Hz	23.32 %

prevented the other two VSDs' frequency from dropping below the deadband. A single VSD can provide some benefit to the wide area grid if a load increase or loss in generation happens in close proximity to the VSD. However, with a higher penetration of VSDs with frequency regulation, the greater the system benefit will be because more frequency events can be mitigated more quickly.

Using high inertia loads to participate in frequency regulation has its pros and cons. The high inertia can help with the initial frequency drop, counteracting the load imbalance. However, if the ramping of the motor speed stops before the load recovers, the inertia causes more variability in the system. This can be seen in Fig. 4.17. The VSD power has a step of about 0.05 p.u. at 25 seconds, when the induction motor stator voltage stops ramping and steadies out. However, the frequency response from this step is still less than the initial drop when the ZIP load is added. Therefore, even in the worst case, such as in Fig. 4.18, the VSD can help the initial drop, but adds additional variation 10 seconds later.

4.4 Chapter Summary

An active front end topology is used for the simulation and emulation of the system. Controls are implemented in the VSD, including DC link voltage, inner and outer current loop, and grid frequency regulation. Two different control techniques were used for the grid frequency regulation– one on the WECC system and one on a microgrid system. The different techniques were developed based on the frequency characteristics on both systems.

The model and system were verified by comparing results on the HTB platform and on the PSCAD/EMTDC simulation platform. The system level effects were simulated in PSCAD/EMTDC. Both the microgrid and the WECC system were simulated with and without the corresponding frequency regulation scheme.

Chapter 5

Summary and Conclusions

Induction motors make up a significant portion of the load on the power grid. The implementation of variable speed drives on induction motors brings, not only, efficiency savings for the customers, but also possible benefits to the utility companies, through demand response and ancillary services. VSDs are uniquely equipped to participate in the regulation market because of their ability to control the motor load. The motor speed can be changed variably, unlike most loads, which are either on or off. This project uses the HTB platform and PSCAD/EMTDC to develop, test, and utilize VSD connected industrial induction motors.

The development of new power devices with wide band gaps, such as SiC and GaN devices, have contributed to active front end VSDs have growth in popularity. For this reason, an active front end topology is used for the simulation and emulation of the system. Controls are implemented in the VSD, including DC link voltage, inner and outer current loop, and grid frequency regulation. Two different control techniques were used for the grid frequency regulation– one on the WECC system and one on a microgrid system. The different techniques were developed based on the frequency characteristics of both systems.

An active front end topology is used for the simulation and emulation of the system. Controls are implemented in the VSD, including DC link voltage, inner and outer current loop, and grid frequency regulation. Two different control techniques were used for the grid frequency regulation– one on the WECC system and one on a microgrid system. The different techniques were developed based on the frequency characteristics on both systems.

The model and system were verified by comparing results on the HTB platform and on the PSCAD/EMTDC simulation platform. The system level effects were simulated in PSCAD/EMTDC. Both the microgrid and the WECC system were simulated with and without the corresponding frequency regulation scheme.

The VSDs with frequency regulation bring major benefits to the microgrid system even with only one VSD. However, with more VSDs on the system, they can share the load, making the effect on each VSD minimal. To ride through a 0.1 p.u. load increase, each VSD only reduced the motor speed by 10 % for 30 seconds. This is not a long-term solution for grid unbalances, but it could help ride through temporary unbalances and prevent additional load shedding.

The WECC system had the greatest benefit with high penetration of VSDs on the grid. The ability to prevent the spread of the frequency event could have major benefits on the wide area grid. However, this requires large motors throughout the system to be equipped with VSDs and frequency regulation control.

Using high inertia loads to participate in frequency regulation has pros and cons. The high inertia can help with the initial frequency drop, counteracting the load imbalance; however, if the ramping of the motor speed stops before the load recovers, the inertia causes more variability in the system. While in the microgrid system, since a PI control is implemented, the VSD's frequency control can account for that initial decrease in power, the WECC system VSD's frequency control does not have that level of sensitivity.

The effects of this type of control on the motor and the VSDs are not discussed in this work. However, this could be a potential avenue for future work. For example, when there was only one VSD on the microgrid, the VSD load drops below zero, which means the load is actually supplying power to the grid momentarily. What effect does this have on the lifetime of the motor? Additionally, does a VSD that implements this control need to have different design parameters? Should the devices or passive components have higher ratings to account for this inrush current? How do these values compare with commonly used values in VSDs currently used?

Additionally, assumptions were made regarding the aggregation of VSDs with frequency regulation. Future work should also include the evaluation of this type of controls at lower

grid levels, for example: the distribution system. The accuracy of this type of aggregation should also be investigated.

Bibliography

Bibliography

[1] J. H. Eto, J. Undrill, C. Roberts, P. Mackin, and J. Ellis, "Frequency control requirements for reliable interconnection frequency response," 2018. 6

[2] J. Wang, Y. Ma, L. Yang, L. M. Tolbert, and F. Wang, "Power converter-based three-phase induction motor load emulator," in *2013 Twenty-Eighth Annual IEEE Applied Power Electronics Conference and Exposition (APEC)*, Conference Proceedings, pp. 3270–3274. [Online]. Available: https://ieeexplore.ieee.org/ielx7/6516132/6520164/06520769.pdf?tp=&arnumber=6520769&isnumber=6520164&ref= viii, 14, 20, 21

[3] S. Zhang, Y. Ma, L. Yang, F. Wang, and L. M. Tolbert, "Development of a hybrid emulation platform based on rtds and reconfigurable power converter-based testbed," in *2016 IEEE Applied Power Electronics Conference and Exposition (APEC)*, Conference Proceedings, pp. 3121–3127. [Online]. Available: https://ieeexplore.ieee.org/ielx7/7465913/7467833/07468310.pdf?tp=&arnumber=7468310&isnumber=7467833&ref= viii, 15, 16

[4] S. S. OFA, "United states industrial electric motor systems market opportunities assessment," 2002. 2, 3, 71

[5] S. Kouro, J. Rodriguez, B. Wu, S. Bernet, and M. Perez, "Powering the future of industry: High-power adjustable speed drive topologies," *IEEE Industry Applications Magazine*, vol. 18, no. 4, pp. 26–39, 2012. [Online]. Available: https://ieeexplore.ieee.org/ielx5/2943/6213196/06198407.pdf?tp=&arnumber=6198407&isnumber=6213196&ref= 2

[6] H. N. Hickok, "Adjustable speed—a tool for saving energy losses in pumps, fans, blowers, and compressors," *IEEE Transactions on Industry Applications*, vol. IA-21, no. 1, pp. 124–136, 1985. [Online]. Available: https://ieeexplore.ieee.org/ielx5/28/4157937/04157960.pdf?tp=&arnumber=4157960&isnumber=4157937&ref= 2

[7] R. Saidur, N. Rahim, H. Ping, M. Jahirul, S. Mekhilef, and H. H. Masjuki, ""energy and emission analysis for industrial motors in malaysia"," *Energy Policy*, vol. 37, no. 9, pp. 3650–3658, 2009. 2

[8] E. Mallada, C. Zhao, and S. Low, "Optimal load-side control for frequency regulation in smart grids," *IEEE Transactions on Automatic Control*, vol. 62, no. 12, pp. 6294–6309, 2017. [Online]. Available: https://ieeexplore.ieee.org/ielx7/9/8125784/07944568.pdf?tp=&arnumber=7944568&isnumber=8125784&ref= 3

[9] Y. Rebours, "A comprehensive assessment of markets for frequency and voltage control ancillary services," Thesis, 2008. [Online]. Available: https://tel.archives-ouvertes.fr/tel-00370805 3

[10] A. v. Jouanne, Z. Haoran, and A. K. Wallace, "An evaluation of mitigation techniques for bearing currents, emi and overvoltages in asd applications," *IEEE Transactions on Industry Applications*, vol. 34, no. 5, pp. 1113–1122, 1998. [Online]. Available: https://ieeexplore.ieee.org/ielx4/28/15542/00720452.pdf?tp=&arnumber=720452&isnumber=15542&ref= 3, 4

[11] H. Hao, B. M. Sanandaji, K. Poolla, and T. L. Vincent, "Frequency regulation from flexible loads: Potential, economics, and implementation," in *2014 American Control Conference*, Conference Proceedings, pp. 65–72. [Online]. Available: https://ieeexplore.ieee.org/ielx7/6849600/6858556/06858734.pdf?tp=&arnumber=6858734&isnumber=6858556&ref= 4

[12] R. Walawalkar, S. Fernands, N. Thakur, and K. R. Chevva, "Evolution and current status of demand response (dr) in electricity markets: Insights from pjm and nyiso," *Energy*, vol. 35, no. 4, pp. 1553–1560, 2010. 4

[13] Q. Qdr, "Benefits of demand response in electricity markets and recommendations for achieving them," *US Dept. Energy, Washington, DC, USA, Tech. Rep*, 2006. 5

[14] J. S. Vardakas, N. Zorba, and C. V. Verikoukis, "A survey on demand response programs in smart grids: Pricing methods and optimization algorithms," *IEEE Communications Surveys & Tutorials*, vol. 17, no. 1, pp. 152–178, 2015. [Online]. Available: https://ieeexplore.ieee.org/ielx7/9739/7061782/06861959.pdf?tp=&arnumber=6861959&isnumber=7061782&ref= 5, 6, 7, 8, 9

[15] M. Zimmerman, "The industry demands better demand response," in *2012 IEEE PES Innovative Smart Grid Technologies (ISGT)*, Conference Proceedings, pp. 1–3. [Online]. Available: https://ieeexplore.ieee.org/ielx5/6170475/6175527/06175672.pdf?tp=&arnumber=6175672&isnumber=6175527&ref= 6

[16] S. Mohagheghi and N. Raji, "Intelligent demand response scheme for energy management of industrial systems," in *2012 IEEE Industry Applications Society Annual Meeting*, Conference Proceedings, pp. 1–9. [Online]. Available: https://ieeexplore.ieee.org/ielx5/6361088/6373971/06374087.pdf?tp=&arnumber=6374087&isnumber=6373971&ref= 6

[17] M. H. Albadi and E. F. El-Saadany, "Demand response in electricity markets: An overview," in *2007 IEEE Power Engineering Society General Meeting*, Conference Proceedings, pp. 1–5. [Online]. Available: https://ieeexplore.ieee.org/ielx5/4275198/4275199/04275494.pdf?tp=&arnumber=4275494&isnumber=4275199&ref= 7

[18] V. C. Gungor, D. Sahin, T. Kocak, S. Ergut, C. Buccella, C. Cecati, and G. P. Hancke, "A survey on smart grid potential applications and communication requirements," *IEEE Transactions on Industrial Informatics*, vol. 9, no. 1, pp. 28–42, 2013. [Online]. Available: https://ieeexplore.ieee.org/ielx5/9424/6387656/06298960.pdf?tp=&arnumber=6298960&isnumber=6387656&ref= 7

[19] A. Faruqui, R. Hledik, and J. Tsoukalis, "The power of dynamic pricing," *The Electricity Journal*, vol. 22, no. 3, pp. 42–56, 2009. 9

[20] A. Faruqui, S. Sergici, and A. Sharif, "The impact of informational feedback on energy consumption—a survey of the experimental evidence," *Energy*, vol. 35, no. 4, pp. 1598–1608, 2010. 9

[21] J. Wang, M. A. Biviji, and W. M. Wang, "Lessons learned from smart grid enabled pricing programs," in *2011 IEEE Power and Energy Conference at Illinois*, Conference Proceedings, pp. 1–7. [Online]. Available: https://ieeexplore.ieee.org/ielx5/5729275/5740475/05740488.pdf?tp=&arnumber=5740488&isnumber=5740475&ref= 10

[22] F. A. Wolak, "Residential customer response to real-time pricing: The anaheim critical peak pricing experiment," 2007. 10

[23] S. Zhang, B. Liu, S. Zheng, Y. Ma, F. Wang, and L. M. Tolbert, "Three-phase short-circuit fault implementation in converter based transmission line emulator," in *2017 IEEE Energy Conversion Congress and Exposition (ECCE)*, Conference Proceedings, pp. 2914–2920. [Online]. Available: https://ieeexplore.ieee.org/ielx7/8085404/8095743/08096538.pdf?tp=&arnumber=8096538&isnumber=8095743&ref= 12

[24] ——, "Development of a converter-based transmission line emulator with three-phase short-circuit fault emulation capability," *IEEE Transactions on Power Electronics*, vol. 33, no. 12, pp. 10 215–10 228, 2018. [Online]. Available: https://ieeexplore.ieee.org/ielx7/63/8468129/08291602.pdf?tp=&arnumber=8291602&isnumber=8468129&ref= 12

[25] D. Li, Y. Ma, C. Zhang, H. Yin, I. Ray, Y. Su, L. Zhu, F. Wang, and L. M. Tolbert, "Development of a converter based microgrid test platform," in *2019 IEEE Energy Conversion Congress and Exposition (ECCE)*, Conference Proceedings, pp. 6294–6300. 15

[26] S. Zhen, Y. Ma, F. Wang, and L. M. Tolbert, "Operation of a flexible dynamic boundary microgrid with multiple islands," in *2019 IEEE Applied Power Electronics Conference and Exposition (APEC)*, Conference Proceedings, pp. 548–554. [Online]. Available: https://ieeexplore.ieee.org/ielx7/8716496/8721765/08721836.pdf?tp=&arnumber=8721836&isnumber=8721765&ref= 15

[27] Y. Ma, X. Hu, H. Yin, L. Zhu, Y. Su, F. Wang, L. M. Tolbert, and Y. Liu, "Real-time control and operation for a flexible microgrid with dynamic boundary," in *2018 IEEE Energy Conversion Congress and Exposition (ECCE)*, Conference Proceedings, pp. 5158–5163. [Online]. Available: https://ieeexplore.ieee.org/ielx7/8537478/8557346/08558364.pdf?tp=&arnumber=8558364&isnumber=8557346&ref= 15

[28] J. Wang, L. Yang, Y. Ma, J. Wang, L. M. Tolbert, F. Wang, and K. Tomsovic, "Static and dynamic power system load emulation in converter-based reconfigurable power grid emulator," in *2014 IEEE Energy Conversion Congress and Exposition (ECCE)*, Conference Proceedings, pp. 4008–4015. 15

[29] L. Yang, J. Wang, Y. Ma, J. Wang, X. Zhang, L. M. Tolbert, F. F. Wang, and K. Tomsovic, "Three-phase power converter-based real-time synchronous generator emulation," *IEEE Transactions on Power Electronics*, vol. 32, no. 2, pp. 1651–1665, 2017. [Online]. Available: https://ieeexplore.ieee.org/ielx7/63/7742436/07451263.pdf?tp=&arnumber=7451263&isnumber=7742436&ref= 15

[30] J. D. Boles, Y. Ma, J. Wang, D. Osipov, L. M. Tolbert, and F. Wang, "Converter-based emulation of battery energy storage systems (bess) for grid applications," *IEEE Transactions on Industry Applications*, vol. 55, no. 4, pp. 4020–4032, 2019. [Online]. Available: https://ieeexplore.ieee.org/ielx7/28/8752494/08703886.pdf?tp=&arnumber=8703886&isnumber=8752494&ref= 15

[31] W. Cao, Y. Ma, J. Wang, L. Yang, J. Wang, F. Wang, and L. M. Tolbert, "Two-stage pv inverter system emulator in converter based power grid emulation system," in *2013 IEEE Energy Conversion Congress and Exposition*, Conference Proceedings, pp. 4518–4525. [Online]. Available: https://ieeexplore.ieee.org/ielx7/6624149/6646663/06647305.pdf?tp=&arnumber=6647305&isnumber=6646663&ref= 15

[32] L. Yang, X. Zhang, Y. Ma, J. Wang, L. Hang, K. Lin, L. M. Tolbert, F. Wang, and K. Tomsovic, "Hardware implementation and control design of generator emulator in multi-converter system," in *2013 Twenty-Eighth Annual IEEE Applied Power Electronics Conference and Exposition (APEC)*, Conference Proceedings, pp.

2316–2323. [Online]. Available: https://ieeexplore.ieee.org/ielx7/6516132/6520164/06520618.pdf?tp=&arnumber=6520618&isnumber=6520164&ref= 15

[33] S. Zhang, B. Liu, S. Zheng, Y. Ma, F. Wang, and L. M. Tolbert, "Development of a converter-based transmission line emulator with three-phase short-circuit fault emulation capability," *IEEE Transactions on Power Electronics*, vol. 33, no. 12, pp. 10 215–10 228, 2018. [Online]. Available: https://ieeexplore.ieee.org/ielx7/63/8468129/08291602.pdf?tp=&arnumber=8291602&isnumber=8468129&ref= 15

[34] ——, "Three-phase short-circuit fault implementation in converter based transmission line emulator," in *2017 IEEE Energy Conversion Congress and Exposition (ECCE)*, Conference Proceedings, pp. 2914–2920. [Online]. Available: https://ieeexplore.ieee.org/ielx7/8085404/8095743/08096538.pdf?tp=&arnumber=8096538&isnumber=8095743&ref= 15

[35] Y. Li, X. Shi, B. Liu, W. Lei, F. Wang, and L. M. Tolbert, "Development, demonstration, and control of a testbed for multiterminal hvdc system," *IEEE Transactions on Power Electronics*, vol. 32, no. 8, pp. 6069–6078, 2017. [Online]. Available: https://ieeexplore.ieee.org/ielx7/63/7886374/07605457.pdf?tp=&arnumber=7605457&isnumber=7886374&ref= 15

[36] Y. Li, X. Shi, B. Liu, F. Wang, L. M. Tolbert, and W. Lei, "Hardware implementation of a four-terminal hvdc test-bed," in *2015 IEEE Energy Conversion Congress and Exposition (ECCE)*, Conference Proceedings, pp. 5363–5370. [Online]. Available: https://ieeexplore.ieee.org/ielx7/7298093/7309651/07310414.pdf?tp=&arnumber=7310414&isnumber=7309651&ref= 15

[37] L. Moran, J. Espinoza, M. Ortiz, J. Rodriguez, and J. Dixon, "Practical problems associated with the operation of asds based on active front end converters in power distribution systems," in *Conference Record of the 2004 IEEE Industry Applications Conference, 2004. 39th IAS Annual Meeting.*, vol. 4, Conference Proceedings, pp. 2568–2572 vol.4. [Online]. Available: https://ieeexplore.ieee.org/ielx5/9338/29652/01348837.pdf?tp=&arnumber=1348837&isnumber=29652&ref= 23, 24

[38] M. Fioretto, G. Raimondo, L. Rubino, N. Serbia, and P. Marino, "Power losses analysis in ac/dc conversion based on active front end systems," in *SPEEDAM 2010*, Conference Proceedings, pp. 210–215. [Online]. Available: https://ieeexplore.ieee.org/ielx5/5530000/5542021/05542199.pdf?tp=&arnumber=5542199&isnumber=5542021&ref= 23

[39] L. Wei, Y. Patel, and C. S. N. Murthy, "Evaluation of lcl filter inductor and active front end rectifier losses under different pwm method," in *2013 IEEE Energy Conversion Congress and Exposition*, Conference Proceedings, pp. 3019–3026. [Online]. Available: https://ieeexplore.ieee.org/ielx7/6624149/6646663/06647095.pdf?tp=&arnumber=6647095&isnumber=6646663&ref= 23

[40] A. Q. Huang, "Wide bandgap (wbg) power devices and their impacts on power delivery systems," in *2016 IEEE International Electron Devices Meeting (IEDM)*, Conference Proceedings, pp. 20.1.1–20.1.4. [Online]. Available: https://ieeexplore.ieee.org/ielx7/7824662/7838021/07838457.pdf?tp=&arnumber=7838457&isnumber=7838021&ref= 25

[41] K. Madjour, "Silicon carbide market update: from discrete devices to modules," in *PCIM Europe*, Conference Proceedings. 26

[42] L. M. Tolbert, B. Ozpineci, S. K. Islam, and M. S. Chinthavali, "Wide bandgap semiconductors for utility applications," *semiconductors*, vol. 1, p. 3, 2003. 25, 27

[43] K. Shenai, M. Dudley, and R. F. Davis, "Current status and emerging trends in wide bandgap (wbg) semiconductor power switching devices," *ECS Journal of Solid State Science and Technology*, vol. 2, no. 8, pp. N3055–N3063, 2013. 25, 26

[44] S. Mao, T. Wu, X. Lu, J. Popovic, and J. A. Ferreira, "Three-phase active front-end rectifier efficiency improvement with silicon carbide power semiconductor devices," in *2016 IEEE Energy Conversion Congress and Exposition (ECCE)*, Conference Proceedings, pp. 1–8. [Online]. Available: https://ieeexplore.ieee.org/ielx7/7835398/7854636/07855515.pdf?tp=&arnumber=7855515&isnumber=7854636&ref= 25

[45] S. Hiti, "Modeling and control of three-phase pwm converters," Thesis, 1995. 30, 31, 32, 50

[46] J. Dannehl, C. Wessels, and F. W. Fuchs, "Limitations of voltage-oriented pi current control of grid-connected pwm rectifiers with*lcl*filters," *IEEE Transactions on Industrial Electronics*, vol. 56, no. 2, pp. 380–388, 2009. [Online]. Available: https://ieeexplore.ieee.org/ielx5/41/4771829/04667634.pdf?tp=&arnumber=4667634&isnumber=4771829&ref= 32, 33

[47] P. Verdelho and G. D. Marques, "Dc voltage control and stability analysis of pwm-voltage-type reversible rectifiers," *IEEE Transactions on Industrial Electronics*, vol. 45, no. 2, pp. 263–273, 1998. [Online]. Available: https://ieeexplore.ieee.org/ielx4/41/14965/00681225.pdf?tp=&arnumber=681225&isnumber=14965&ref= 32, 33, 48

[48] B. Akin and N. Garg, "Scalar (v/f) control of 3-phase induction motors," *Texas Instruments Incorporated, Texas*, 2013. 34, 35, 36, 49

[49] R. Azizipanah-Abarghooee and M. Malekpour, "Smart induction motor variable frequency drives for primary frequency regulation," *IEEE Transactions on Energy Conversion*, pp. 1–1, 2019. 37, 38

[50] M. Malekpour, R. Azizipanah-Abarghooee, F. Teng, G. Strbac, and V. Terzija, "Fast frequency response from smart induction motor variable speed drives," *IEEE Transactions on Power Systems*, pp. 1–1, 2019. [Online]. Available: https://ieeexplore.ieee.org/ielx7/59/4374138/08809714.pdf?tp=&arnumber=8809714&isnumber=4374138&ref= 37, 39

[51] S. Wang, S. Zhang, Y. Ma, F. Wang, and L. M. Tolbert, "Analysis of mtdc inertia emulation impact on connected ac systems," in *2018 IEEE Energy Conversion Congress and Exposition (ECCE)*, Conference Proceedings, pp. 3705–3712. [Online]. Available: https://ieeexplore.ieee.org/ielx7/8537478/8557346/08557977.pdf?tp=&arnumber=8557977&isnumber=8557346&ref= 39, 40

[52] W. Cao, Y. Ma, J. Wang, L. Yang, J. Wang, F. Wang, and L. M. Tolbert, "Two-stage pv inverter system emulator in converter based power grid emulation system," in *2013 IEEE Energy Conversion Congress and Exposition*, Conference Proceedings, pp. 4518–4525. [Online]. Available: https://ieeexplore.ieee.org/ielx7/6624149/6646663/06647305.pdf?tp=&arnumber=6647305&isnumber=6646663&ref= 48

Vita

Taylor L. Short was raised in Munford, TN, where she graduate from Munford High School in 2013. She began pursuing a degree in electrical engineering at the University of Tennessee, Knoxville the following fall and graduated cum laude with a B.S. from the Tickle College of Engineering in 2018. As a Master's student, Taylor is now a Wide Bandgap Trainee and works through the Center for Ultra Wide-Area Resilient Electric Energy Transmission Networks (CURENT) as a Graduate Research Assistant. She has been involved with CURENT since 2014 through various research, outreach, and leadership opportunities. Also, as an undergraduate, Taylor completed four co-op rotations in Southern Company's Research and Development group, where she worked on technology innovation for transmission and distribution monitoring and maintenance. In addition to her school and work, Taylor has participated in various outreach and leadership initiatives, including planning the second biennial WomEngineers Day.